N73-18648

NASA CONTRACTOR REPORT

NASA CR-2201

NASA CR-2201

A FIELD INVESTIGATION AND NUMERICAL SIMULATION OF COASTAL FOG

by E. J. Mack, W. J. Eadie, C. W. Rogers,
W. C. Kocmond, and R. J. Pilie

Prepared by
CORNELL AERONAUTICAL LABORATORY, INC.
Buffalo, N.Y. 14221
for George C. Marshall Space Flight Center

NATIONAL AERONAUTICS AND SPACE ADMINISTRATION • WASHINGTON, D. C. • FEBRUARY 1973

1. Report No. NASA CR-2201	2. Government Accession No.	3. Recipient's Catalog No.

4. Title and Subtitle
A FIELD INVESTIGATION AND NUMERICAL SIMULATION OF COASTAL FOG

5. Report Date
February 1973

6. Performing Organization Code
M111

7. Author(s)
E. J. Mack, W. J. Eadie, C. W. Rogers, W. C. Kocmond, and R. J. Pilie

8. Performing Organization Report No.
CJ-5055-M-1

9. Performing Organization Name and Address
Cornell Aeronautical Laboratory, Inc.
Buffalo, New York 14221

10. Work Unit No.

11. Contract or Grant No.
NAS 8-27999

12. Sponsoring Agency Name and Address
National Aeronautics and Space Administration
Washington, D. C. 20546

13. Type of Report and Period Covered
CONTRACTOR

14. Sponsoring Agency Code

15. Supplementary Notes

16. Abstract

A field investigation of the microphysical and micrometeorological features of fogs occurring near Los Angeles and Vandenberg, California was conducted. Observations of wind speed and direction, temperature, dew point, vertical wind velocity, dew deposition, drop-size distribution, liquid water content, and haze and cloud nucleus concentration were obtained. These observations were initiated in late evening prior to fog formation and continued until the time of dissipation in both advection and radiation fogs. Data were also acquired in one valley fog and several dense haze situations. The behavior of these parameters prior to and during fog are discussed in detail.

A two-dimensional numerical model was developed to investigate the formation and dissipation of advection fogs under the influence of horizontal variations in surface temperature. The model predicts the evolution of potential temperature, water vapor content, and liquid water content in a vertical plane as determined by vertical turbulent transfer and horizontal advection. Results are discussed from preliminary numerical experiments on the formation of warm-air advection fog and dissipation by natural and artificial heating from the surface.

17. Key Words (Suggested by Author(s))
Numerical Simulation
Field Investigation
Fog Microphysics
Micrometeorological

18. Distribution Statement

19. Security Classif. (of this report) Unclassified	20. Security Classif. (of this page) Unclassified	21. No. of Pages 145	22. Price $3.00

MSFC - Form 3292-1 (April 1972)

For sale by National Technical Information Service, Springfield, Virginia 22151

TABLE OF CONTENTS

Section | Page

LIST OF FIGURES

LIST OF TABLES

ACKNOWLEDGEMENTS

The authors express their gratitude to members of the Atmospheric Sciences Section of the Environmental Systems Department of CAL who participated in this program and who contributed long hours of their time during the field trips to Vandenberg Air Force Base and Los Angeles International Airport.

Special thanks are due Major J. Russell of the United States Air Force, Vandenberg Air Force Base for coordinating our numerous project requirements with base personnel. We are indebted to the many members of the Los Angeles Airport and Federal Aviation Agency who helped arrange for this study on the airport grounds and who assisted in the selection of instrumentation sites. In particular, we wish to thank Mr. Robert C. Davidson, Deputy General Manager, for his contributions in this respect and Mr. Paul Rittenberg of the FAA for his special help in arranging the installation of our equipment at the ASDE and VOR sites.

Finally, we wish to thank Miss Christine R. Schurkus for her swift and accurate typing of this manuscript and for her help in handling administrative matters during our absence.

INTRODUCTION

The Cornell Aeronautical Laboratory, Inc. (CAL) under the joint sponsorship and technical cognizance of Mr. O. H. Vaughan, Aerospace Environment Division, Marshall Space Flight Center, Huntsville, Alabama, NASA, and Mr. Murray H. Schefer, Naval Air Systems Command,. Department of the Navy, Washington, D. C., has been performing an investigation of warm fog properties and fog modification concepts. Earlier investigations performed by CAL under NASA sponsorship were aimed at developing a practical method for improving visibility in natural fog. As a result of these studies, which included the development of physical and dynamic models for describing important fog properties, a concept evolved for modifying natural fogs with sized hygroscopic materials.

Field experiments designed to test the seeding concept were successfully performed during the summers of 1968 and 1969 (Kocmond and Eadie, 1969; Kocmond et al., 1971) in Elmira, NY. It was clear from these tests, however, that natural fog formation and dissipation were complicated processes and that far more detailed measurements were needed to adequately describe the natural fog life cycle. With this goal in mind, emphasis during the following year was placed on acquiring measurements in the field that would help describe the microphysical and dynamic properties of fog. Pursuit of this goal resulted in one of the most complete and extensive investigations of valley fog behavior to date (Pilié et al., 1972). Information was gathered relative to visibility in fog, micrometeorological data including low level temperature and dew point structure, dew deposition and evaporation rates, wind speed and direction, and radiation. Microphysics data were acquired through the fog life cycle and cloud nucleus concentrations were measured at several altitudes from an aircraft prior to fog formation. These data were used to interpret important fog formation processes including the role of dew in the formation of fog and the evolution of drop-size distributions.

One of the important facets of fog that was not adequately answered, however, involved an understanding of the influence of cloud nucleus type and concentration on the microphysical features of fog. Although natural as well as man-made particulates are known to serve as condensation sites for the formation of fog, very little information has been made available on how common fog types differ in relatively polluted and clean environments, respectively.

In an attempt to gain a better understanding of the role of pollutants on fog microstructure and to obtain observations in coastal fog, preliminary life cycle studies were performed at Vandenberg and Los Angeles, California during the late summer and fall of 1971. Field investigations were conducted during the periods 10 September through 2 October at Vandenberg Air Force Base and 25 October through 20 November at the Los Angeles International Airport. Measurements were obtained in seven fogs and one dense haze (visibility 4-6 km) during the three-week period at Vandenberg. Of the fogs which were observed at Vandenberg, three were advection fogs, two were radiation fogs, one was a frontal fog, and one was a radiation-valley fog. At Los Angeles, observations were made in the two radiation fogs and the two dense haze (visibility 5-10 km) situations which occurred during the four-week field trip.

Advection fog was the most common fog type occurring in the vicinity of the Vandenberg coastal site. At the Los Angeles coastal site, however, only radiation fog was observed. The physical and dynamic characteristics of the coastal advection fog differed markedly from that of both the coastal radiation fog of Los Angeles and a coastal radiation fog which formed at Vandenberg. Further, the physical characteristics of radiation fog forming at the two sites also varied substantially. These data are summarized in Chapter II and discussed in detail in Chapter III.

Observations were also obtained in a valley fog which occurred near the Vandenberg coastal site. Data acquired in that fog are compared in Chapter III with similar data obtained in Elmira.

Data were also acquired in dense haze at both Los Angeles and Vandenberg during periods in which visibility degraded to between 4 and 10 km. Visibility restriction was due to the presence of drops of up to 20 μm radius. These data are discussed in Chapter III.

Daily measurements of cloud and haze nucleus concentration as well as occasional areal surveys provided useful support data that was instrumental in the interpretation of visibility and liquid water content data. Observations of haze and cloud nucleus concentration as a function of distance inland (downwind) from the Pacific Ocean are discussed within the text and compared with similar data obtained on the Pacific coast of Washington. These data are presented in Chapter III.

A two-dimensional numerical model was developed to investigate the formation of advection fogs and their dissipation by natural and artificial heating. The model incorporates several features of an earlier one-dimensional radiation fog model (Pilié et al., 1972) developed at CAL. The physical and mathematical foundations of the advection fog model and results of preliminary numerical experiments with the model are presented in Chapter IV. The basic capabilities and characteristics of the model are demonstrated in the formation and dissipation of warm-air advection fog. Recommendations are presented for future numerical modeling research which builds upon the initial model development in the present study. Documentation of the computer program for the model is provided in Appendix A.

II. SUMMARY OF OBSERVATIONS

The primary objectives of the field investigations were (1) to perform a study of the life cycle of coastal advection fogs forming in the vicinity of Vandenberg Air Force Base and Los Angeles, California; and (2) to compare characteristics of fog formed in a clean environment (Vandenberg) with that of fogs formed in a relatively polluted region (Los Angeles). Instrumentation was installed at several locations on the grounds of Vandenberg Air Force Base and the Los Angeles International Airport. Existing towers of approximately 35 m height were instrumented, and primary data acquisition sites were located within several kilometers of the Pacific shoreline.

Measurements were obtained in a total of three coastal advection fogs and one radiation fog at Vandenberg during the period 10 September through 2 October 1971. At Los Angeles, data were acquired in the only two fogs (radiation type) which occurred during the 25 October to 20 November 1971 field trip. In addition, data were obtained in one brief frontal fog, a valley fog, and a dense haze (visibility, 4-6 km) which occurred at Vandenberg and in two dense haze (visibility 5-10 km) situations occurring at Los Angeles.

Continuous measurements of temperature at five levels between the surface and ~35 m, dew point at four levels, and wind speed and direction at two levels were obtained during each occurrence of fog. Vertical wind velocity was measured at ~35 m and visibility was measured between 1.0 and 32 m. At the surface, visibility was continuously measured at three sites and dew deposition was monitored only at the primary data acquisition site. Nucleus concentrations were measured several times nightly; once fog had formed, measurements of drop-size distribution and liquid water content (LWC) were obtained at intervals varying from several minutes to several hours.

Haze nucleus[*] concentration at 97, 99, and 100% RH, cloud nucleus concentration at 0.3 and 1.0%S and Aitken (total particulate) nucleus concentration were measured on a daily basis. The nucleus populations at the two west coast sites differed markedly. The data have been averaged and are compared in Table I with similar data acquired near Elmira, NY.

Table I

Comparison of Average Nucleus Concentrations (cm^{-3})
Measured at Three Locations

	Haze Nuclei			Cloud Nuclei		Aitken Nuclei
	97%	99%	100% RH	0.3%S	1.0%S	
Elmira	--	--	--	900	3300	2.1×10^4
Vandenberg	25	35	40	250	630	0.3×10^4
Los Angeles	310	370	580	1800	2800	2.9×10^4

In Los Angeles, data were obtained about 0.7 km from the ocean at a site upwind (west) of the Los Angeles International Airport. The Vandenberg data were obtained approximately 1.4 km inland from the ocean shoreline. The Elmira data were acquired at the Chemung County Airport located at the center of the valley floor. The high nucleus concentrations observed at Elmira can be attributed to pollutants (industrial, vehicle traffic, air traffic, etc.) trapped by a nocturnal inversion which often occurred within the valley on clear nights.

As expected, the lowest nucleus concentrations were measured at Vandenberg. These values are typical of those found in unpolluted coastal regions. At Los Angeles, however, in addition to predictably high concentrations of Aitken nuclei, there are large concentrations of particulates which serve as extremely effective condensation sites (i.e., haze nuclei which form solution droplets at relative humidities of 95% and lower). These nuclei are probably of mixed origin, occurring as a result of man-made and natural

---

[*] Hygroscopic nuclei which deliquesce and grow to ~1 μm radius at relative humidities near 100%.

processes, including the formation of abundant photochemical aerosols in the Los Angeles Basin.

Fogs formed in environments of differing nucleus populations such as those observed at Elmira, Vandenberg and Los Angeles were found to exhibit different microphysical characteristics. The observed differences in characteristics of these fogs, however, were not completely attributable to the observed differences in nucleus populations. The effects of nucleus activation spectra on microphysical characteristics of the fog were in many cases masked by differing fog formation mechanisms which prevailed during the periods of observation at each site. Nevertheless, some significant effects were discerned.

The Los Angeles fog was a true radiation fog formed under clear skies. The Elmira valley fog was also a radiation fog but actual fog formation was stimulated by nocturnal valley circulations on cloudless nights. The coastal advection fog of Vandenberg, on the other hand, was an aged, low lying stratus cloud of considerable depth.

Fog microphysics data were obtained in fogs typical of those which form at each of the sites. Average data, acquired during the uniformly dense (visibility ≤ 0.5 km) and mature stage of these fogs are compared in Table II. As shown by the data, the largest drops, lowest LWC, and greatest minimum visibilities were observed in Vandenberg advection fogs.

Table II

Comparison of Average Microphysical Characteristics of Dense Fogs Occurring at Three Locations

Site	Mode Rad. (μm)	Typical Measured Drop Size Range (rad-μm)	Avg. LWC (mg m^{-3})	Max. LWC (mg m^{-3})	Avg. Min. Vsby. (m)
Elmira (Valley Fog)	1.5-3.0 6.0-10	1.5-30	100	210	200-600
Vandenberg (Advection Fog)	6.0-10	1.5-100	80	120	400-1000
Los Angeles (Radiation Fog)	(< 1.0) 6.0-10	$\leq$ 1.0-30	170	310	40-200

Most drop-size distributions measured in Vandenberg advection fog were found to have significant concentrations of drops of up to 100 μm radius. These large drops were observed in the form of a continuous light drizzle which persisted throughout the life cycle of the fog.

The advection fogs at Vandenberg form offshore and, under appropriate synoptic conditions, the normal sea breeze advects the fog inland before natural dissipation occurs. In our study, the appearance of fog at the surface was usually preceded (by several hours) by cloud cover. The cloud layer was frequently dense enough to reduce radiational cooling and prevent dew formation. As a result, surface temperature and dew point temperature remained warmer than temperatures aloft. Vertical temperature profiles ranged from isothermal to superadiabatic but, typically, were approximately adiabatic. No changes in the vertical temperature distribution or absolute temperature were observed at the times of fog occurrence.

The presence of advection fog at the instrumented sites was closely correlated with low level (10-30 m) wind direction. During these episodes of advection fog, a shift to easterly (offshore) winds was followed by improvements in visibility. Onshore winds prevailed during periods of low visibility.

At Los Angeles, radiation fogs (as shown in Table II) were characterized by extremely low visibilities, high liquid water contents, and small droplets. Drop-size distributions measured in the Los Angeles radiation fogs were relatively narrow and sharply peaked. The distributions were further distinguished by the presence of high concentrations of micron size droplets. These droplets were formed on the abundant hygroscopic haze nuclei that were present in the Los Angeles area.

During the two occurrences of radiation fog, haze nucleus concentrations were found to be a factor of two greater than the average. Haze nucleus concentrations at 100% RH prior to fog were 1200-1300 cm^{-3}. Calculations indicate that such concentrations of micron size droplets could reduce visibility to several hundred meters. It is likely, therefore, that a significant fraction of the visibility restriction observed in the Los Angeles fogs was attributable to the presence of high concentrations of these hygroscopic particulates.

The Los Angeles fogs formed under clear skies and hence radiational cooling produced substantial dew deposition. Prior to fog formation, low level inversions of up to 3.5°C/100 m were observed in the lowest 30 m. In both cases, fog was advected over the observation site by light easterly winds. After fog covered the region, the vertical temperature structure became superadiabatic. This superadiabatic lapse rate remained relatively constant until after sunrise when fog dissipation occurred. Similar changes in vertical temperature distribution accompanied the formation of radiation fog at Vandenberg, and these two sets of observations are in agreement with observations reported previously for valley fog in Elmira, NY.

III. FIELD INVESTIGATIONS

A. FIELD SITES AND INSTRUMENTATION

In order to compare the physical characteristics of fogs formed in a relatively clean environment with those of fogs formed in a polluted region, two field sites were chosen for this study. Vandenberg, California, which has a high incidence of advection fog was selected for its clean maritime environment. Los Angeles, California (peak fog season, October-December) was the choice for measurements in fog formed in a polluted environment:

1. The Vandenberg Field Site

The field installation at Vandenberg, illustrated in Figure 1, was designed primarily for measurements at 30 m, 60 m, and 105 m (MSL) elevations on the gentle coastal slopes that characterize the coastal region approximately eight kilometers north of Point Arguello. The primary experimental site, recorded as the Tower site, was established at PLC-A where a 32 m high tower was made available to us by the Air Force. This installation, located approximately one kilometer inland at 60 m MSL, included the instrumentation listed in Table III.

Table III

Instrumentation

On Surface	On Tower
G. E. small particle counter (Aitken nuclei)	Temperature sensors (1, 3, 10, 32 m levels)
Thermal diffusion chamber (cloud nuclei)	Dewpoint sensors (1, 3, 10, 32 m levels)
Haze chamber (haze nuclei)	Anemometers and wind vanes (10 and 32 m levels)
Gelman high volume sampler (LWC)	Vertical anemometer (32 m level)
Dew plate	Drop sampler (25 m level)
Temperature sensor (on ground)	Slant range transmissometer (1 to 30 m)
Transmissometer (1.2 m level)	
Drop sampler (1.2 m level)	

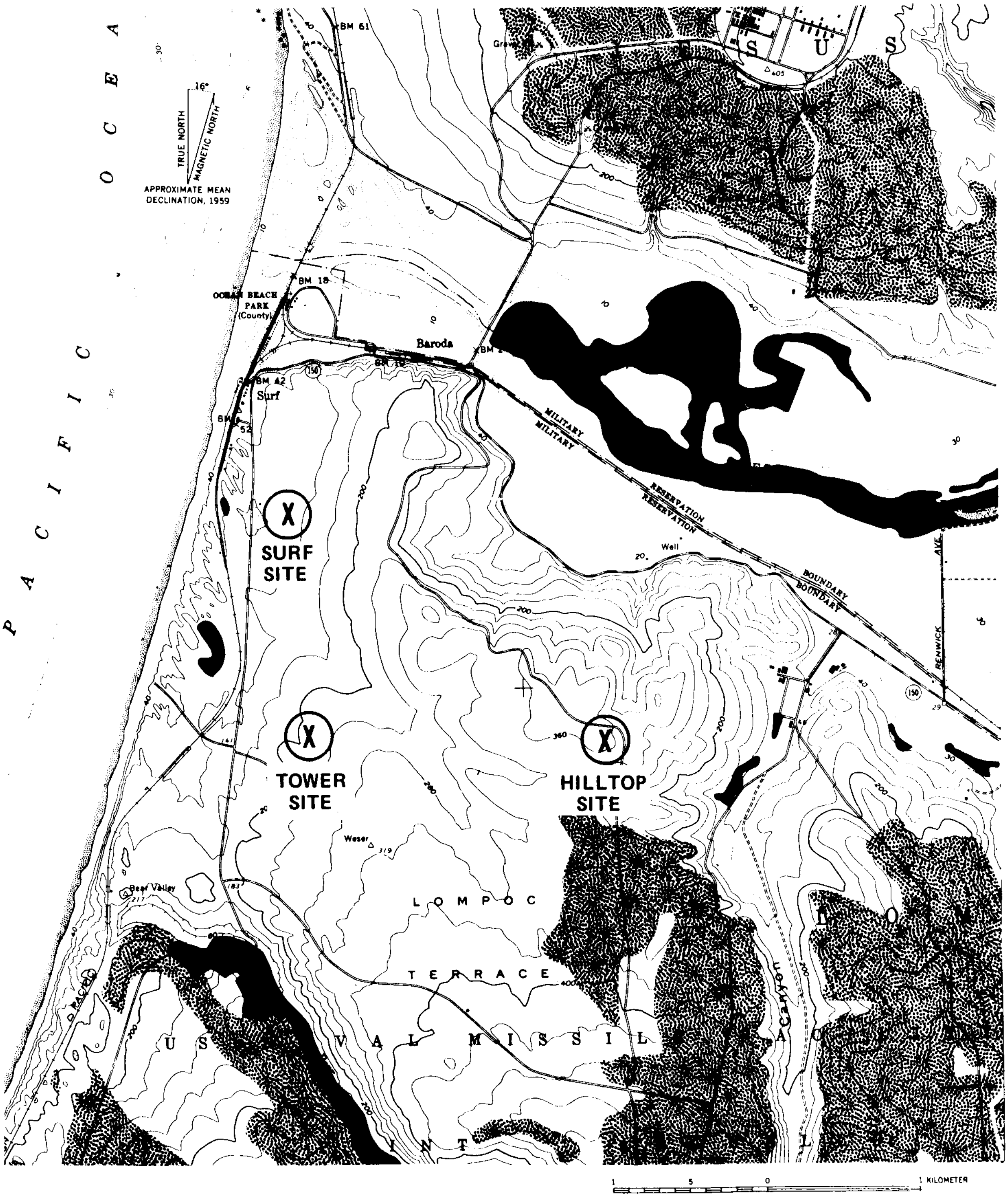

Figure 1 VANDENBERG FIELD SITE

Additional transmissometers were located at the 1.2 ±0.2 m level at the two secondary sites: one located near Building 980 (Surf), 0.75 km inland at 35 m MSL; and the second located near Building 900 (Hilltop), three kilometers inland at 105 m elevation. The drop sampler and Gelman were occasionally transported to secondary sites for specific observations.

Temperature, dew point, horizontal and vertical wind and visibility were recorded continuously throughout the field program. Measurements of drop size, drop concentration, liquid water content, cloud and haze nucleus concentration and dew deposition were obtained at varying intervals before, during, and after episodes of fog.

2. The Los Angeles Field Site

The Los Angeles field site was located on the grounds of Los Angeles International Airport adjacent to the Pacific Ocean as shown schematically in Figure 2. Our principal data acquisition site was the ASDE radar tower (Tower site), which is approximately 43 m high and located about 2.5 km inland from the shoreline at the center of the airport between the active runways. At this location, we placed temperature and dew sensors at 1, 5, 11, and 38 m, wind vanes and anemometers at 5 and 38 m, a slant range transmissometer (1-38 m) and a transmissometer for measuring horizontal visibility at the surface. Average surface elevation for the airport and the ASDE Tower site is approximately 38 m MSL.

Two additional transmissometers were located off the west end of the runways approximately 1.8 km apart and each approximately 0.7 km from the shoreline. These protected sites (VOR and Localizer) provided good spatial distribution for visibility measurements and convenient locations for acquiring surface data in fog. The VOR site was situated at 58 m MSL atop a large sand dune which runs parallel (~0.7 km inland) to the shoreline for several tens of kilometers. The Localizer site was located on the inland side of and near the base of the dune at approximately 30 m MSL.

Because of the proximity of buildings, air and vehicular traffic, and asphalt pavement surrounding the ASDE tower site, surface observations were generally made at the VOR site. Except for surface temperature, which

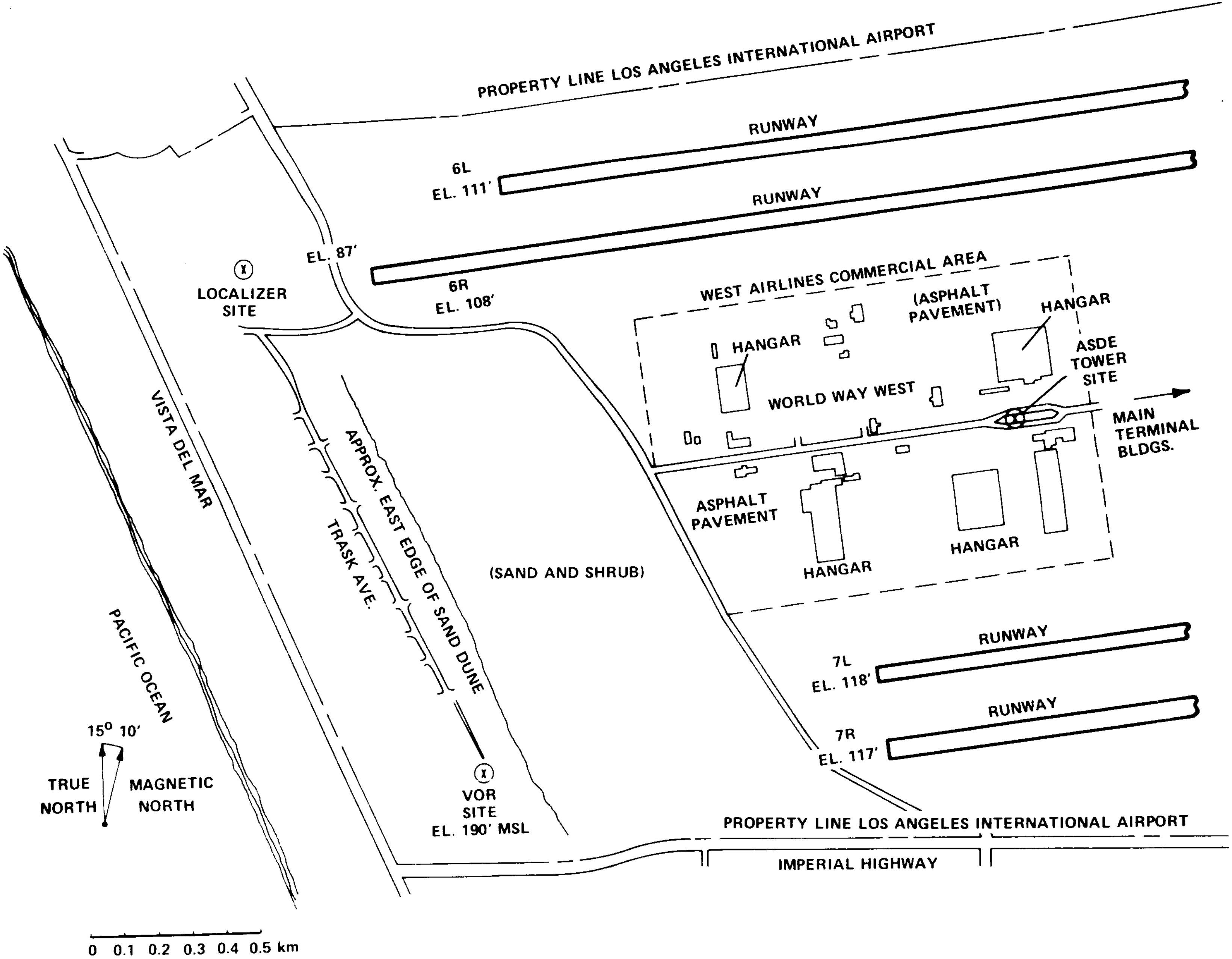

Figure 2 SCHEMATIC DIAGRAM OF LOS ANGELES FIELD SITE

was measured at the ASDE location, all the surface-based instrumentation described previously for use at Vandenberg was utilized at the VOR site in Los Angeles.

3. Description of Field Instrumentation

- Transmissometers

Visibility data were acquired from CAL-designed transmissometers located at three sites at each location as indicated in Figures 1 and 2. The transmissometers were operated over 30 m path lengths at a height of 1.2 m above the surface. Each instrument was adjusted in situ to provide a measured transmitter beam width of less than 1°. Maximum overall error in the measurement of received light intensity was estimated to be ±5%, with the greatest limitation being imposed by the accuracy of the recorder (±1% full scale) at the lowest visibilities. This error is negligible in the low visibility region; e.g., at 1000 ft visibility, an error of ±5% in the measurement of received light produces an error of only ±100 ft in visibility. To minimize error due to drift in the transmissometers, a reference signal was generated by inserting a prism into the transmitted beam to reflect a fixed fraction of the transmitted light into a second phototube mounted in the transmitter. The reference phototube was operated from the same power supply as the receiver and its output was passed through the receiver electronics. Reference signals were recorded for 20-second intervals every three minutes.

Continuously recorded transmissometer data were converted to meteorological visibility V in the standard manner. That is,

$$I = I_0 e^{-\beta x} \tag{1}$$

$$V = \frac{3.912}{\beta} \tag{2}$$

where I and I_0 are observed light intensities at the receiver after transmission through the turbid and clear media respectively, x is the transmission path length (30 m in this case) and β is the extinction coefficient. Conversions were made at discrete times determined by changes in transmission characteristics or to coincide with the acquisition of drop samples.

- Wind Speed and Direction Instrumentation

The primary measurements of wind speed and direction were made at two levels at the Tower sites (10 and 32 m at Van; 5 and 38 m at LAX) using Packard Bell W/S 100 (B series) wind systems. Factory performance characteristics for the anemometers in these systems are 0.25 m $\sec^{-1}$ threshold speed and 0.1 m $\sec^{-1}$ accuracy. Quoted characteristics for the wind vanes are 0.35 m $\sec^{-1}$ threshold and an accuracy of $\pm 3^\circ$. The vanes were field adjusted to $\pm 10^\circ$ relative to true north using a transit with an integral compass.

- Low Level Temperature Instrumentation

Low level temperature data were acquired at five levels from the surface to approximately 35 m during the two field programs. These data consisted of continuous recordings of temperature using a Foxboro system.*

On several occasions during the field programs, the Foxboro system was calibrated against the secondary standard thermometers. The calibrations were performed in fog and on cloudy days by temporarily mounting the secondary standards at each resistance probe level and comparing manually observed temperature with the strip chart recordings. After appropriate fixed corrections were applied to the records, agreement was within 0.2°C (absolute) and within 0.1°C (relative) for a single resistance probe over periods of hours. In general, therefore, we estimate that all relative temperatures are good to $\pm 0.2^\circ$C on a given day.

- Low Level Dew Point Instrumentation

Dew point was measured at the same levels as was temperature (except for the surface measurement) and recorded continuously using a Foxboro dew point measuring system.**

---

*Dyatherm Resistance Bulb Model DB-21B-226W and Recorder Model ERB.

**Model 2701 RG Dynalog Dewcel Element and associated electronics with ERB 6 Multipoint Recorder.

The Foxboro system was factory-calibrated. Perhaps the best indication of the absolute accuracy of this system rests in the extensive observations of Elmira valley fog (Pilié et al., 1972). These observations showed that the mean difference between indicated temperature and indicated dew point at the time of fog formation was 0.3°C for the eleven cases available. In eleven cases studied, the maximum indicated difference was 1.0°C and in all other cases the difference was less than 0.6°C. For reasons that are not clear, the difference between T and T_d observed in Vandenberg and in LAX at the time of fog formation was consistently 0.7°C. While no instrumentation problems can be found, we suspect that a drift occurred in this Foxboro system between 1970 and 1971. Purely on the basis of internal consistency of the data, it appears that the dew points are accurate to ±1.0°C in an absolute sense and probably better relative to one another.

- Vertical Wind Instrumentation

Vertical wind velocity and direction were measured with a lightweight propeller anemometer* mounted in the vertical position at approximately 35 m above the surface at the Tower sites in both Los Angeles and Vandenberg. These data were recorded continuously from the time of arrival of the field crew until after fog dissipation.

- Drop-Size Measurement Instrumentation

Measurements of drop-size distribution were obtained using a modified Bausch and Lomb slide projector to expose gelatin-coated slides to a stream of foggy air. In operation, droplets in the air stream were impacted on the treated slides to leave permanent, well-defined "replicas" that could be accurately measured under a microscope. Previous work had established that true droplet diameter is very nearly equal to one-half the diameter of the crater-like impressions left in the gelatin.

---

*Gill Model No. 27100

The apparatus used at the Tower site and operated at the same level as the transmissometer (i.e., 1.2 m) was designed to permit control of exposure time from less than 0.1 sec to periods of several minutes and selection of air stream velocity (by a speed control on the blower motor) between 10 and 70 m $\sec^{-1}$. To provide for greater accuracy in applying collection efficiency corrections, air velocity was measured for each exposure of the four millimeter wide slides.

Reduction of drop-size data was performed manually from photomicrographs obtained with a phase contrast microscope. Where possible, a minimum of 200 droplets was measured for each distribution. In some cases with very low droplet concentration, all replicas on the slide were measured directly through the microscope.

Inspection of the drop-size distribution data obtained during the Elmira investigation suggests that droplets smaller than 1 μm radius could not be detected in the field even though smaller droplets can be detected in the laboratory. The principal known sources of error in these measurements are statistical in nature and imposed by the time required to measure larger numbers of replicas for each distribution. These errors are particularly important for small droplet sizes (<3 μm radius) where the number of replicated droplets is limited by small collection efficiencies and consequently collection efficiency corrections are large (Langmuir and Blodgett, 1946). Similar problems occur for large drop sizes where natural concentrations are small. A second type of statistical error is due to the lack of "representativeness" of the sample. A fog that occupies many cubic kilometers is often characterized by a few tens of samples, each containing the droplets from five to ten cubic centimeters.

While exposure time for a given sample is controllable, short exposure times (<0.5 sec) are not reproducible to within a factor of about three from slide to slide. Therefore, normalized drop-size distribution data can be obtained directly; but it is not feasible to obtain direct measurements of drop concentration from the droplet samples. Drop concentrations were obtained by combining the normalized distributions obtained at the surface (1.2 m) with simultaneous measurements of extinction coefficient obtained from the tower transmissometer (at the 1.2 m level ~30 m away) according to the following expression:

$$\beta_{transmissometer} = 2\pi n \sum_{i=0}^{\infty} N(r_i)\, r_i^2 \tag{3}$$

where $N(r)$ is the normalized distribution and n is the concentration.

- Liquid Water Content Instrumentation

Liquid water content data were acquired by integrating the absolute drop-size distribution ($\omega = 4/3\pi n \sum_{i=0}^{\infty} N(r_i)\, r_i^3$) for each drop sample and occasionally (5 to 10 times/fog) by direct measurement using a Gelman* high volume sampler for mechanical collection of the water from 8 m^3 of fog. Cellulose filters were used in the Gelman so that liquid water was absorbed into the fibers. To minimize the error due to absorption of water vapor from the humid atmosphere by the cellulose, the filters were moistened by collection of water and vapor from 2 m^3 of fog prior to the first weight measurement. The increase in weight after exposure to an additional 8 m^3 of fog was used to determine LWC. It was found in the Elmira studies that simultaneous measurements of LWC by the two methods in general, agree to within ±40 mg m^{-3} (Pilié et al., 1972). Variability appeared to be random and associated in part with the fact that Gelman data were obtained from an average of 8 m^3 of fog acquired over a seven-minute interval while the drop-size distributions were acquired from a few cubic centimeters of fog collected essentially instantaneously.

In the present investigation, the Gelman data indicated consistently larger LWC than computed values at Vandenberg and consistently smaller LWC than computed values at LAX. These deviations are quite adequately explained by additional measurements made at both sites and are discussed in detail later in this chapter.

---

*Gelman Model No. 16003

- Cloud and Haze Nucleus Instrumentation

The CAL thermal gradient diffusion chamber has been used for making measurements of cloud nuclei since about December 1964. The basic design of the chamber is patterned after that of Langsdorf (1936), Wieland (1956), and also Twomey (1963). In brief, the unit consists of a cylindrical plexiglass chamber with upper and lower water reservoirs, a collimated light beam to illuminate a small volume within the chamber, and a Polaroid camera for photographing droplets that have formed on condensation nuclei.

During operation, water vapor diffuses from the warmer upper surface to the lower reservoir, with the chamber supersaturation being a known function of temperature difference between the two reservoirs. A series of ten thermocouples (five on each surface) is used to measure ΔT. When the desired supersaturation has been achieved, an air sample containing nuclei to be investigated is drawn into the chamber at a continuous rate for several seconds. The air sample is allowed to reside in the supersaturated environment where, in a few seconds, droplet growth proceeds on the most active condensation nuclei. The growing droplets are illuminated by a 200 watt Osram lamp and photographed at 90° to the light beam moments before sedimentation begins. The concentration of active nuclei can be estimated from the photographs by counting the point images per unit area of photograph.

The haze chamber is of a similar design but employs saturated solutions of KNO_3 in place of the water. By varying the temperature gradient within the chamber, relative humidity can be controlled between 95 and 100%. Hygroscopic nuclei which deliquesce and enlarge to ~ 1.0 μm radius and larger at these humidities are illuminated by the intense ribbon of light and photographed. This instrument, which does not exist elsewhere in the United States, provides essential information on the relative activity of aerosols in terms of producing haze size droplets at humidities near saturation. The data acquired on this program demonstrate that use of instrumentation of this type is essential to the complete understanding of fog characteristics.

B. ADVECTION FOG

1. Fog Formation Characteristics

The three advection fogs that were observed at Vandenberg are considered typical of the predominant fog type of that region. No advection fogs were observed in Los Angeles. The advection fog of greatest duration occurred on 15 and 16 September 1971 and persisted for nearly 31 hours. The two other advection fogs formed in the early morning hours on 18 September and 20 September and lasted for 11 and seven hours, respectively.

- Synoptic Situation

The weather pattern for the period 15-20 September 1971 was typical for the Southern California area in the fall. The eastern edge of the eastern Pacific subtropical high was located over the coastal shoreline. At the surface, the normal thermal low extended through central California providing a weak pressure gradient field along the coast. Under these conditions, the surface wind direction near Vandenberg depends primarily on the sea breeze circulation with the onshore winds supported by the larger scale pressure gradient.

On the 15-16th, the subtropical high was ridged over the area and the surface thermal low was well-developed in northern California. These conditions permitted a westerly onshore flow. On the 18th and 20th, the subtropical high had shifted westward and the ridge aloft was replaced by a weak trough. At the surface, the thermal low center had shifted southeastward, and the surface pressure pattern was conducive to north-northwesterly onshore flow in the vicinity of Vandenberg. Thus, the onset and persistence of advection fogs which occurred at Vandenberg in September 1971 were related to large-scale surface and upper air flow patterns.

- Visibility Characteristics

Horizontal visibility was measured at three sites from CAL-designed 30 m baseline transmissometers. A fourth transmissometer was oriented vertically on the 30 m tower in order to provide measurements of visibility in the lowest 30 m of fog. This instrument was put into operation prior to the fog of 18 September.

The visibility data obtained during the advection fogs of 15-16, 18, and 20 September are shown in Figures 3, 4, and 5, respectively.* The figures are organized such that visibilities measured at each of four elevations on the coastal slopes are shown in order of descending altitude. Note from the visibility records the nonuniform patchy nature of the fogs. Except for measurements recorded at the Hilltop site, visibility was rarely < 500 m. At the Hilltop site, visibility occasionally dropped to about 300 m.

These data also show that during the three advection fogs visibility generally degraded first,and visibility restriction was always most severe, at higher elevations. Note that the fogs were most dense at the Hilltop site (105 m MSL), of lesser density between 60 and 90 m (vertical visibility), and even less dense near the surface (60 m MSL) at the Tower site. Transmissometer observations of visibility at the Surf site (35 m MSL) in the fogs of 18 and 20 September show that fog was least dense at that site. At that lower level, visibilities remained greater (by a factor of approximately two) than that measured at the Tower site in each of the advection fogs for which data were available.

2. Micrometeorological Data

- Low Level Winds

Wind speed and direction were recorded continuously prior to, during, and after the three occurrences of advection fog observed at Vandenberg. These data have been reduced to ten-minute averages for each half-hour interval. Wind speed was measured to the nearest 0.5 m sec^{-1} and wind direction was read to the nearest ten degrees.

---

*With the 30 m baseline, the least count of the transmissometers was such that visibility in excess of about 4500 m was not distinguishable from infinity. The dashed portions of the curves simply indicate that visibility exceeded that value.

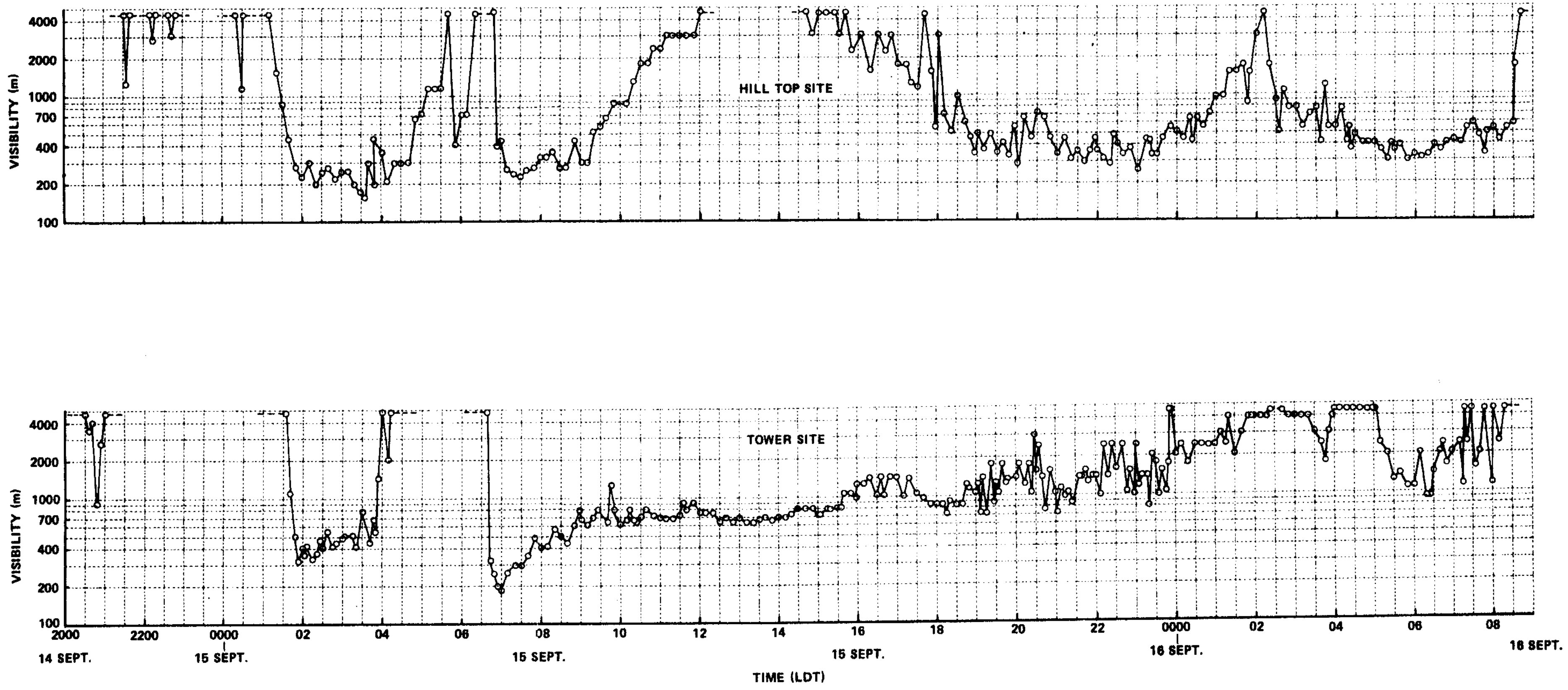

Figure 3 VISIBILITY AS A FUNCTION OF TIME, 15-16 SEPTEMBER 1971

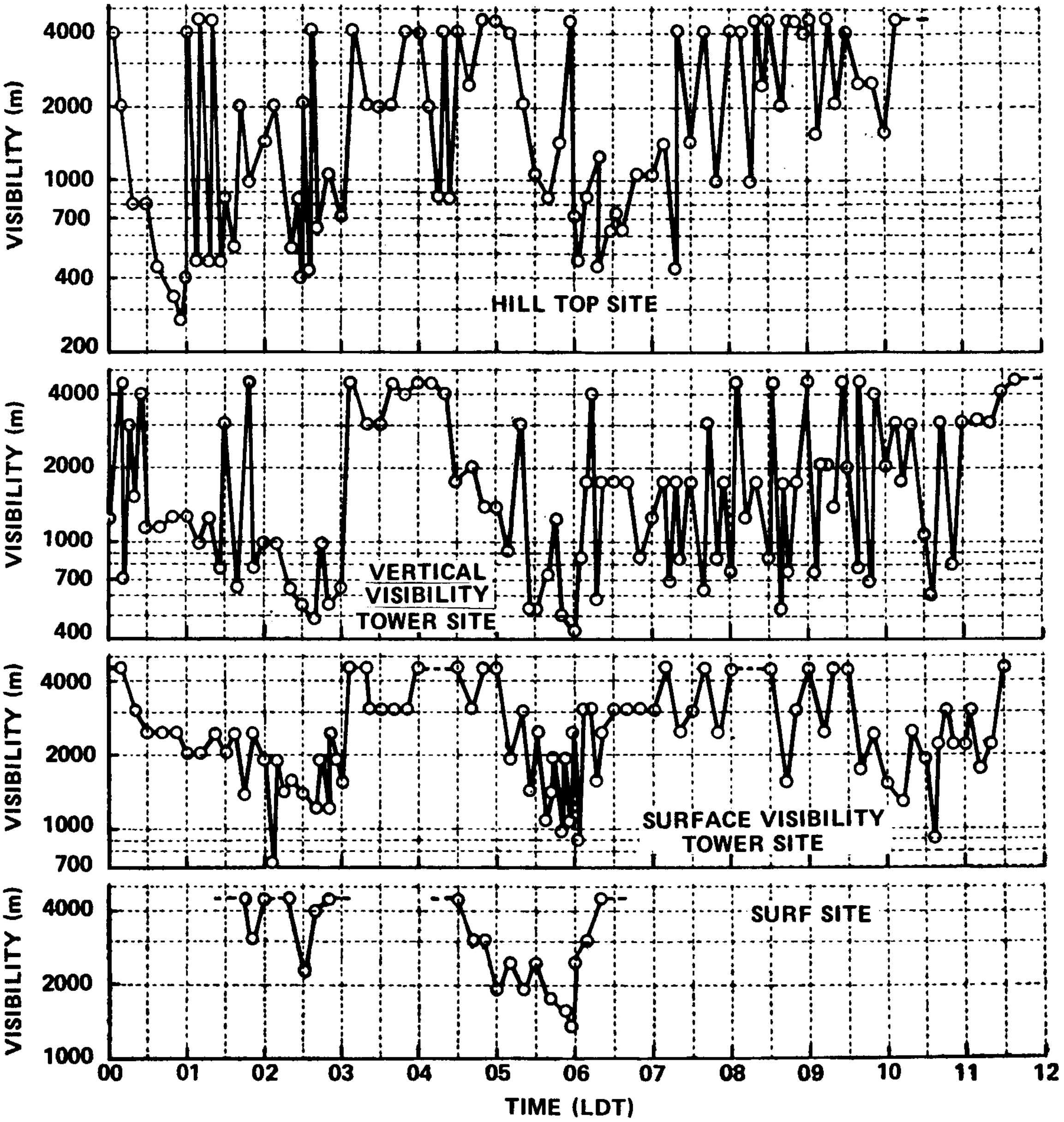

Figure 4 VISIBILITY AS A FUNCTION OF TIME, 18 SEPTEMBER 1971

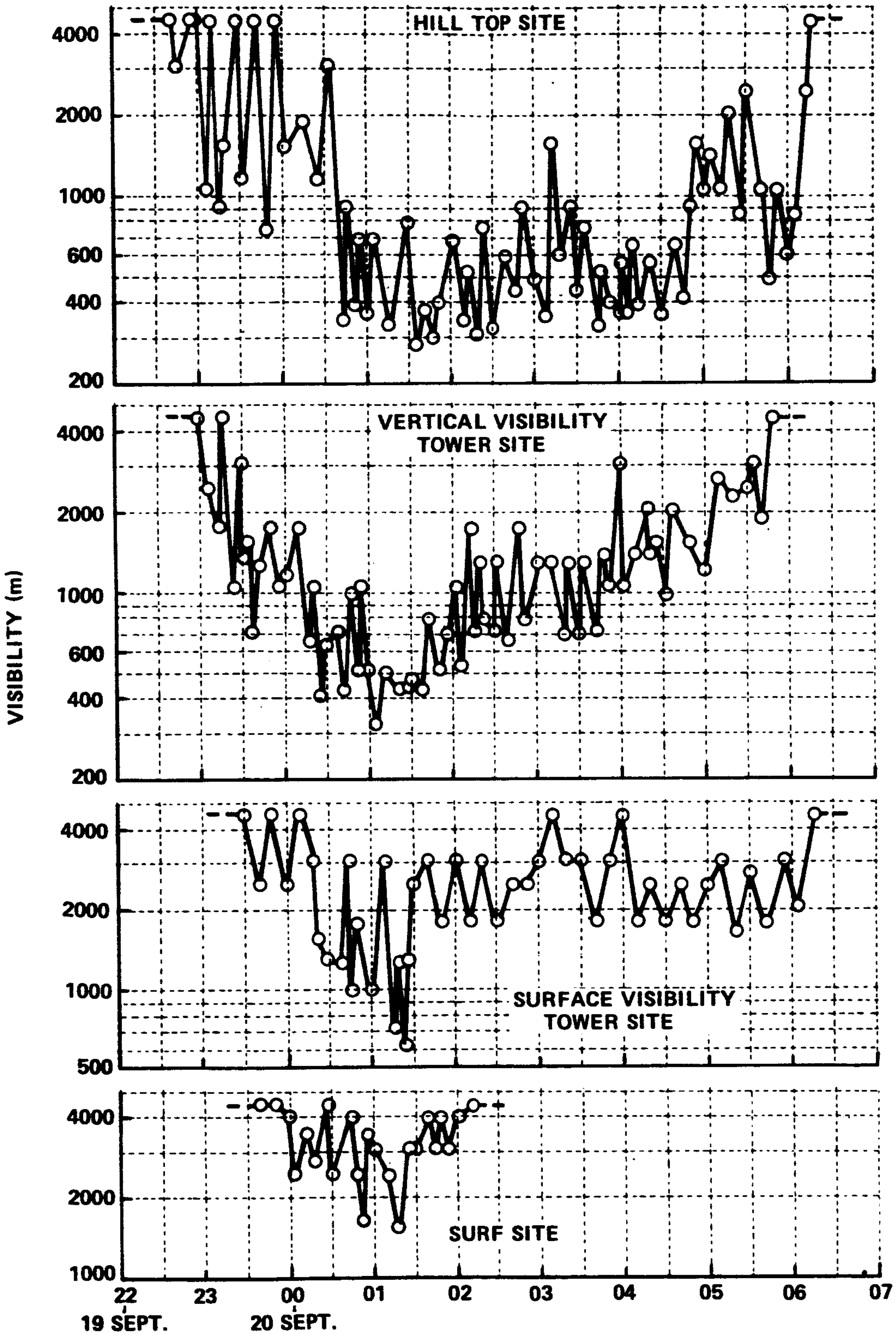

Figure 5 VISIBILITY AS A FUNCTION OF TIME, 19-20 SEPTEMBER 1971

The wind data for the advection fogs of 15-16, 18, and 20 September are presented in Figures 6, 7, and 8, respectively. Note from the data that winds during these three advection fogs were light and variable. Wind speed typically ranged from one to three meters per second, and occasional periods of calm were recorded. Because of the very low wind speeds, wind direction was highly variable at times.

A comparison of the visibility records (Figures 3, 4, and 5) and wind data obtained during episodes of advection fog reveals a consistent correlation between wind direction and the presence of fog at the Tower site. During periods of fog, wind speeds were generally greatest (i.e., ~ 3 m sec^{-1}) and wind directions were typically onshore (i.e., 210° to 360° true).

The correlation of wind with the advent of fog is particularly evident from the records of 15-16 September and 18 September. Note, for example, that as wind speed increased and wind direction shifted from northeast to southwest (onshore) at both 0000 and 0600 on 15 September and from northeast to northwest (onshore) at 0000 and 0500 on 18 September, fog appeared at the Tower site one-half to one hour afterwards. An increase in wind speed and a shift in direction from northeast to northwest is also apparent prior to the appearance of fog (at the Tower site) on 20 September.

Fog dissipation was also correlated with low level wind direction. Note, for example, that the disappearance of fog at the Tower site at 0430 on 15 September, 0800 on 16 September, 0400 on 18 September, and 0600 on 20 September was preceded in each case by a wind shift. The exception to this correlation occurred during fog dissipation at mid-morning on 18 September. Undoubtedly (as will be shown in the next subsection), surface warming during mid-morning hours contributed to,or was wholly responsible for,final fog dissipation on both 16 and 20 September as well as on 18 September.

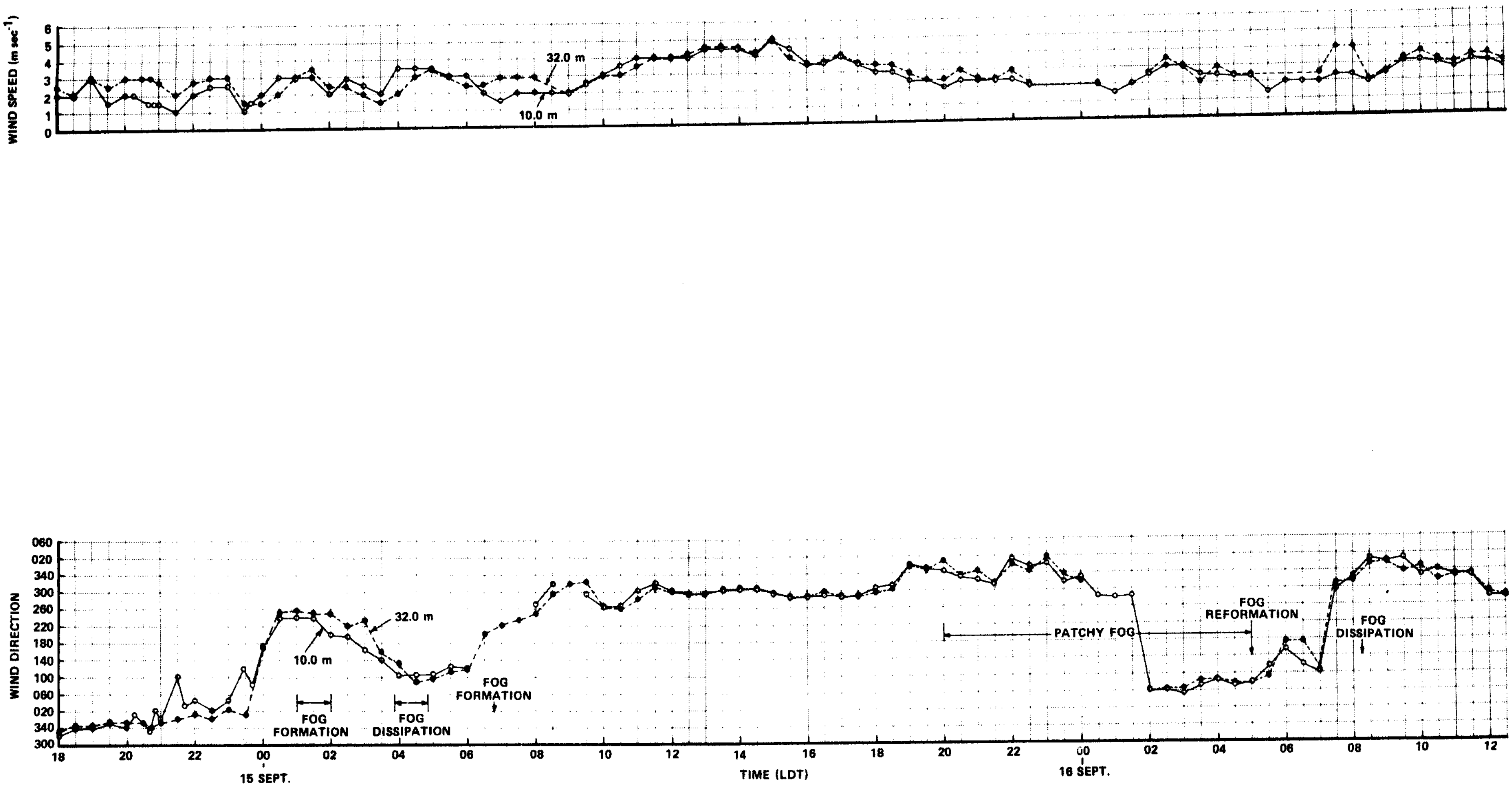

Figure 6 WIND SPEEDS AND DIRECTION AS FUNCTIONS OF TIME, 14-16 SEPTEMBER 1971

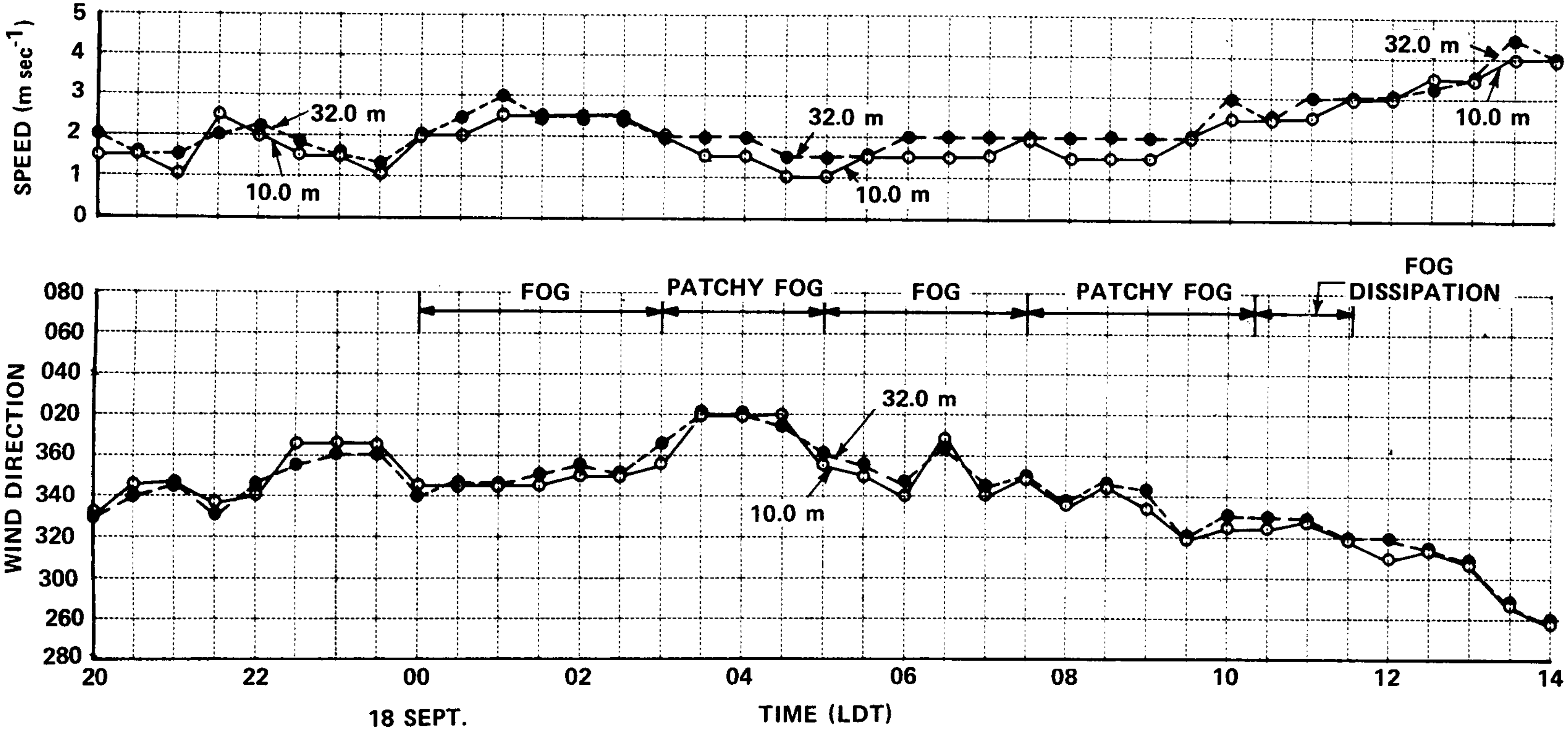

Figure 7 WIND SPEED AND DIRECTION AS FUNCTIONS OF TIME, 18 SEPTEMBER 1971

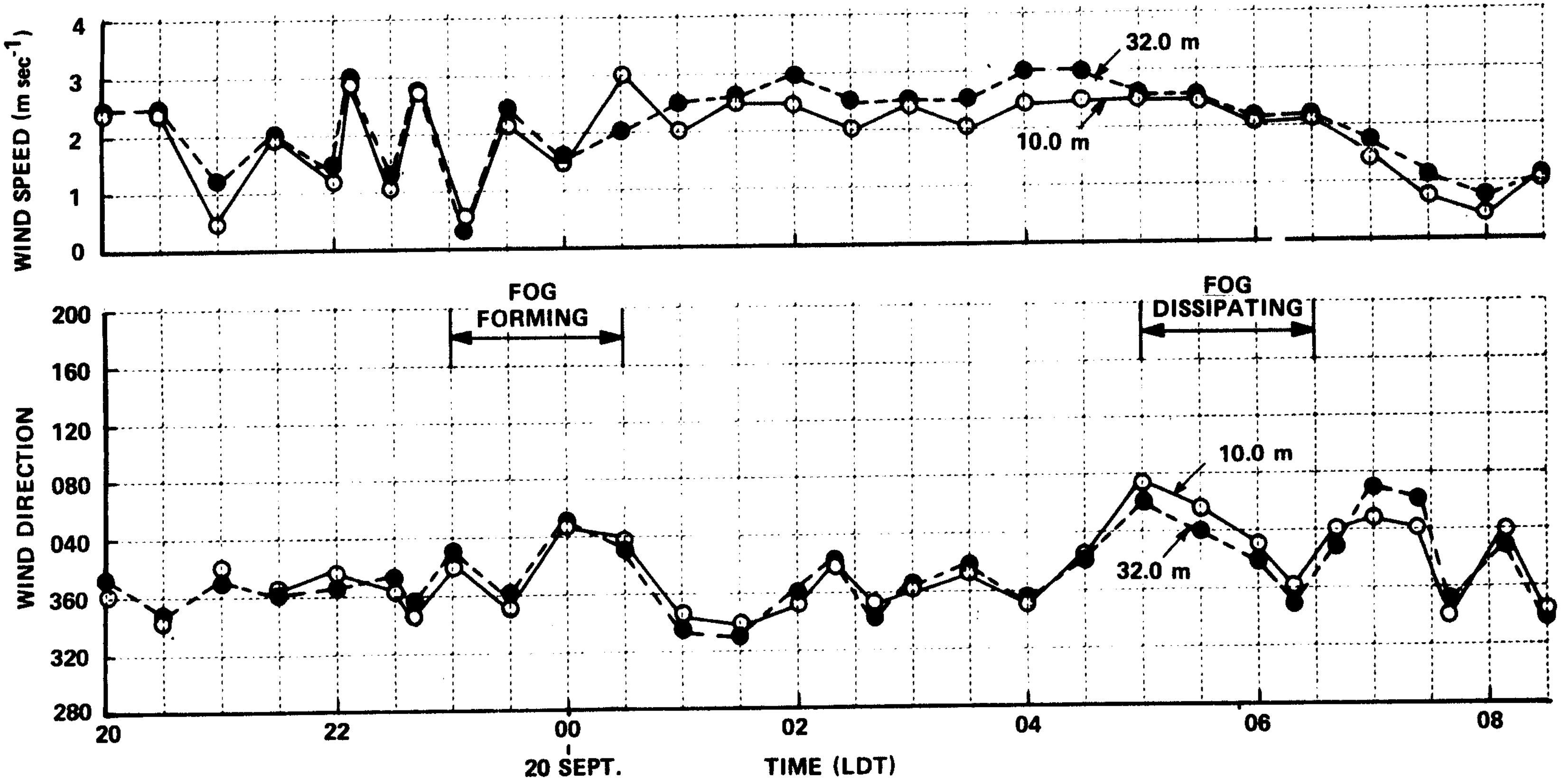

Figure 8 WIND SPEED AND DIRECTION AS FUNCTIONS OF TIME, 20 SEPTEMBER 1971

- Low Level Temperature and Dew Point Data

Temperature and dew point data obtained during the three occurrences of advection fog are shown in Figures 9, 10, and 11. The data represent ten-minute averages of temperature and dew point taken at half-hour intervals. Several consistent features of the low level temperature structure are evident from these data. Note the striking similarities between the temperature records and the rather uniform vertical temperature structure for the three occurrences of advection fog.

Lapse conditions prevailed between the surface and 32 m throughout the pre- to post-fog periods in the three Vandenberg advection fogs. Surface temperature remained warmer than air temperature and the 32 m temperature remained colder than that at lower levels. Superadiabatic lapse rates of 2-3°C m^{-1} were common in the lowest one meter. Between 1.0 and 10.0 m the vertical temperature structure was, within the accuracy of the measurement, essentially isothermal; however, in the region between 10 and 32 m, superadiabatic lapse rates of 1.5°C to 3.5°C per 100 m were typical.

Surface and lower level temperatures remained warmer than higher level temperatures throughout pre- to post-fog period. The warm surface temperatures indicate that, for several hours prior to the appearance of fog at the surface, radiational cooling at the surface was substantially reduced or prevented, most likely by stratus aloft. Thus, radiational cooling probably did not contribute appreciably to formation of the observed advection fogs. This observation was further substantiated by the fact that dew did not form on nights when advection fog occurred. Note also that at the times when fog appeared, no change was observed in the vertical temperature structure while visibility gradually degraded downward from higher levels (Hilltop) to lower (Tower base) levels.

As shown by Figure 9, significant radiational cooling under clear skies preceded the appearance of fog at the Tower site on 15 September. While this cooling certainly helped establish low level conditions in which fog could exist, it does not appear to have been the primary cause of the occurrence of fog. As seen in Figures 3 and 6, fog had appeared at the Hilltop first at 0110 and then at the surface Tower site in response to low level wind shifts.

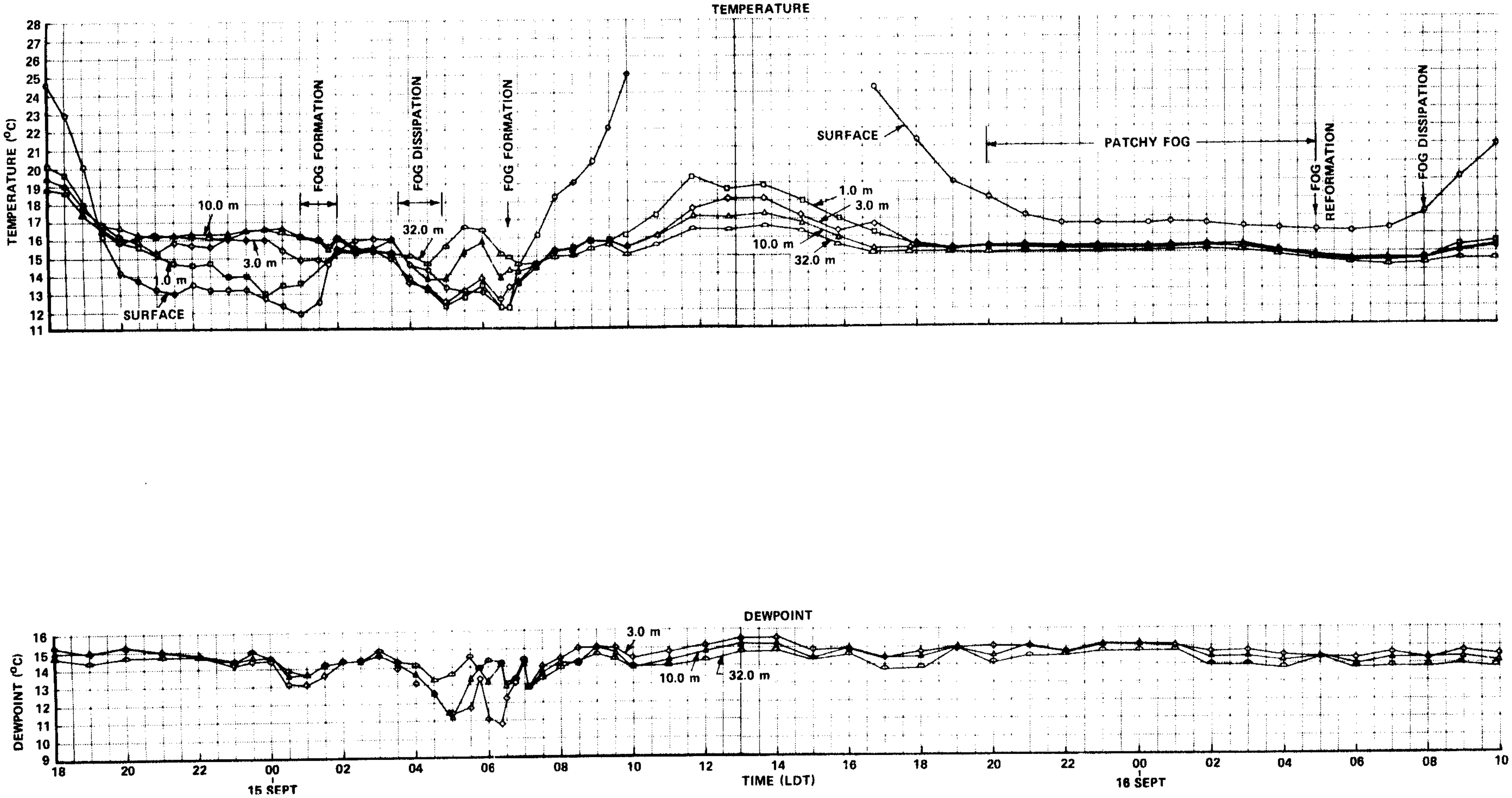

Figure 9 TEMPERATURE AND DEWPOINT AS FUNCTIONS OF TIME, 14-16 SEPTEMBER

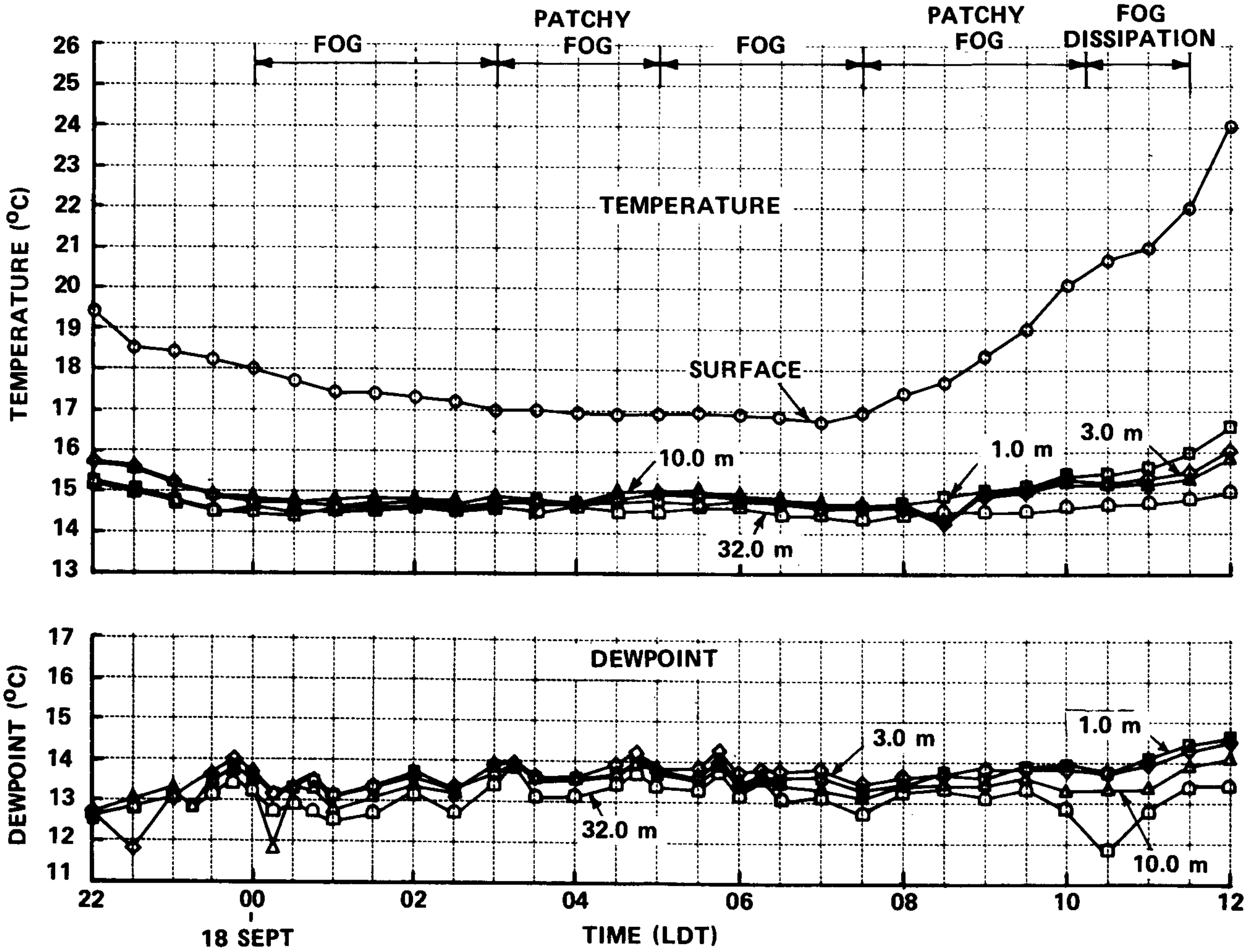

Figure 10 TEMPERATURE AND DEWPOINT AS FUNCTIONS OF TIME, 18 SEPTEMBER 1971

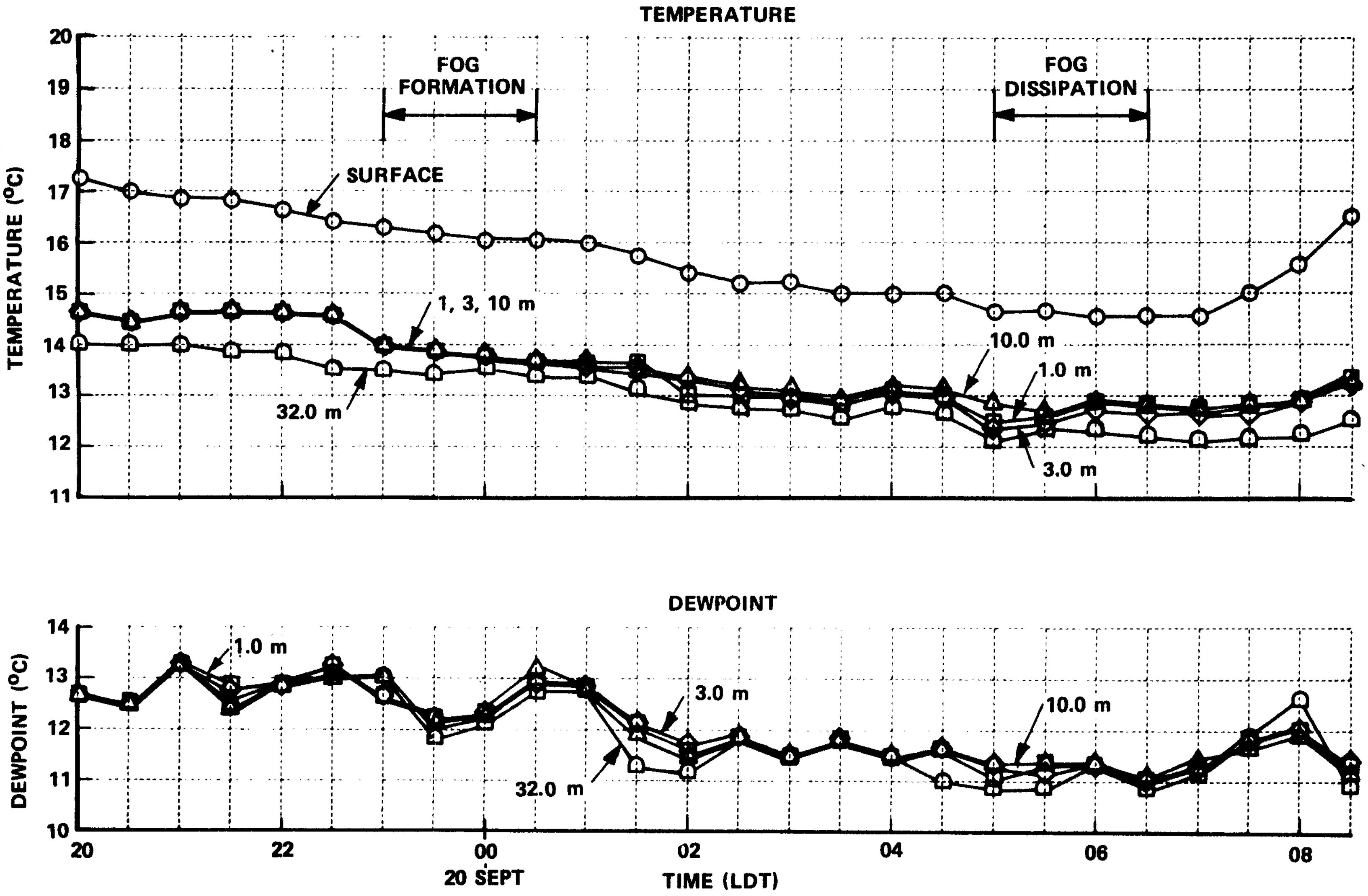

Figure 11 TEMPERATURE AND DEWPOINT AS FUNCTIONS OF TIME, 20 SEPTEMBER 1971

Increased surface warming during early and mid-morning hours apparently contributed substantially to final fog dissipation in all cases. While it has been shown that these advection fogs appeared and disappeared in response to synoptic scale features and low level wind direction, it is also apparent that surface visibility began to improve in response to surface warming after sunrise. Warm surface temperatures during episodes of advection fog no doubt contributed to increased vertical mixing, evaporation of fog droplets nearest the surface, and subsequent improvement of surface visibility.

Typically, dew point remained constant throughout the pre- to post-fog periods. The vertical profiles of dew point temperature exhibited features similar to those of temperature. The dew point profile ranged from isothermal to an average lapse of about 1.5°C per 100 m in the lowest 32 m. Long-term (1-6 hrs) fluctuations of the order of 1-2°C were observed but appeared to be independent of temperature or the occurrence of fog.

- Vertical Wind Data

The vertical wind anemometer was not installed until after the fog of 15-16 September. However, complete records of vertical wind velocity and direction were obtained during the advection fogs which occurred on 18 and 20 September. These data indicate that during periods of onshore (up slope) wind, persistent upward motion prevailed on the coastal slopes of Vandenberg. Before sunrise, these peak upward velocities were most intense when horizontal wind speed was at a maximum. For example, between 0000 and 0300 on 18 September, when horizontal winds were from 350° (onshore) at 2.5 m $\sec^{-1}$, average vertical wind speed was +0.2 m $\sec^{-1}$ and frequent gusts to +0.5 m $\sec^{-1}$ were recorded. Later, when horizontal winds had subsided and shifted to the northeast, vertical velocity also subsided to a mean of approximately zero. During the hour prior to sunrise (approximately 0700), vertical gustiness increased without altering the mean. Several hours after sunrise, peak up- and downdraft velocities in excess of 1.2 m $\sec^{-1}$ were recorded.

Vertical wind data obtained during the fog of 20 September exhibit similar trends. Between 0100 and 0430 when surface winds were steady (2.5 m sec^{-1}) and onshore (340° to 360°), nearly continuous upward motions of approximately 0.34 m sec^{-1} were observed. Peak updraft velocities frequently exceeded 1.0 m sec^{-1}. Again, during periods of light offshore wind vertical velocities subsided to less than 10.0 cm sec^{-1}. After sunrise, peak up- and downdraft velocities in excess of 1.5 m sec^{-1} were observed.

3. Microphysical Characteristics of Advection Fog

Manual measurements of fog microphysics were obtained at varying intervals throughout the life cycles of the three advection fogs which occurred at Vandenberg during the field program. Attempts were made to measure drop-size distribution, drop concentration, LWC and nucleus concentration at intervals varying from several minutes to several hours. Evaporation of fog at the lowest levels because of warm surface temperatures occasionally prevented data acquisition at desirably frequent intervals.

- Drop-size Distributions

Observations indicate that a continuous light drizzle (drops up to 100 μm radius) frequently accompanies the advection fogs at Vandenberg. An attempt was made to measure drizzle precipitation rates with the dew deposition instrument. Although drizzle was observed to be more or less continuous during advection fog, measurements were recorded only between 2000 and 2400 on 15 September and between 0045 and 0300 on 20 September. Measured precipitation rates ranged from 39 to 88 g m^{-2} hr^{-1} (averaging 56 g m^{-2} hr^{-1} over the period) on 15 September to 13 g m^{-2} hr^{-1} on 20 September. The presence of these large drizzle drops (radius > 20 μm) was due in part to the presence of large sea-salt nuclei and also to the fact that the Vandenberg advection fog is generally a low-lying, aged stratus cloud of considerable depth (i.e., >200 m), thus increasing the likelihood of droplet coalescence.

Because of the extremely low concentrations of drizzle drops (typically, 50-100 l^{-1}) relative to that of droplets of less than 20 µm radius (typically 10-20 cm^{-3}), normal sampling procedures (i.e., with the drop sampler) were not adequate for measurement of the drizzle portion of the drop-size distribution. An attempt was made to measure the drizzle (fallout) drop-size distribution by means of gelatin-coated slides located in the vicinity of the drop sampler. Although drizzle was observed to be more or less continuous during episodes of advection fog, the qualitative nature of these fallout measurements did not warrant a regular sampling procedure. These data*, along with the drop-size distributions obtained with the drop sampler, are presented in normalized form for the fogs of 15-16, 18 and 20 September in Figures 12, 13 and 14, respectively.

While usable data were not obtained frequently enough to reveal life cycle variations, the drop-size distributions are remarkably consistent between fogs. The typical advection fog drop-size distribution is rather broad but consistently peaked at a radius between 4-10 µm; approximately 60-70% of the drops were in that size range. The one distinguishing characteristic of the Vandenberg advection fog drop population is the tail (produced by the drizzle drops) which frequently extends the drop-size distribution to 80 µm radius and beyond.

- Liquid Water Content

The presence of drizzle was found to be a major influence on fog LWC. While the concentrations of drizzle drops (radius >20 µm) were typically only 0.1 - 1.0% of the total, the drizzle accounted for a significant portion of the fog LWC. Direct comparisons of LWC in drizzle, as computed from fallout slides, with total LWC obtained with the high volume sampler are possible in a few cases only. Invariably, these comparisons indicate that 50-75% of the total water is contained in droplets with radius exceeding

---

*Drizzle drop-size distributions were obtained by counting all drops (> 20 µm) in a given area on a slide, applying appropriate terminal velocity corrections to each size category and normalizing.

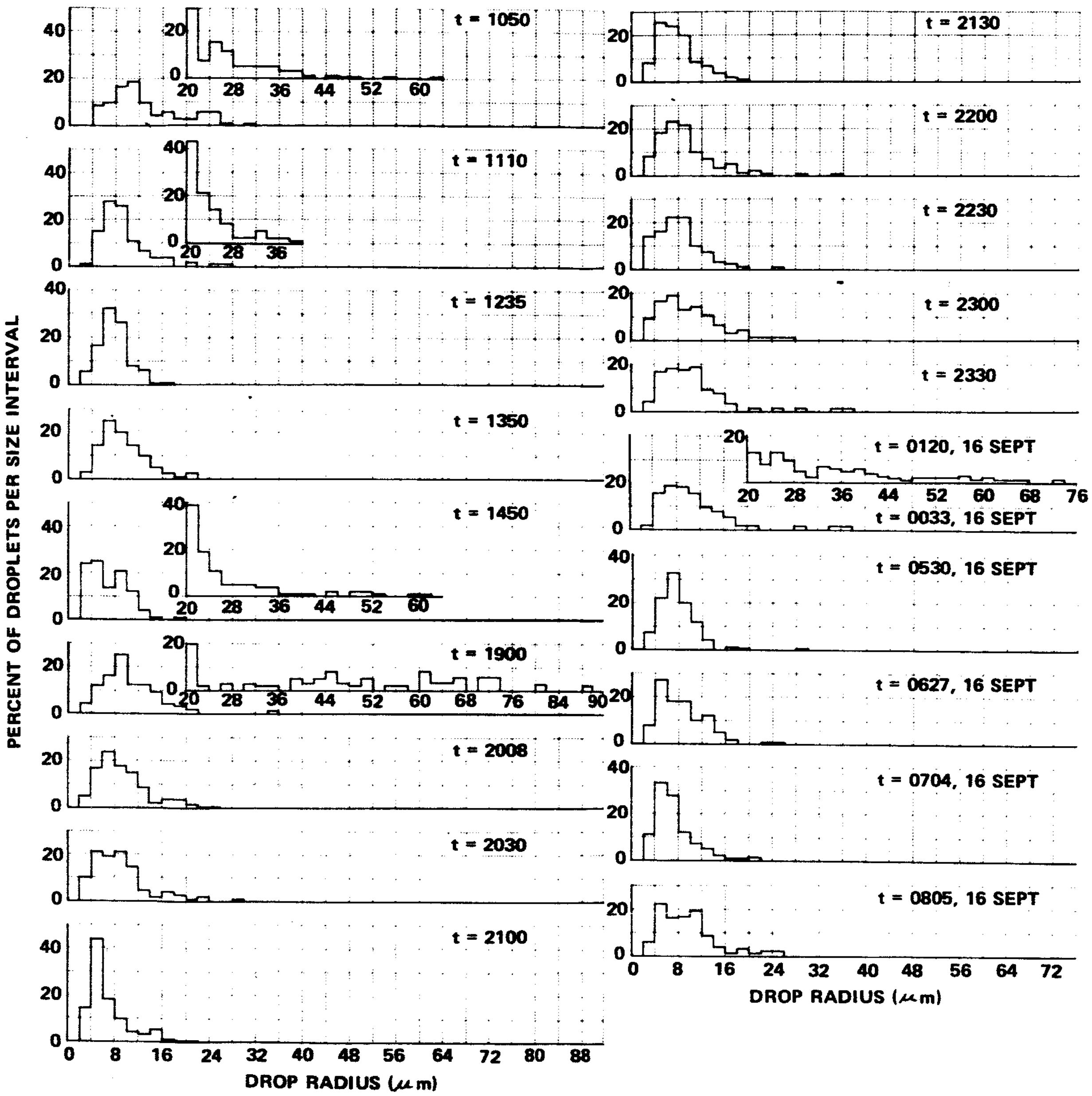

Figure 12 NORMALIZED DROP SIZE DISTRIBUTIONS OBTAINED IN THE ADVECTION FOG OF 15-16 SEPTEMBER 1971

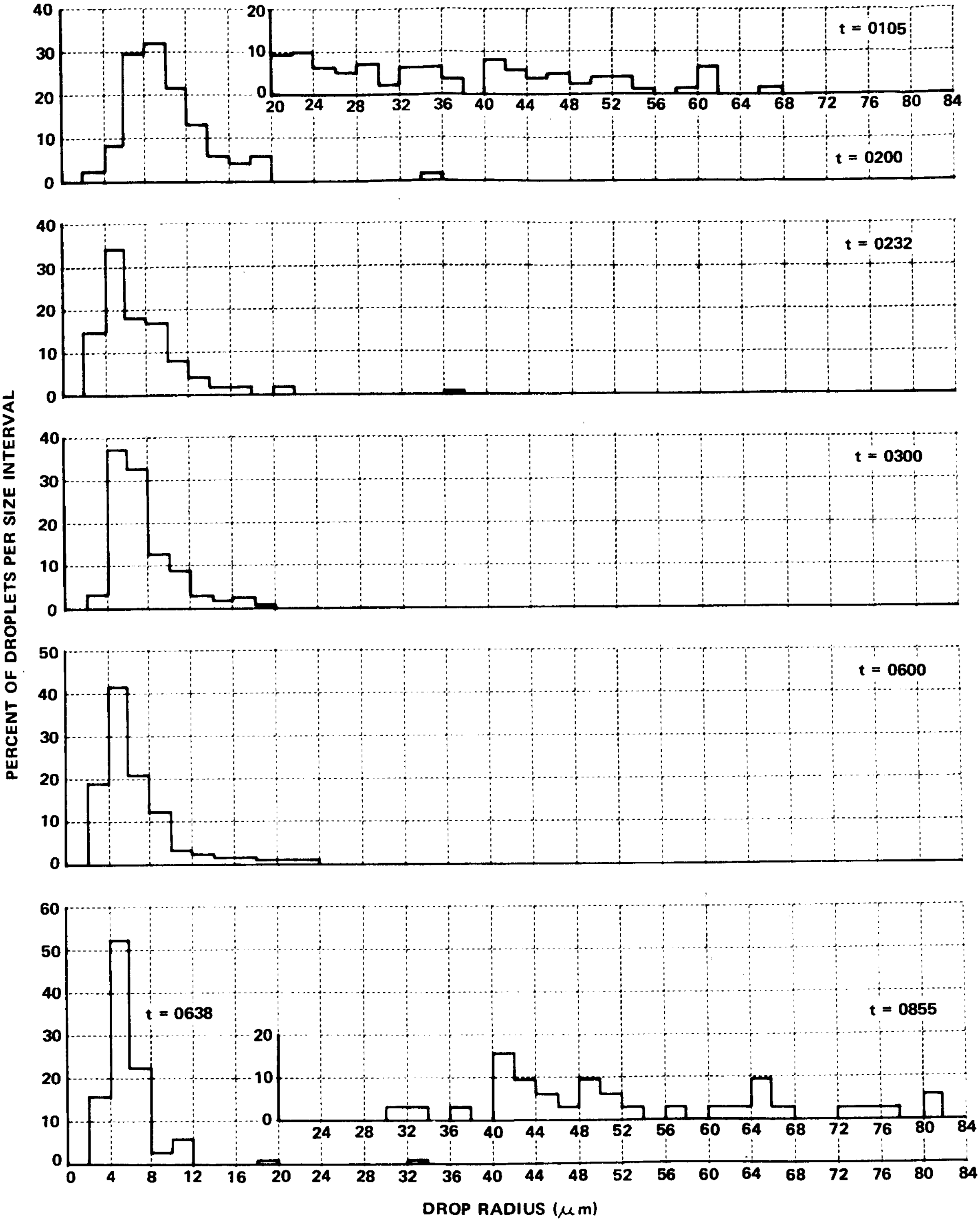

Figure 13 NORMALIZED DROP SIZE DISTRIBUTIONS OBTAINED IN ADVECTION FOG OF 18 SEPTEMBER 1971

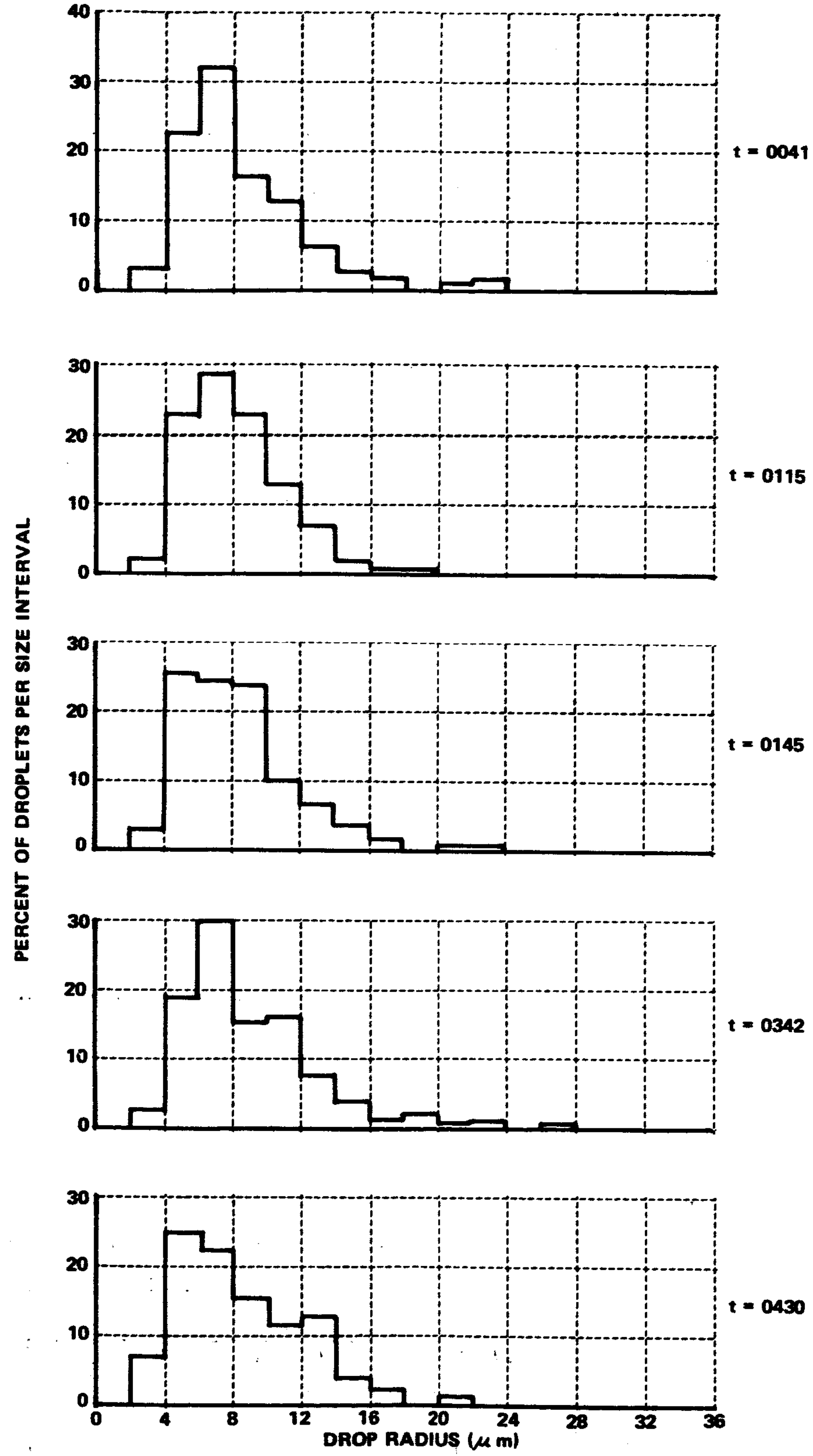

Figure 14 NORMALIZED DROP SIZE DISTRIBUTIONS OBTAINED IN ADVECTION FOG OF 20 SEPTEMBER 1971

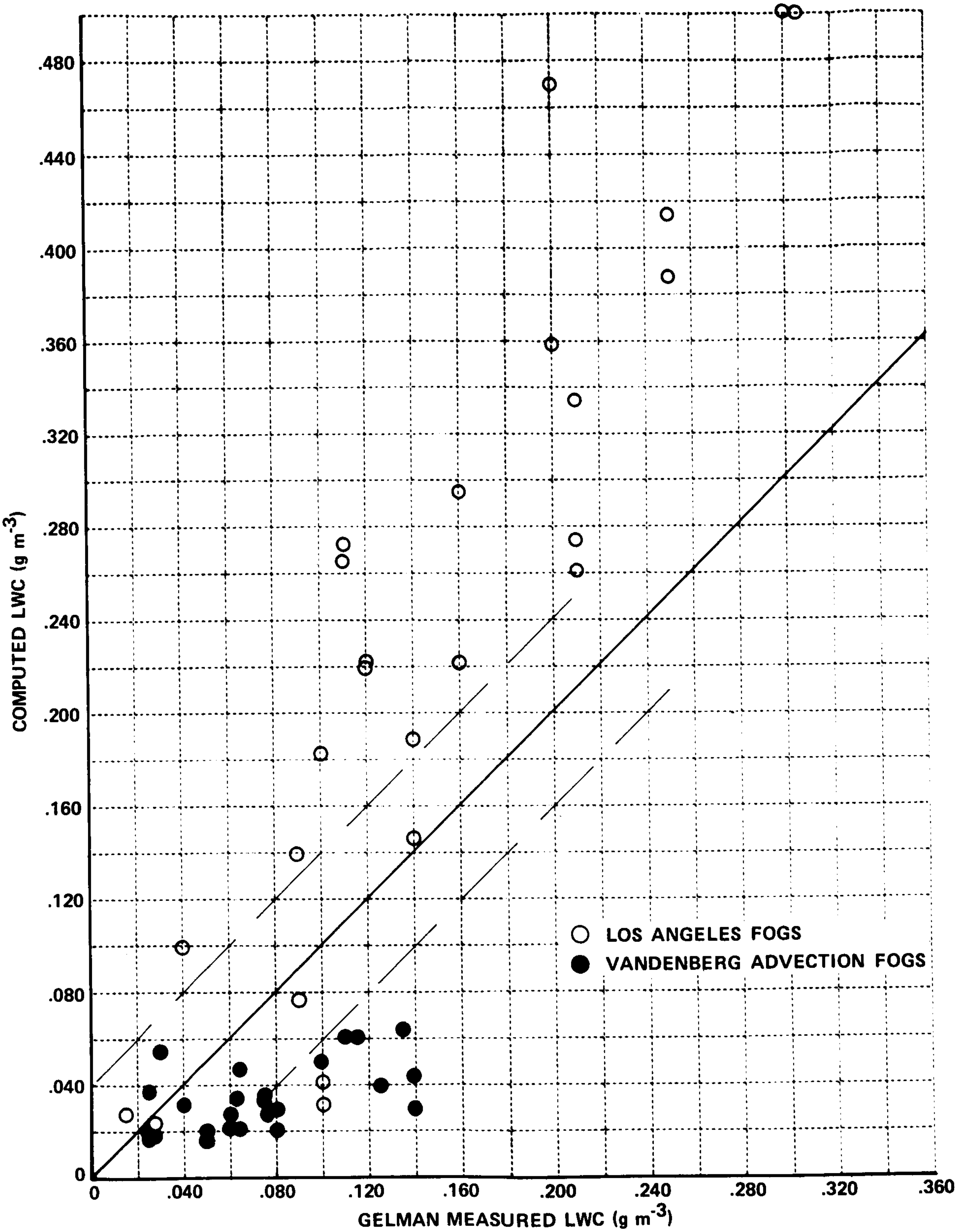

Figure 15 A COMPARISON OF LIQUID WATER CONTENT MEASUREMENTS MADE WITH A HIGH VOLUME SAMPLER AND SIMULTANEOUS VALUES OBTAINED BY INTEGRATING THE ABSOLUTE DROP SIZE DISTRIBUTION

20 µm. In Figure 15, the data obtained with the high volume sampler are compared with LWC computed from the measured drop size distribution.

In examination of Figure 15, the reader should recall that the initial step in computation of LWC is the determination of absolute drop concentration from the expression:

$$n = \frac{\beta_{Trans}}{2\pi \sum_{i=0}^{\infty} n_i(r_i)\, r_i^2}$$

where $n_i(r_i)$ is the fraction of drops with radius = r_i.

The denominator may be rewritten as

$$2\pi \left\{ \sum_{i=0}^{20} n_i(r_i)\, r_i^2 + \sum_{i=20}^{\infty} n_i(r_i)\, r_i^2 \right\}$$

For the purposes of this illustration, suppose that the droplets of r < 20 µm are all of r = 8 µm and are 100 times more abundant than the drops of r > 20 µm. Let the larger droplets be uniformly of r = 40 µm. The relative contribution of the two terms in the denominator would then be 4:1. If, in the computation, the larger drops are neglected, the computed drop concentration would be too large by about 20%.

The computation of liquid water content would then proceed using the expression:

$$LWC = 4/3\,\pi n \left\{ \sum_{i=0}^{20} n_i(r_i)\, r_i^3 + \sum_{i=20}^{\infty} n_i(r_i)\, r_i^3 \right\}$$

By neglecting the larger drops and using the value of n which is 20% too large, the estimate of liquid water content will be a factor of two smaller than the actual value.

The computations presented in Figure 15 are closely approximated by the illustration presented above. Note that the computed values for Vandenberg fogs are uniformly 30 to 50% of the values obtained simultaneously from the high volume sampler. We believe from this analysis that LWC obtained with the Gelman at Vandenberg are more nearly correct than the computed values; however, more data are needed before the question can be completely settled.

Perhaps the most important result of this analysis is in demonstrating the importance of making duplicate measurements of fog characteristics using different techniques. With the present state-of-the-art of measuring microphysical properties of fog, it is necessary to intercompare measured quantities to resolve difficulties and misunderstandings that may arise from the use of a single technique.

- Nucleus Concentrations

Observations of nucleus concentration were obtained during and after the advection fogs which occurred at Vandenberg. Generally, these measurements were made during periods of north to northwest onshore winds. Typical Aitken nucleus concentrations ranged from 1000 to 2000 cm^{-3}; at 1%S, cloud nucleus concentration varied from 400 to 800 cm^{-3}; and at 0.3%S, nucleus concentration was 150 to 250 cm^{-3}. Measurements made after fog dissipation revealed nucleus concentrations similar to those observed in fog.

4. Discussion and Summary

A review of the synoptic, micrometeorological and microphysical features of the three advection fogs which occurred in the latter half of September 1971 revealed a rather consistent pattern of fog occurrence and persistence. The Vandenberg advection fog is an aged, low-lying stratus cloud that forms offshore under environmental conditions (determined by both atmospheric stability and water temperature) unique to the region. During appropriate synoptic conditions, normal land- and sea-breeze effects are enhanced, and fog can be advected onto shore areas. The advent of advection fog at the instrumented sites on 15, 18, and 20 September was clearly in response to low-level wind shifts to onshore.

Visibility measurements obtained at a number of altitudes above sea level showed that fog always appeared first and visibility was always minimum at higher levels. Afterwards, visibility gradually degraded progressively downward to lower levels. These observations indicate that the leading edge of the "fog front" sloped upward in the downwind (onshore) direction. Apparently, greater wind speeds at higher levels, unstable atmospheric conditions, and warm surface temperatures contributed to this chain of events.

When the stratus existed aloft prior to the formation of fog at the surface, the thermal structure in the lowest 30 m of the atmosphere prior to and during the advent of fog remained relatively unchanged. When clear skies existed before fog formation, the thermal structure changed in much the same way as observed in valley fogs. Surface temperatures were consistently warmer than temperatures aloft during periods of fog. Prior to sunrise, the unstable conditions combined with onshore upslope winds producing steady updrafts (at 32 m above the surface at the Tower site) averaging approximately 0.2 m sec^{-1} and occasionally gusting to over 0.5 m sec^{-1}. After sunrise, peak up- and downdrafts were in excess of 1.5 m sec^{-1}.

Similarly, fog microphysics exhibited features characteristic of aged stratus clouds occurring in maritime atmospheres. Low concentrations of extremely effective sea-salt nuclei gave rise to droplet populations consisting of a few relatively large droplets. The drop-size distribution was typified by a broad range of drop sizes with peak concentrations at 4 to 10 μm radius. The advection fog drop-size spectra were further distinguished by the presence of drizzle size (up to 100 μm radius) drops. The presence of a continuous light drizzle was observed throughout the life cycle of the advection fog and is indicative of an aged fog of considerable depth.

C. RADIATION FOG

1. Fog Formation Characteristics

A total of five radiation fogs were observed during the field trips to Vandenberg and Los Angeles: three at Vandenberg and two at Los Angeles. The radiation fogs at Vandenberg occurred on 19, 23, and 29 September and persisted for 7.5, 0.4, and 3.5 hours, respectively. At Los Angeles, radiation fogs formed on 5 and 9 November. The fog of 5 November was of 3.5 hours duration, and the fog of 9 November persisted for nearly 14 hours.

The Vandenberg radiation fogs of 23 and 29 September are not discussed in this section. The fog of 23 September was a shallow ground fog which persisted at the Hilltop site for ~1.5 hr. A wind shift advected a small patch of fog over the Tower site just prior to dissipation at ~0400. Only a minimum of data was obtained during the brief (10-20 min) encounter with this fog.

The fog of 29 September formed and persisted only in a valley some distance from the Tower site; thus, micrometeorological data obtained at the Tower do not specifically apply to fog formation analyses. Fog microphysics data obtained in the fog of 29 September are discussed in a following section.

- Synoptic Situation

Because the radiation fogs observed at the two sites occurred at different times of the year, description of the synoptic situation necessarily falls into two parts. The basic flow pattern for the September period was described in Part B of this section. The detailed weather conditions during the radiation fog of 19 September were these: Aloft, the weak trough present on the 18th and 20th was temporarily replaced on the 19th by a migratory ridge. At the surface, this upper air ridge caused a pronounced weakening of the thermal low in central California and high pressure ridging westward from the plateau region of California. Consequently, the large-scale pressure pattern was favorable for the light easterly, offshore winds which precluded the occurrence of advection fog and provided conditions favorable for radiation fog formation.

In early November 1971, the Los Angeles area was under the influence of a variety of winter season weather patterns associated with the southern edge of westerly flow aloft. These weather patterns consisted of migratory troughs and ridges as well as an occasional cutoff low and poleward intrusion of the subtropical high. The fog of 5 November occurred during a period of transition from an intruding subtropical ridge to a cutoff low. During this transition, the surface pressure field evolved from a well-developed north-south pressure gradient associated with a strong surface high located under a ridge aloft to a weak pressure field found under a developing closed low aloft. This weak surface pressure field provided the large-scale environment for the formation of radiation fog at Los Angeles on 5 November 1971.

On the 9th, the Los Angeles area was under the influence of a migratory ridge aloft. As this ridge moved eastward, the surface pressure gradient weakened and the area was sandwiched between developing high pressure to the east and the subtropical high pressure cell off the coast. The resulting conditions were favorable for formation of the radiation fog of 9 November 1971.

- Visibility Characteristics

The visibility records for the radiation fogs on 19 September at Vandenberg and 5 and 9 November at Los Angeles are shown in Figures 16, 17, and 18, respectively. Again, visibility records from varying altitudes at the two field locations are organized in descending order in the figures. Unlike that of the previously discussed advection fogs, visibility in these three radiation fogs was at times quite uniform and very low. Visibility restrictions of <200 m for periods of several hours were common in all three fogs. The most dense fogs were observed in Los Angeles. During the fog of 9 November, for example, visibility (Figure 18) was restricted to <100 m for a large portion of the fog lifetime and often degraded to <50 m for substantial periods.

Fog density in each of these three radiation fogs exhibited little consistent correlation with surface elevation. Note from the figures that, typically, visibility was relatively uniform from site to site. However, at Los Angeles, fog density was somewhat less severe and fog (in the lowest 38 m) duration was shorter at the Tower site than the other LAX sites. This was probably due to the "heat island" effect of the extensive asphalt parking lots which surround the ASDE tower. The heat island effect was particularly evident from the visibility records for the fog of 9 November. While this fog appeared almost at the same time at each of the three sites, complete dissipation at mid-morning occurred only at the Tower site.

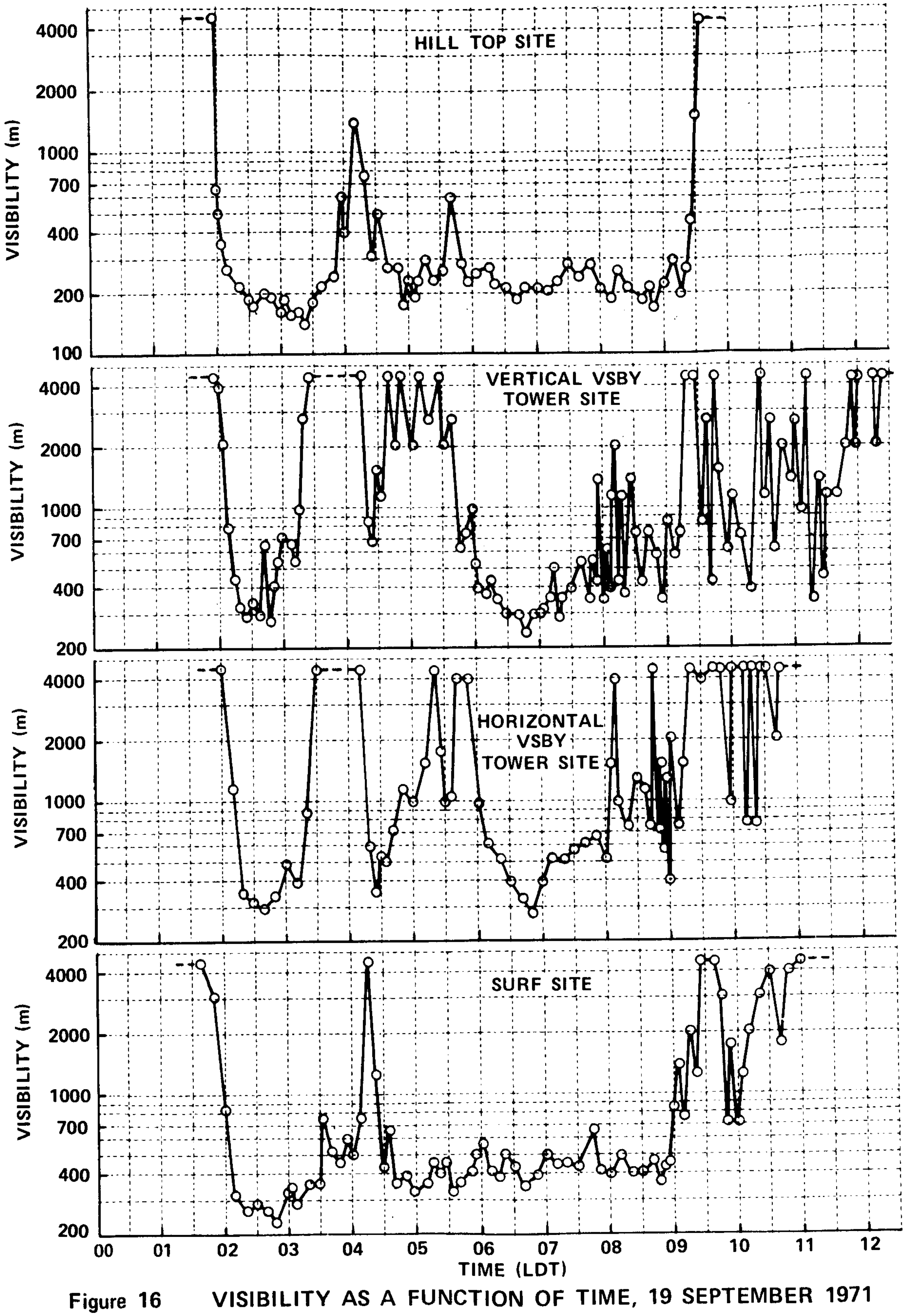

Figure 16 VISIBILITY AS A FUNCTION OF TIME, 19 SEPTEMBER 1971

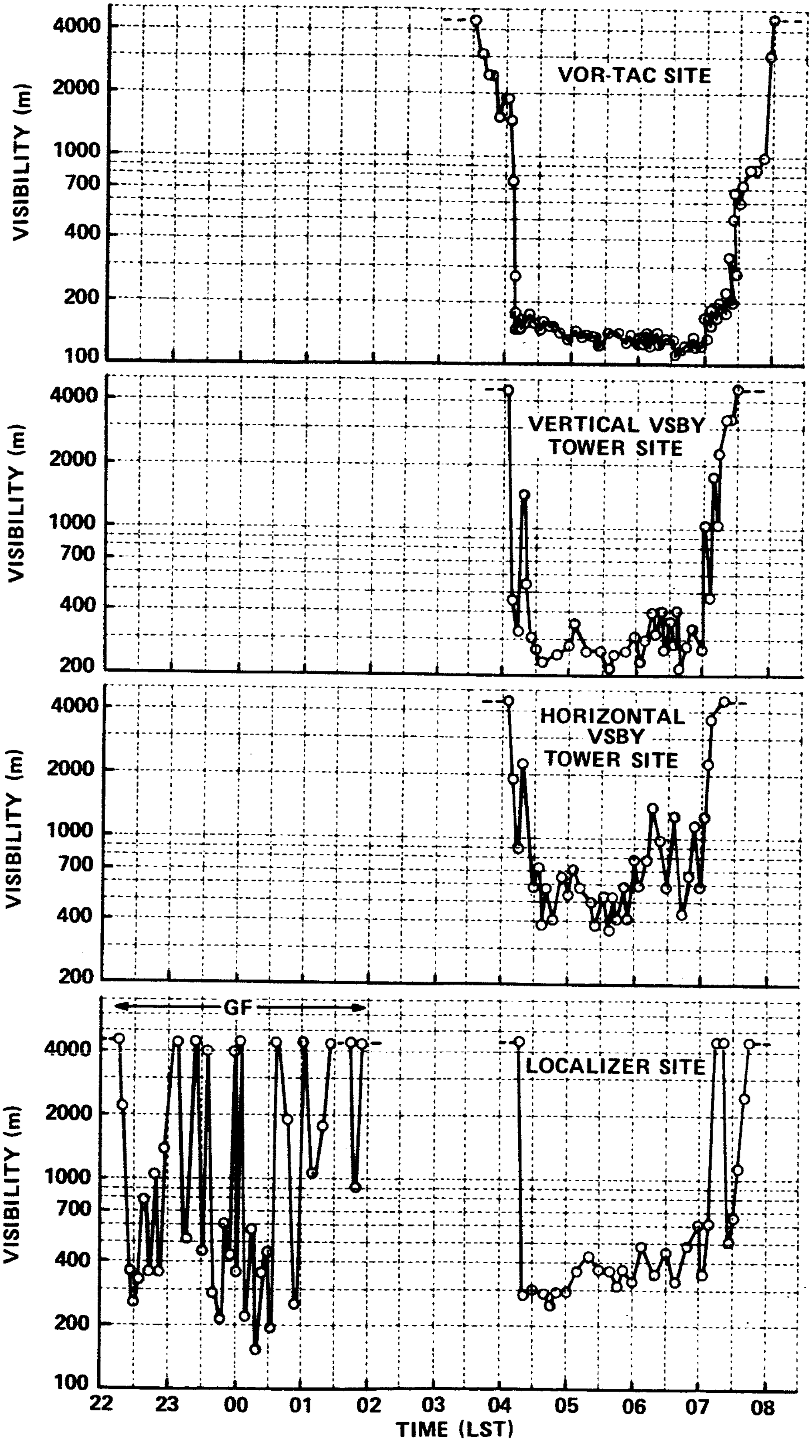

Figure 17 VISIBILITY AS A FUNCTION OF TIME, 5 NOVEMBER 1971

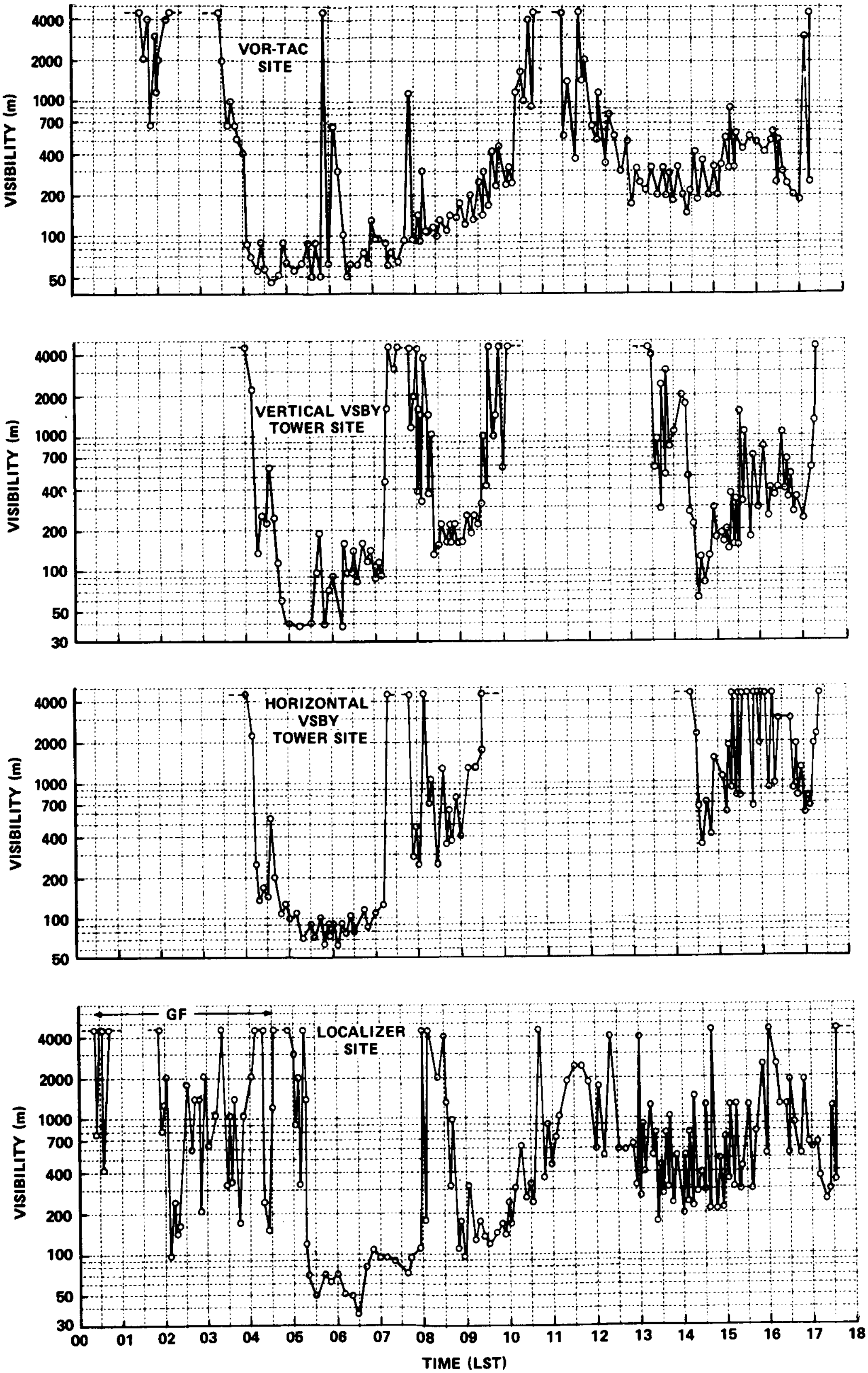

Figure 18 VISIBILITY AS A FUNCTION OF TIME, 9 NOVEMBER 1971

Further, dissipation was most pronounced at the surface. Visibility improved, but fog never completely dissipated at the VOR and Localizer sites.

The visibility records for the radiation fog of 19 September at Vandenberg show that fog was consistently most dense at the Hilltop and Surf sites. Surf site was located on the southwest side of a small valley (oriented northwest-southeast) and Hilltop site was situated on top of the southwest ridge. The data suggest that this fog was initially a widespread radiation fog which formed to a depth much greater than that of the valley. Later, changing conditions caused partial dissipation of fog at the Tower but trapped fog in the valley. Fog generation continued in the valley and predominantly easterly winds advected the fog over the Tower site.

2. Micrometeorological Data

- Low Level Winds

Wind speed and direction were monitored continuously throughout the pre- to post-fog periods for the three occurrences of radiation fog. The data obtained and analyzed at half-hour intervals are shown in Figures 19, 20, and 21 for the fogs of 19 September and 5 and 9 November, respectively. As can be seen from the figures, winds were typically light (1 to 3 m $\sec^{-1}$) and easterly during each of the radiation fogs at both Los Angeles and Vandenberg.

While the radiation fogs did not form at the primary data acquisition sites but rather were advected to these locations by prevailing winds, a comparison of wind data in Figures 19, 20 and 21 with visibility data in Figures 16, 17 and 18 reveals little correlation between wind and the occurrence of fog. For at least two hours prior to the onset of each of these fogs, wind direction did not vary by more than ±20° from the direction prevalent after fog formation. Similarly, although winds were shifting during the dissipation of the 19 September fog, the tower site remained downwind of the valley where fog was forming. Fog dissipation on 19 September was probably not related to the shifting wind. A change in wind direction between 0300 and 0500, however, appeared partially responsible for improvements in visibility which occurred at all sites during that period.

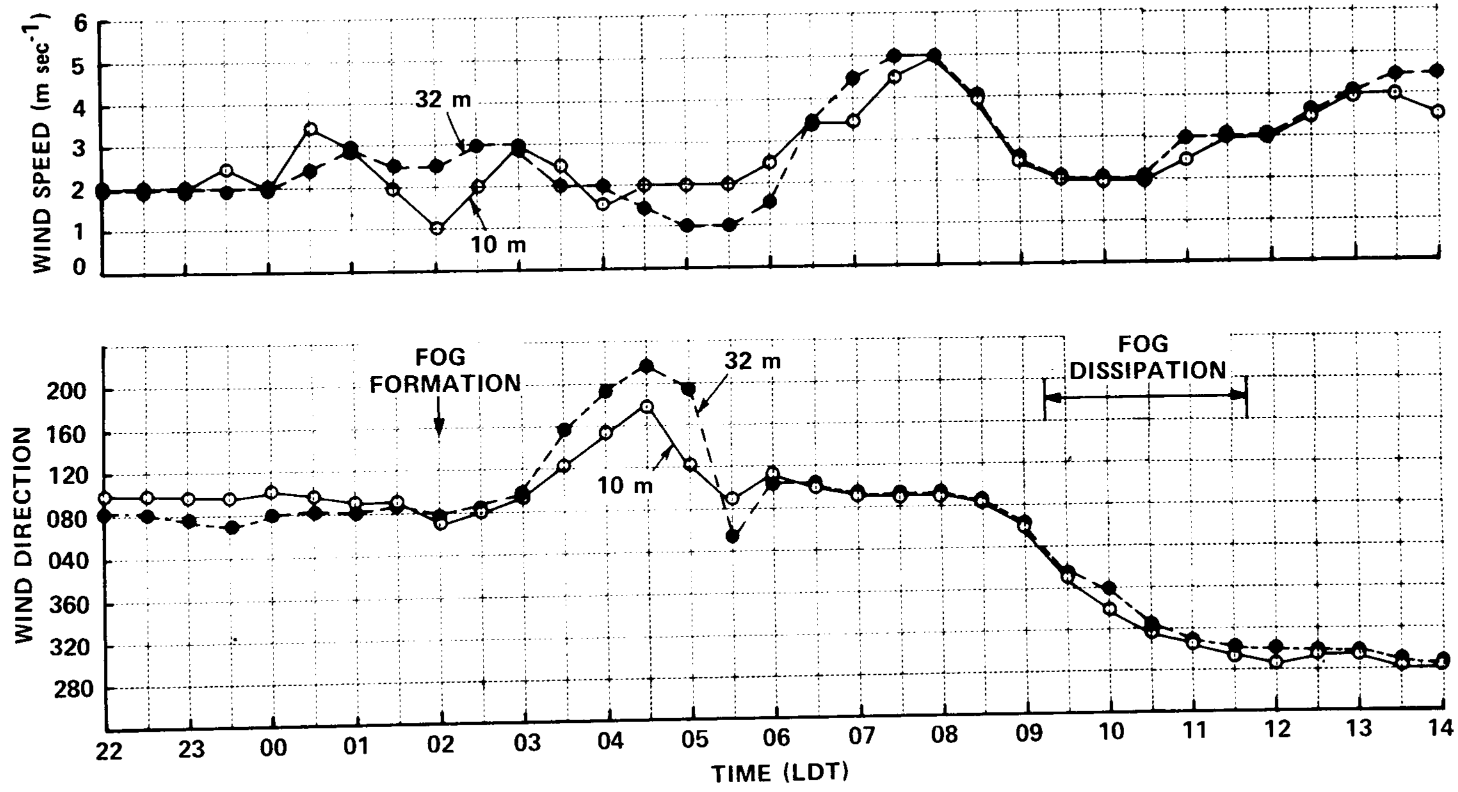

Figure 19 WIND SPEED AND DIRECTION AS FUNCTIONS OF TIME, 19 SEPTEMBER 1971

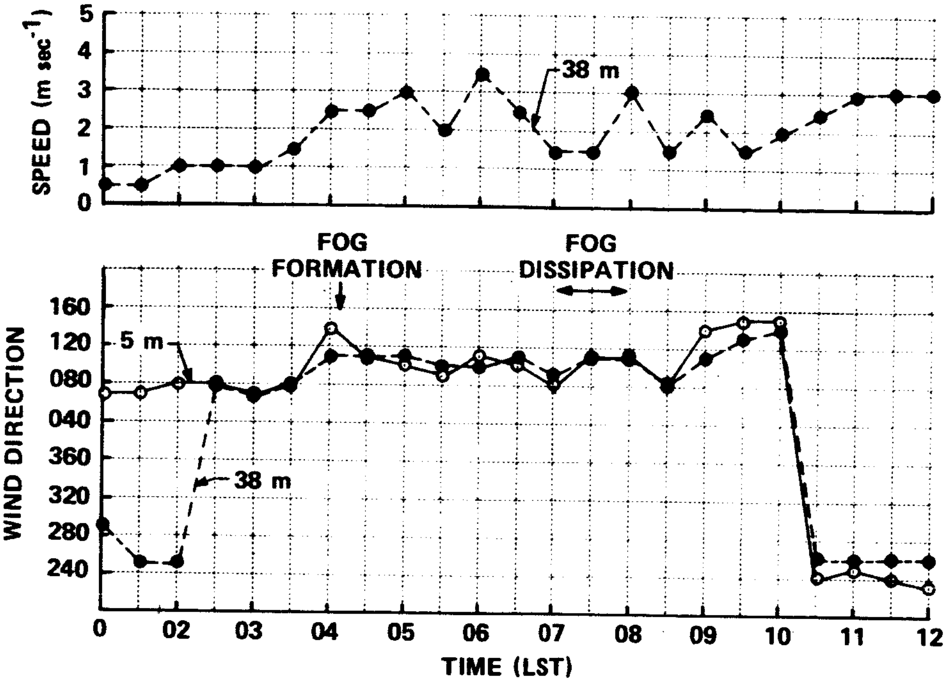

Figure 20 WIND SPEED AND DIRECTION AS FUNCTIONS OF TIME, 5 NOVEMBER 1971

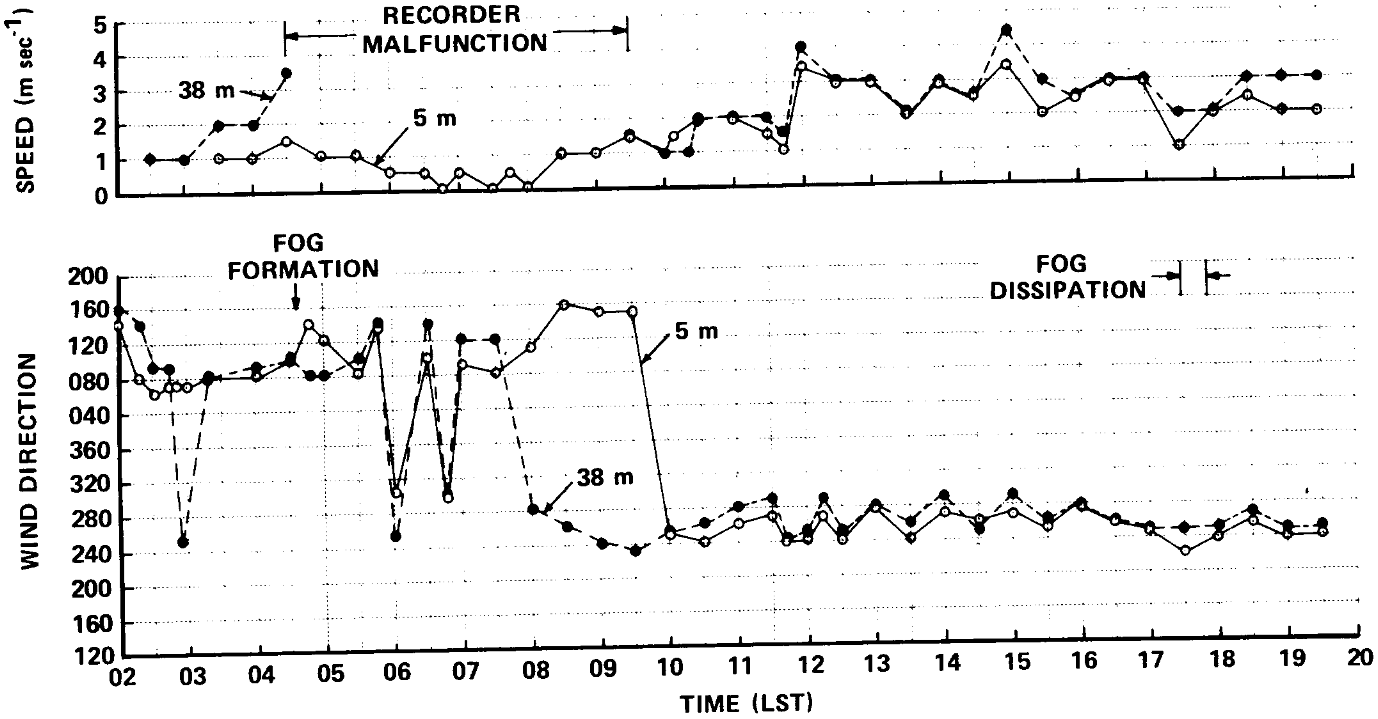

Figure 21 WIND SPEED AND DIRECTION AS FUNCTIONS OF TIME, 9 NOVEMBER 1971

- Low Level Temperature and Dew Point Data

The low level temperature and dew point profiles for the three radiation fogs exhibited features similar to patterns observed by Pilié et al. (1972) in the study of radiation-valley fog at Elmira. Temperature and dew point data for the fogs of 19 September, 5 and 9 November are presented in Figures 22, 23, and 24, respectively. As shown by the data, prior to each of the radiation fogs, a low level inversion formed by 0000 and persisted with minor fluctuations in intensity until fog formed. In general, the inversion was most intense at the lowest levels.

Cooling occurred at all levels (up to approximately 30 m) throughout the early morning hours prior to fog formation. Typically, at approximately one-half hour before the onset of fog, temperatures in the lowest levels began to increase slowly while temperatures at higher levels (10 m and above) continued to decrease. While the magnitude of the temperature changes and the heights at which they occurred varied from fog to fog, the trend was consistent and indicated the formation of a fog layer aloft. The fog layer prevented further surface cooling, but radiational heat loss from the top of the layer allowed additional cooling at that level. Subsequent instability caused mixing and cooling of lower levels.

After fog formation, temperatures remained constant or began to increase slowly. At sunrise, surface temperature followed by those at higher levels began to increase rapidly, ultimately causing fog dissipation at about mid-morning.

Radiational cooling caused substantial dew deposition prior to the formation of each of the radiation fogs. Total dew deposition was well in excess of 300 g m^{-2} by the time of fog formation. Dew deposition behavior was similar to that observed in Elmira. That is, dew deposition stopped at the time of fog formation; total dew weight remained constant until about sunrise, and then evaporation of dew commenced.

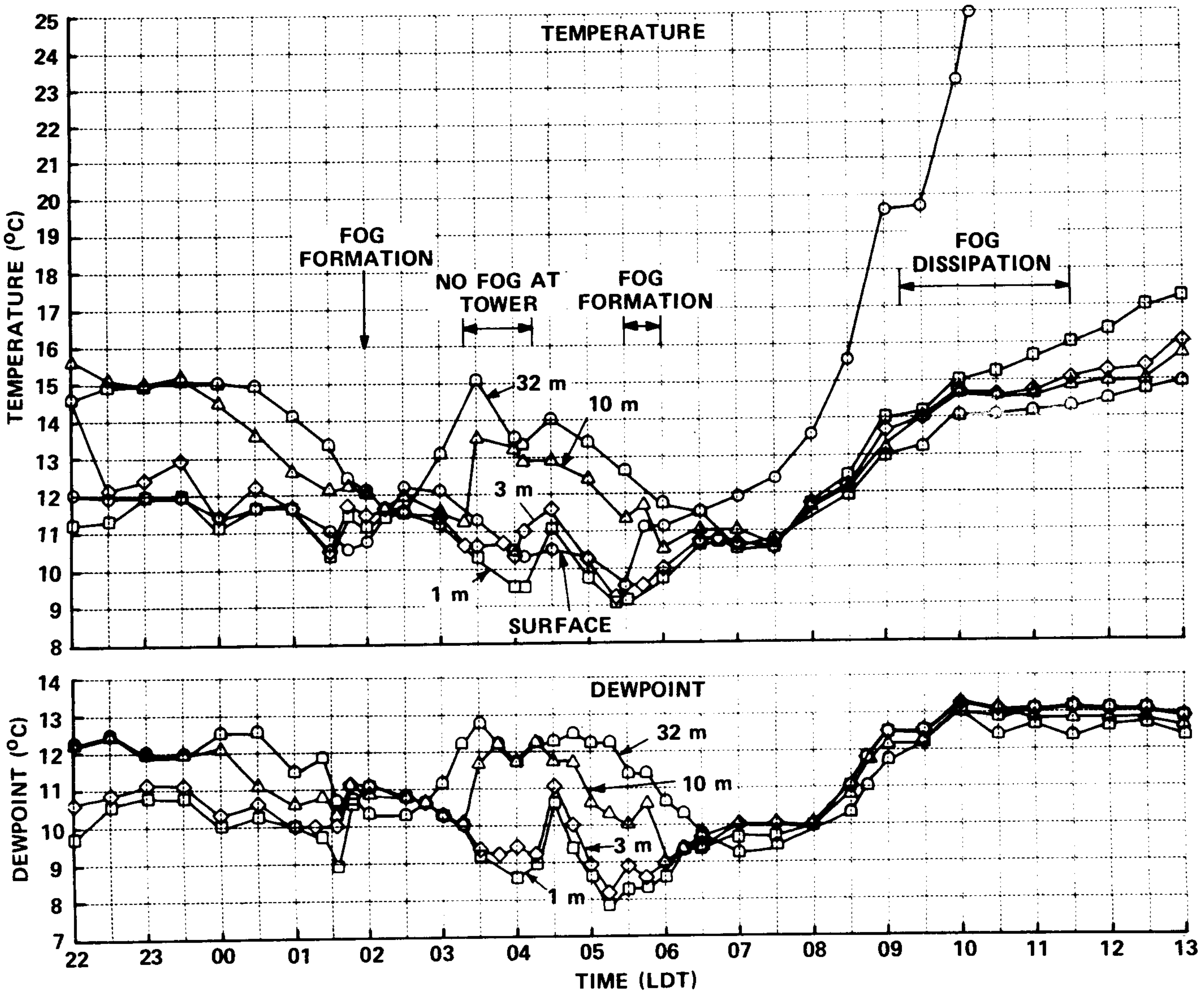

Figure 22 TEMPERATURE AND DEWPOINT AS FUNCTIONS OF TIME, 19 SEPTEMBER 1971

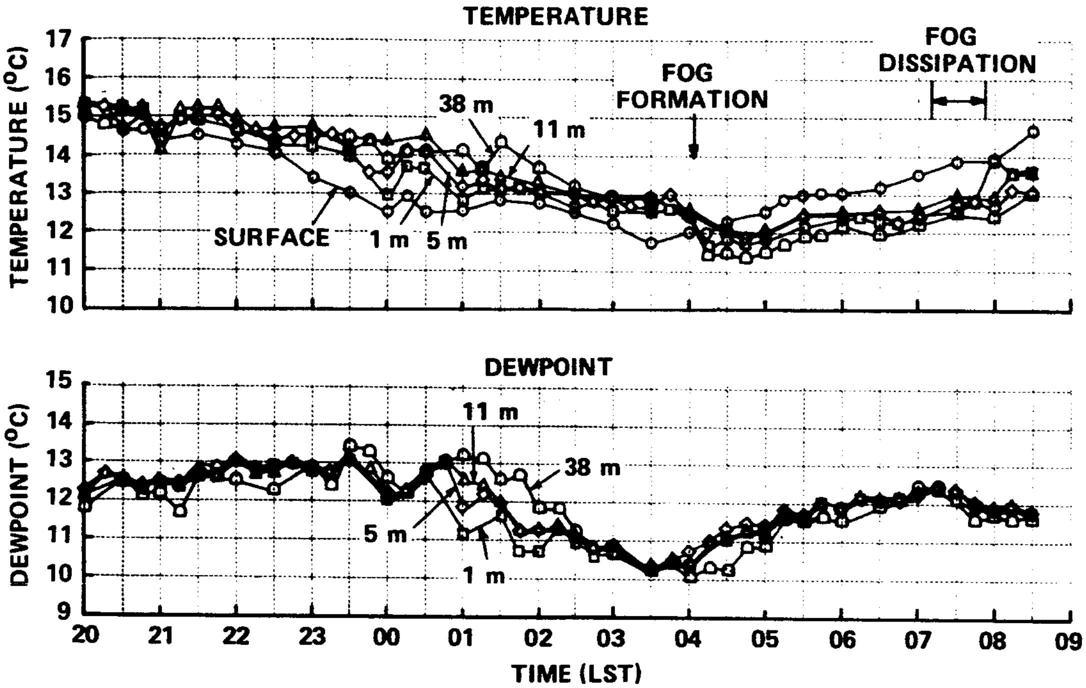

Figure 23 TEMPERATURE AND DEWPOINT AS FUNCTIONS OF TIME, 5 NOVEMBER 1971

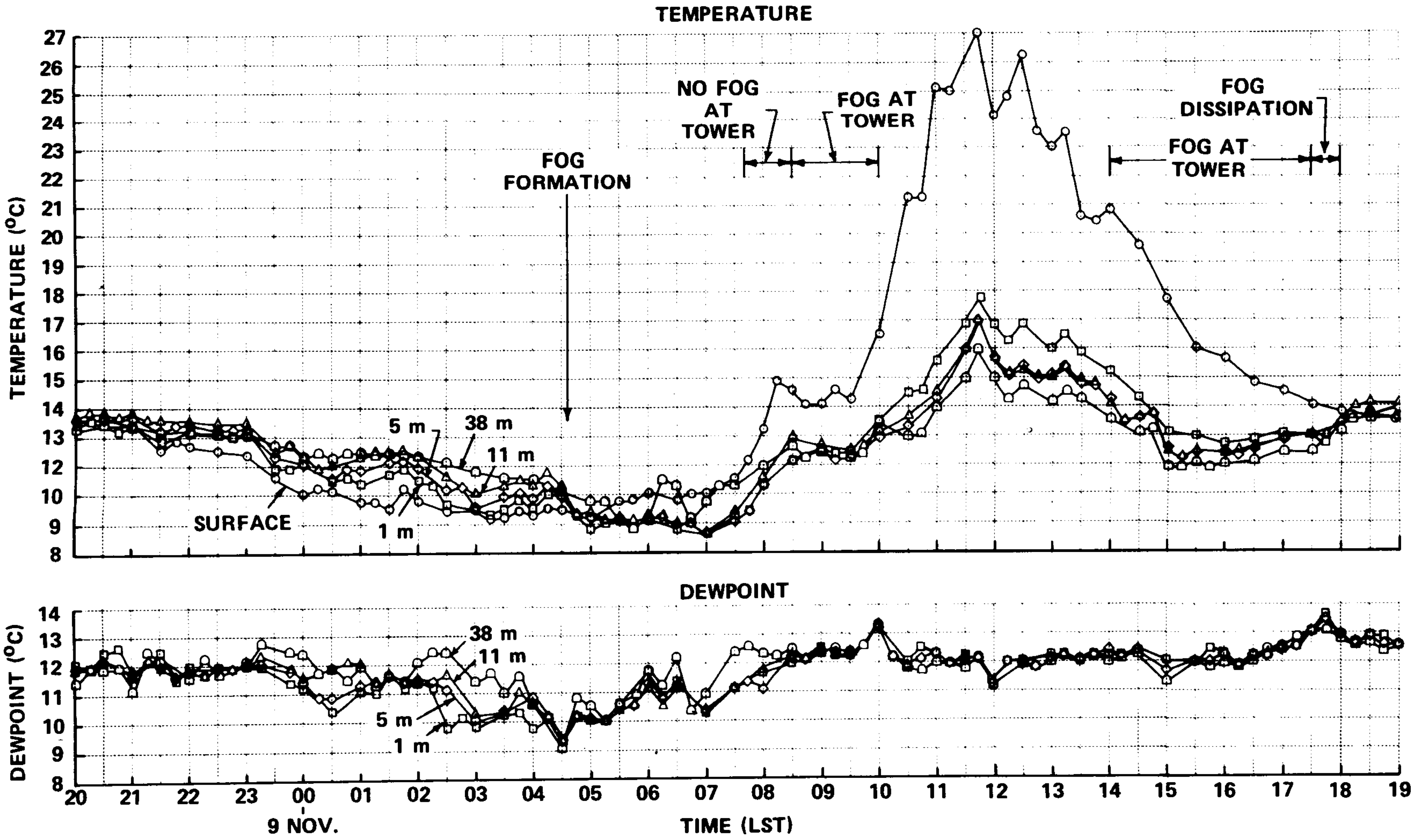

Figure 24 TEMPERATURE AND DEWPOINT AS FUNCTIONS OF TIME, 9 NOVEMBER 1971

Each of these fogs occurred under complicated micrometeorological situations, and the temperature profiles exhibited a number of departures from the general trends discussed previously. Note, for example, from Figure 16 that while the fog of 19 September was uniformly persistent at two widely spaced sites (Hilltop and Surf), fog at the Tower site (midway both vertically and horizontally between the other two sites) appeared in three distinct patches. The temperature and dew point records obtained at the Tower site also reflect those events. As shown in Figure 22, during the period of patchy fog (0330 to 0530), cooling continued in the lowest 3 m where fog was most persistent (Figure 16). At 10 m and above, however, substantial warming occurred at about the same time winds began shifting. Winds ultimately shifted nearly 100° from east to south-southwest and then back to east during the patchy fog period. It seems likely that a lowering of a higher level inversion caused the observed warming and wind shift and was responsible for the dissipation of fog at the Tower during that period. At the same time, fog was trapped in the valley. As the inversion lifted and winds shifted back to east, foggy conditions were again advected over the Tower site.

The Surf site which is located at the mouth of the Santa Ynez Valley and the Hilltop site which is located on top of the southwest ridge of the valley were almost continuously in dense fog. Visibility data obtained at the Vandenberg air field (9 km to the north) showed that equally dense fog formed there at nearly the same time as at the other sites. The trend of events which occurred on 19 September suggests that fog formation was initially widespread. Later, when the inversion lowered, fog was being formed only in the Santa Ynez Valley (northeast of the Tower) and advected over the Hilltop site toward the Tower site.

Meteorological conditions were somewhat less complicated during the Los Angeles radiation fogs. Visual observation positively confirmed that the Los Angeles radiation fog of 5 November advected from an east-southeast direction over the Tower. The visibility records support that observation. Note from Figure 17 that fog was first observed aloft at the VOR site, next at the Tower site, and finally at the Localizer site (farthest downwind). From Figures 17, 20, and 23, representing visibility, wind and temperature, it can be seen that while radiational cooling was occurring at all levels below 38 m, steady winds advected fog and somewhat cooler air over the site. Once radiational cooling was substantially reduced by the fog cover, heat conduction from the ground to the air apparently caused air temperatures within the fog to increase. Further heating after sunrise led to eventual fog dissipation.

The fog of 9 November at Los Angeles must also have formed and advected over the Tower site in a manner similar to that of 5 November. Note from Figures 18, 21, and 24 that with light but steady easterly winds, fog appeared aloft at the VOR site, next at the Tower site, and finally at the Localizer site (the farthest downwind site). As the fog gradually advected into and thickened over the region, air temperature continued to decrease at higher levels. Upper level cooling continued until the time of the first visibility minimum. Lower level (i.e., $\leq$ 10 m) temperatures remained constant for about an hour after fog formation and then decreased slightly from 0600 to 0700 LST.

Warming at all levels commenced at approximately 0700 and partial fog dissipation followed soon afterward at the centrally located Tower site. An increase in wind speed and a shift in direction to westerly beginning at about 0800 brought in cooler moist air off the ocean and allowed fog to persist at the Tower until 1000. Warming by the sun was apparently responsible for dissipation of the second patch of fog at the Tower site.

As indicated by the visibility records for the VOR and Localizer sites in Figure 18, complete fog dissipation occurred only at the center of the airport, probably due to heating of the surrounding asphalt. Air temperature at the Tower increased by as much as $4^{o}C$ during the afternoon. Continued advection of cooler air by westerly winds, however, overcame surface heating by about noon and air temperature began to decrease. By about 1500, air temperature and dew point converged and fog lowered to the surface at the Tower site. Warming at low levels commencing at about 1730 apparently caused final fog dissipation by 1800.

3. Microphysical Characteristics of Radiation Fog

● Drop-size Distributions

Drop-size distributions acquired in the radiation fogs of 19 September, 5 November and 9 November are presented in Figures 25, 26, and 27, respectively. Compared to the drop-size distributions obtained in Vandenberg advection fogs (shown in Figures 12, 13, and 14), drop spectra observed in the radiation fogs are quite narrow. While the greatest percentage of droplets were observed within the same size range (i.e., 4-10 μm) for both fog types, the very large drizzle drops were not present in the radiation fog.

The size distributions of fully activated fog droplets found in radiation fogs at Vandenberg and Los Angeles were quite similar. However, measurements in Los Angeles made with the haze chamber revealed the presence of significant concentrations of enlarged nuclei (solution droplets that are not fully activated under ambient conditions). These nuclei which exist in concentrations of approximately 1250 cm^{-3} in Los Angeles fogs enlarge to radii $\geq$ 1 μm (at 100% relative humidity), which is the minimum detectable size in the chamber. In the supersaturated ambient atmosphere, the solution droplets must be even larger. Since the droplets were not detected in natural fog, however, their maximum radius must have been smaller than the 2 μm cutoff of the gelatin sampler.

The complete drop-size distribution at Los Angeles must have consisted of the distributions illustrated in Figures 26 and 27 plus a spike extending to over 1000 cm^{-3} in the 1 to 2 μm radius increment. This spike is important for several reasons. First, droplets in this size class contributed significantly to the visibility restriction experienced on 5 and 9 November. Depending on their actual size distribution, the visibility restriction due to the solution droplets alone (i.e., without the fully activated fog droplets) was computed to be between 500 and 130 m.

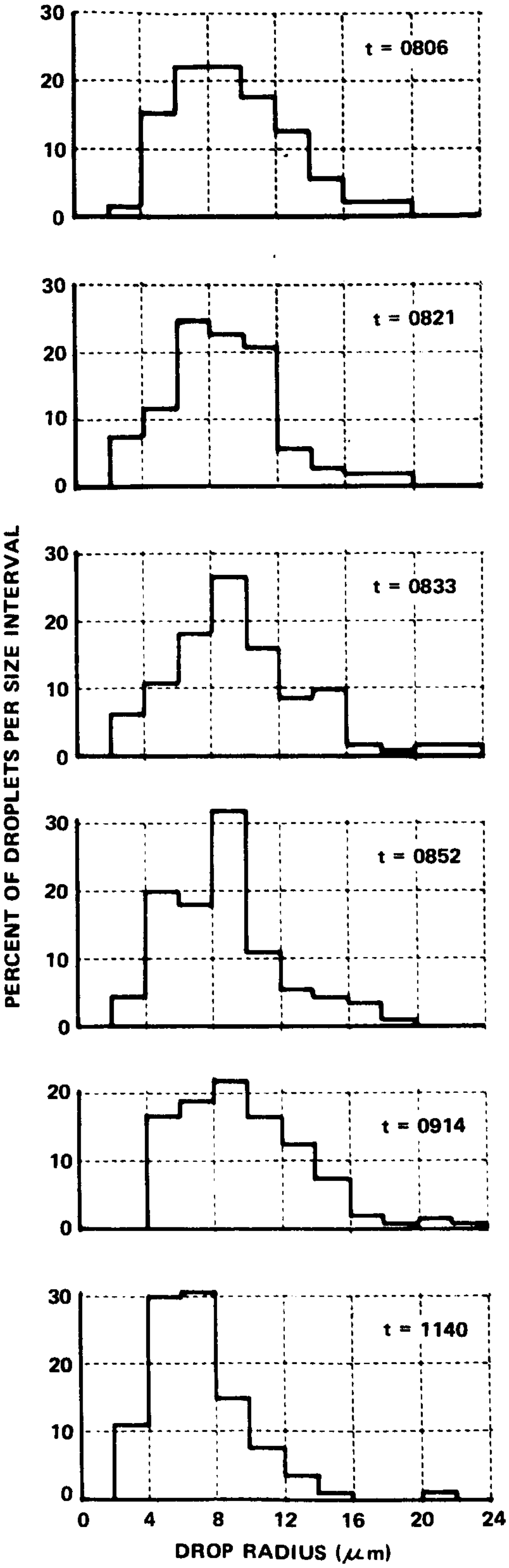

Figure 25 DROP SIZE DISTRIBUTIONS OBTAINED IN RADIATION FOG, 19 SEPTEMBER 1971

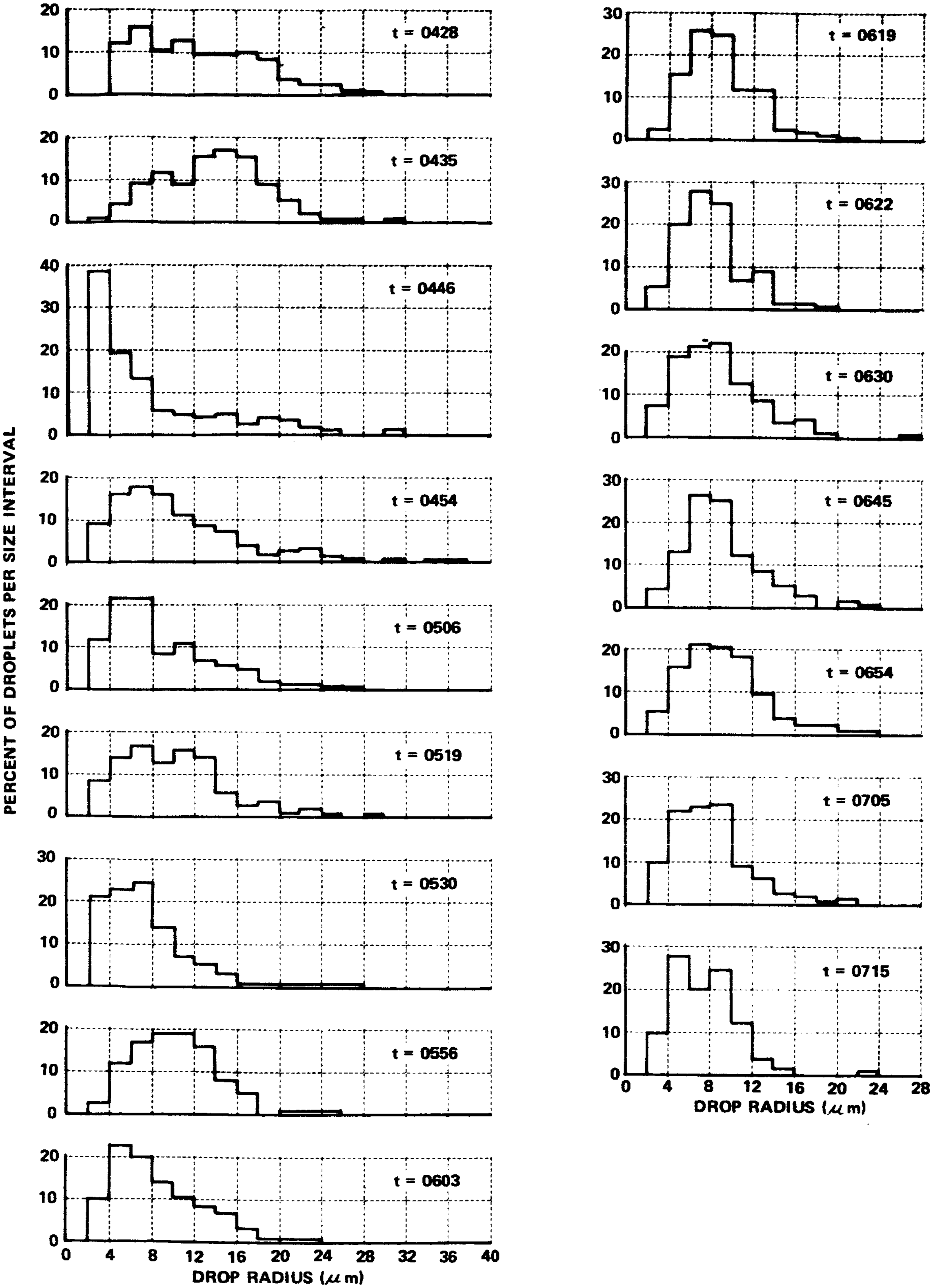

Figure 26 DROP SIZE DISTRIBUTIONS OBTAINED IN RADIATION FOG, 5 NOVEMBER 1971

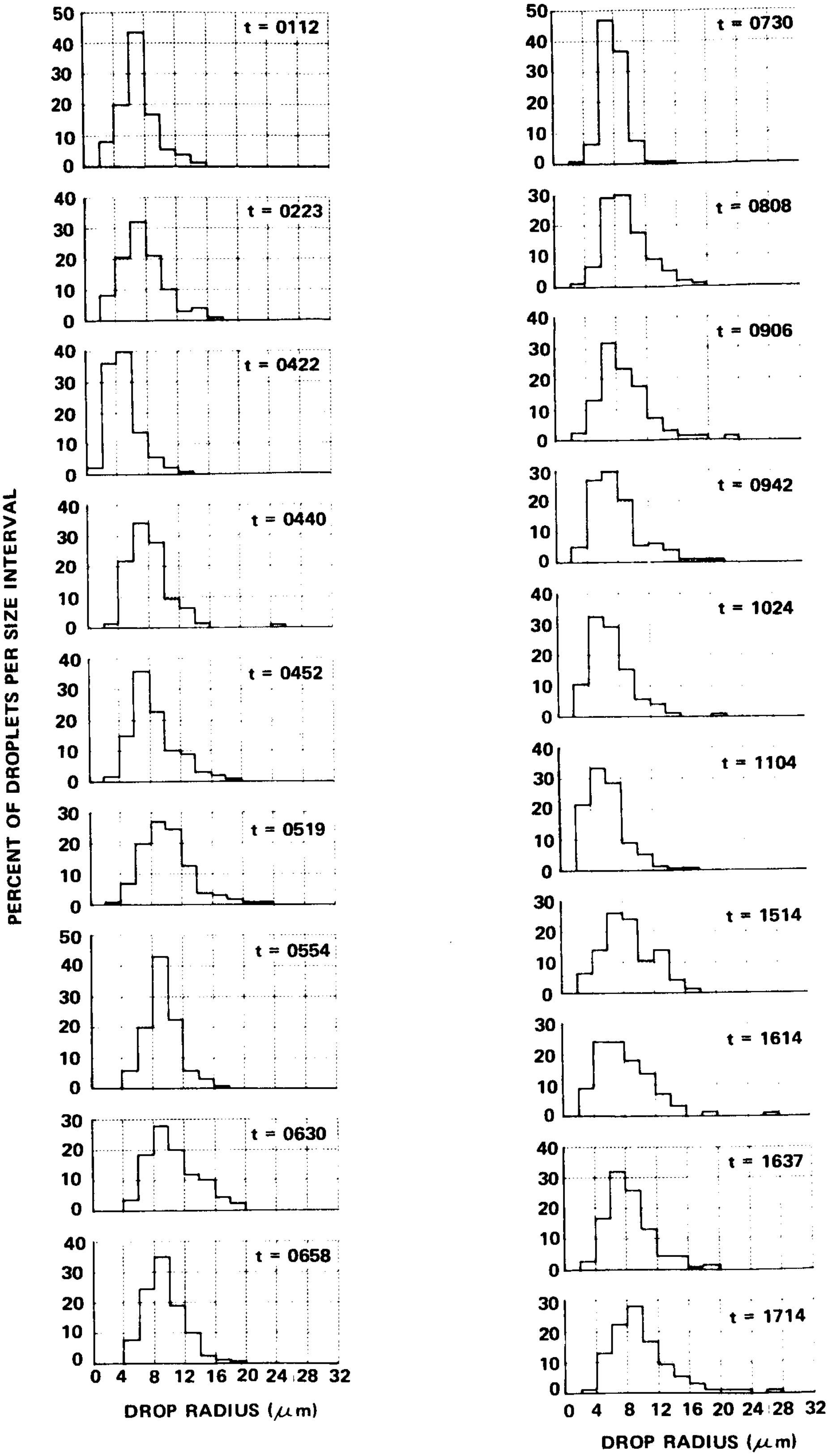

Figure 27 DROP SIZE DISTRIBUTIONS OBTAINED IN RADIATION FOG, 9 NOVEMBER 1971

Second, the presence of high concentrations of solution droplets carries important implications when considering fog modification programs in polluted regions such as the Los Angeles Basin. Most realistic modification efforts are directed at either altering drop sizes or lowering relative humidities to slightly less than 100% (i.e., 95-99%), thereby causing evaporation of fog. If visibilities are already restricted to 130-500 m by the high concentrations of hygroscopic particulates that exist at relative humidities < 100%, then modification efforts might be fruitless.

The detection of the solution droplets with the haze chamber was particularly important to the data analysis on this program. In an earlier discussion, we explained how the large drizzle droplets observed in Vandenberg affected the LWC estimate based on drop-size distribution and transmissometer data. Referring back to Figure 15, it is immediately apparent that similar estimates made with Los Angeles data indicate liquid water contents that are roughly twice the values measured directly with the Gelman high volume sampler. The explanation of this discrepancy rests in the fact that the solution droplets caused a significant visibility reduction, and consequently were detected by the transmissometer but were not detected by the droplet sampler. While the LWC in these extremely small droplets was negligible, the calculation ascribed the visibility reduction caused by them to larger droplets. Hence, the concentration of larger droplets, and therefore the total liquid water content, was overestimated.

This discussion again illustrates the importance of measuring haze nucleus concentrations in fog studies, particularly in polluted areas. A review of the data acquired in the relatively clean environments of Vandenberg and Elmira shows that in both cases the contribution of haze to visibility restriction was negligible.

- Liquid Water Content

Manual observations of LWC were obtained at infrequent intervals since we normally compute LWC from drop-size distributions and visibility data. As previously discussed, computations of LWC were not as reliable as in previous studies because of the large number of small drops that were not sampled but which contributed to reduced visibility. The few measurements that were obtained revealed LWC of 100-150 mg m^{-3}, 100-200 mg m^{-3}, and 150-300 mg m^{-3} in the radiation fogs of 19 September, 5 and 9 November. The data points suggest trends similar to those observed in the Elmira valley fog. For example, LWC increased to a maximum during the first 0.5-1.0 hour after fog formation. By the time of the first visibility minimum, LWC had decreased somewhat and leveled off to a more or less constant value. Near the end of the fog life cycle, LWC began to decrease rapidly until final fog dissipation. In view of the large number of haze size droplets occurring in Los Angeles fogs (and probably in most fogs occurring in polluted environments), it is recommended that in future life cycle studies greater reliance be placed on the manual observations of LWC.

- Nucleus Concentrations

Only a few measurements of haze nucleus concentration were made during the fog of 19 September and no observations were obtained (due to instrument malfunction) in the fog of 5 November. Aitken and cloud nucleus (at 0.3%S) concentrations measured at Vandenberg in the fog of 19 September were 2500 cm^{-3} and 280 cm^{-3}, respectively. These values are among the lowest that we have observed in any natural atmosphere.

During the fog of 9 November at Los Angeles, extensive observations of nucleus concentration were obtained. Nearly continuous measurements of Aitken nucleus and haze (at 95% RH) nucleus concentrations were made throughout the pre- to post-fog interval as well as occasional observations of nucleus concentrations at intermediate values. These observations were made at the VOR site; the data are presented in Figure 28. From the figure, it can be seen that Aitken nucleus concentrations ranged from 10^4 to 3×10^4 cm^{-3}; cloud nucleus concentrations at 1.0 and 0.3%S averaged 3×10^3 and 1.6×10^3 cm^{-3}, respectively; and haze nucleus concentrations at 100% and 95% RH averaged 1.2×10^3 and 0.4×10^3 cm^{-3}, respectively.

It is evident from the figure that fluctuations in nucleus concentrations were not random. A comparison of data in Figure 28 with the visibility record shown in Figure 18 reveals an interesting correlation of

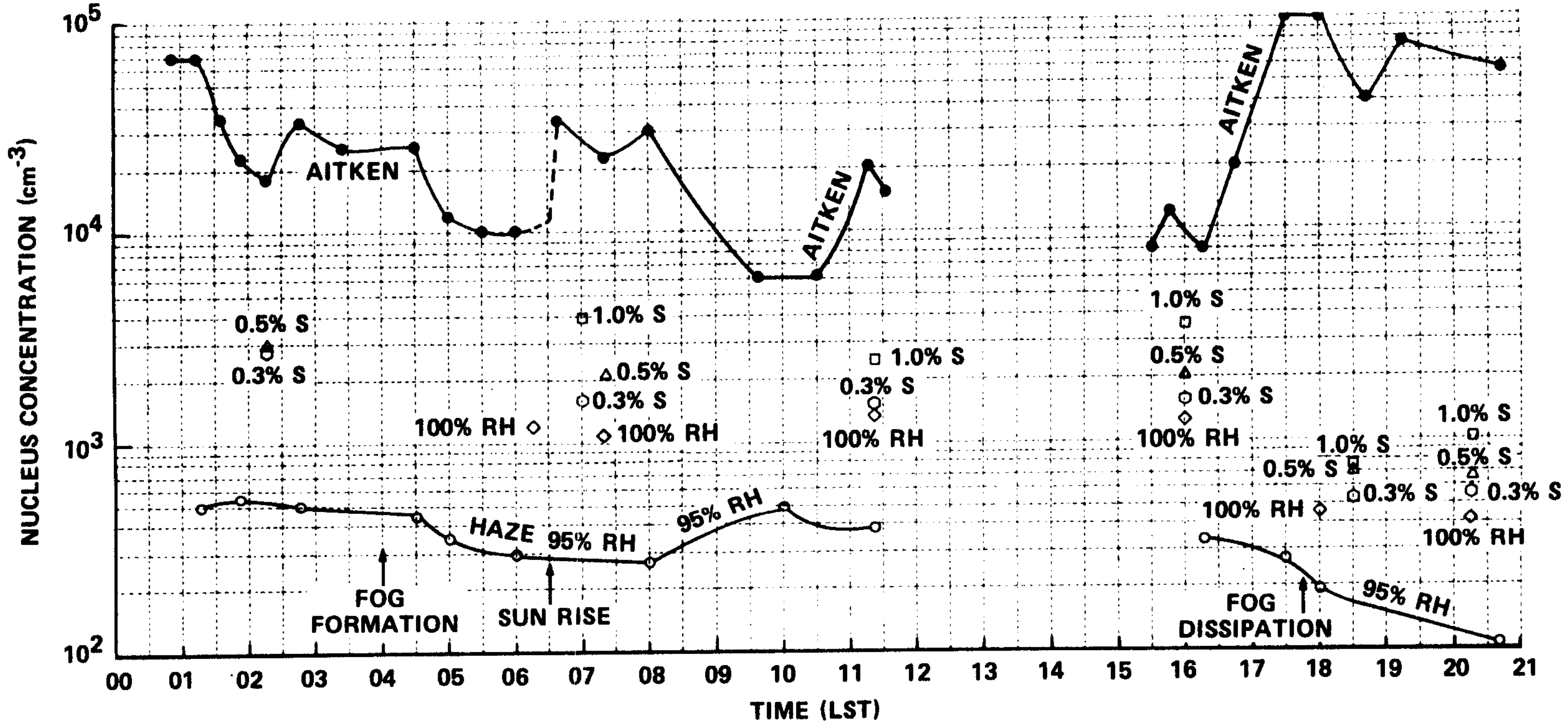

Figure 28 NUCLEUS CONCENTRATIONS AS FUNCTIONS OF TIME, 9 NOVEMBER 1971

nucleus concentration with the occurrence of fog on 9 November. Note that measurements made shortly after fog formation at 0430 show that both Aitken and haze nucleus concentrations decreased by approximately 50%. The loss of these particulates was most likely due to scavenging by fog droplets. The magnitude of this loss due to scavenging was in good agreement with that observed in recent laboratory experiments (Mack and Katz, 1971; Kocmond et al., 1972) performed at CAL.

Data were not obtained as frequently later in the day, and correlations are therefore not as easily recognized. The dramatic increase in Aitken nucleus concentration shortly after 0630, however, was probably due to increased vehicular traffic and photochemical production of aerosol after sunrise at 0630. Changes in aerosol concentration after 0800 are largely responses to local conditions and cannot be isolated. The very high Aitken concentrations after 1600 are probably the result of evening rush hour traffic. A large increase in the haze nucleus concentration would not necessarily be expected since most particulates formed by combustion processes are in the Aitken size range (i.e., ~0.1 μm).

4. Discussion and Summary

We have stated that the radiation fogs observed during this investigation at Los Angeles and Vandenberg did not form at the measurement sites. Rather, these fogs formed elsewhere at inland locations and were advected to the instrumented sites by light but steady easterly winds. These fogs formed under clear skies which allowed substantial radiational cooling and dew formation at the surface. Constant fluctuations in vertical motion provided sufficient mixing to cool the air in at least the lowest 30 m. As the fogs were advected over the instrumented sites, radiational cooling was reduced and air temperatures began to rise probably as a result of heat conduction from the ground. After sunrise, increased surface warming was ultimately responsible for final fog dissipation.

Microphysical characteristics of radiation fog were found to be quite different from those observed in advection fog. Drop-size distributions measured in radiation fog were narrow and sharply peaked. Drizzle sized drops were not observed in the radiation fogs.

Significant differences were also found between the complete drop-size spectra observed in radiation fogs formed at Vandenberg and Los Angeles. High concentrations of hygroscopic nuclei that enlarged to 1 to 2 μm radius solution droplets at relative humidities near 100% were measured at Los Angeles. These high concentrations of solution droplets were responsible for a significant portion of the observed visibility restriction in the Los Angeles fogs.

D. RADIATION-VALLEY FOG

On one occasion during the Vandenberg field trip, a fog formed only in the Santa Ynez River Valley which separates North and South Vandenberg. The valley is approximately 3 km wide and 100 m deep. The coastal valley fog, which formed on 29 September 1971 prior to 0530 and persisted until after 0830, filled the valley and spilled over the southwest ridge. Visibility was typically 300 m and LWC averaged 110 mg m^{-3}.

The radiation-valley fog formed under conditions similar to those observed in previous investigations near Elmira, NY. Clear skies allowed substantial radiational cooling and subsequent heavy dew deposition. Winds observed at the Tower site were light and easterly and caused some advection of the fog over the Hilltop site located on the southwest ridge of the valley. Dense fog was also observed at the Surf site which was located at the mouth of the valley near the coastline.

Nucleus concentrations were measured at the Tower prior to fog formation. These measurements revealed extremely low (but typical of the region) nucleus concentrations. Aitken nuclei averaged 3000 cm^{-3}; cloud nuclei at 1.0 and 0.3%S were 770 cm^{-3} and 250 cm^{-3}, respectively; and haze nucleus concentrations were 30 and 20 cm^{-3} at 100 and 96% relative humidity. (Typical nucleus concentrations observed in Elmira fogs were greater by approximately a factor of four.)

Average drop-size distributions obtained near Elmira, NY are compared in Figure 29 with those obtained in the Vandenberg valley fog. Data from the Vandenberg fog shown in the figure were acquired by sampling the fog at various levels along an access road that leads from the valley floor to the ridge top. The drop-size distributions were obtained

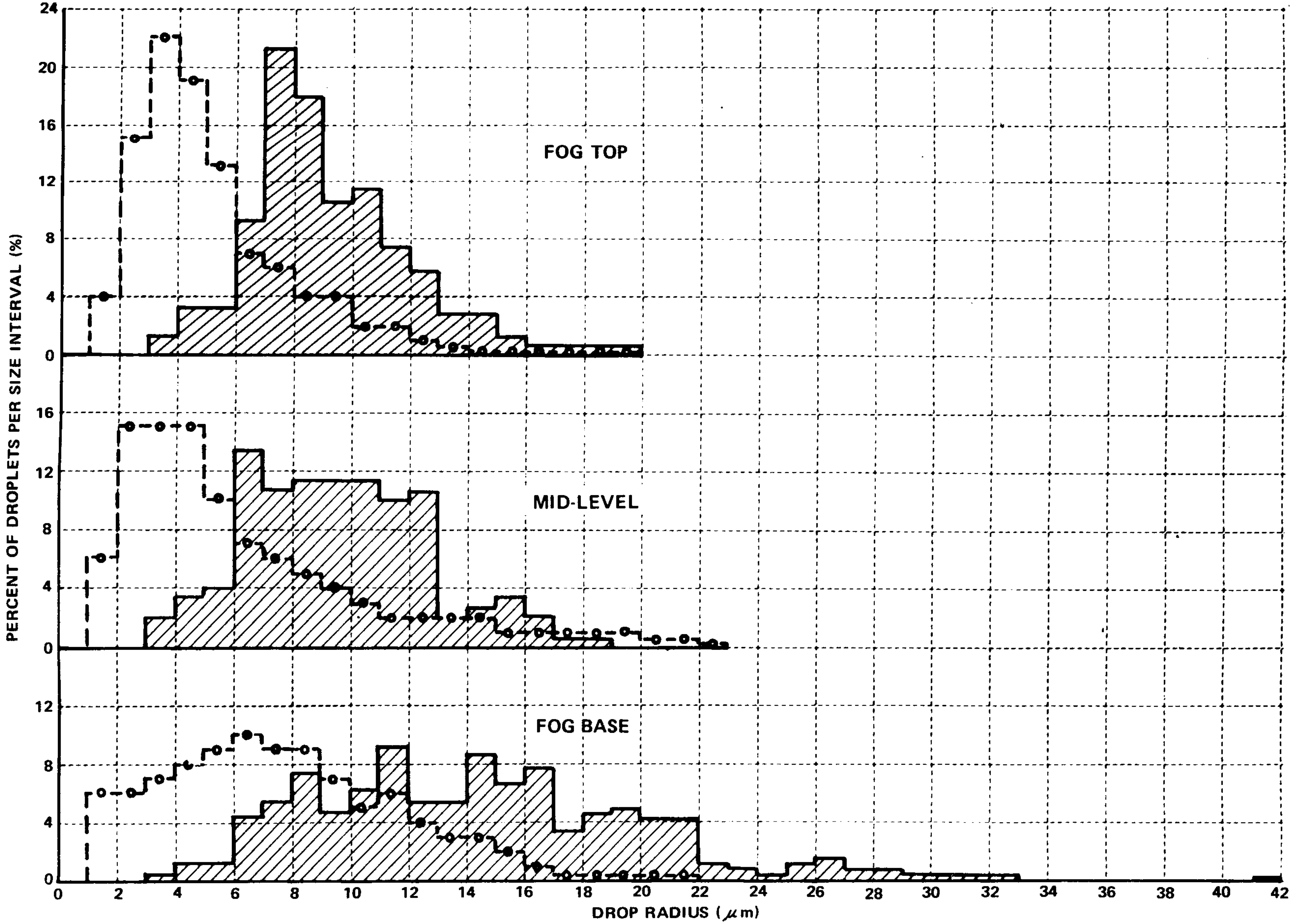

Figure 29 COMPARISON OF AVERAGE DROP-SIZE DISTRIBUTIONS AT THREE ALTITUDES IN ELMIRA, NY. VALLEY FOG (DASHED) WITH SIMILAR DATA OBTAINED IN A COASTAL VALLEY FOG (SHADED) AT VANDENBERG, CA.

at fog base, at the mid-level, and at fog top (100 m). Data shown for the Elmira fog were acquired by aircraft. The Elmira data represent the averages for seven valley fogs observed during the late summer of 1970. Note the striking similarities in the shapes of the drop-size distributions at each level for the two fogs and the remarkable difference in drop sizes.

Additional drop-size measurements obtained at other times and locations in the coastal valley fog exhibited similar differences from that of the inland valley fog. Apparently, differences in the population of cloud nuclei at these two sites were responsible for the observed differences in drop sizes.

E. DENSE HAZE

1. Formation Characteristics

During the field trips to Vandenberg and Los Angeles, data were also obtained during occurrences of what we have called "dense haze." These nighttime occurrences were typified by visibility restrictions of the order of 4 to 10 km and the presence of measurable concentrations of relatively large droplets. A total of three dense haze situations were observed: one at Vandenberg on 1 October and two at Los Angeles on 6 and 7 November 1971.

- Synoptic Situation

The weather pattern on 1 October was dominated by weak northerly flow aloft around a closed low situated over Utah. The attendant clear skies and weak pressure field at the surface allowed sufficient radiational cooling to cause convergence of temperature and dew point and droplet growth on sea-salt nuclei at high humidities. Visibility restriction was estimated at 4 to 6 km. Substantial drying at all levels which began at about 0430 caused a decrease in relative humidity to approximately 10% by 0700, thus preventing formation of radiation fog.

In the context of the synoptic discussion for the radiation fog cases of early November at Los Angeles, the weather pattern during the period 6-7 November was controlled by the aforementioned closed low. The extent of the influence of this system on the formation of haze rather than fog cannot be determined. It seems likely, however, that except during Santa Ana and other low humidity situations, haze is a common occurrence in the Los Angeles Basin. The formation of low level (i.e., ~100-300 m) cloud cover (observed on both nights) probably was responsible for limiting radiational heat loss and prevented cooling to the dew point temperature. Instead, relative humidity increased only to about 90%; this was sufficient, it appears, to cause deliquescence and growth of the most effective nuclei. Visibility restriction due to the presence of these enlarged haze particles was estimated at 5 to 10 km during both occurrences.

2. Micrometeorological Data

The haze of 1 October at Vandenberg was accompanied by moderate (4-6 m $\sec^{-1}$) northerly winds while the haze situations of 6 and 7 November at Los Angeles occurred with light (0.5-2.0 m $\sec^{-1}$) easterly and westerly winds, respectively. The haze of 1 October occurred under clear skies and subsequent radiational cooling. As a result, temperature in the lowest 10 m gradually decreased throughout the night. Aloft (30 m), however, temperature slowly increased during the period. Dew point temperature at all levels gradually decreased until about 0430. At that time, dew point began to decrease rapidly, ultimately reaching approximately 2°C (RH $\simeq$ 10%).

Radiational cooling was responsible for substantial dew deposition on the morning of 1 October. Dew deposition rates were observed to be about twice that measured in Elmira. These rates averaged approximately 40 g m^{-2} hr^{-1} until 0600. At 0600, total dew deposition had reached 350 g m^{-2}; but the dramatic decrease in relative humidity after that time caused rapid evaporation of dew.

The dense haze occurrences observed at Los Angeles formed under entirely different micrometeorological conditions. Easterly winds of 0.5-1.5 m sec^{-1} and westerly winds of 1.0-2.0 m sec^{-1} were recorded during the haze conditions of 6 and 7 November, respectively. Low level temperature profiles for both occurrences exhibited features characteristic of that which would occur under dense cloud cover. Surface temperatures exceeded low level air temperatures throughout the night. The temperature structure at higher levels ranged from near isothermal to superadiabatic on both occasions. Minimum temperatures were observed on both nights at approximately 0430. The minimum temperatures, however, were only 1°C less than that observed earlier at 2000. Dew point records for the two haze occurrences followed similar trends.

Dew deposition was not extraordinary during the two haze episodes observed at Los Angeles. A total deposition of 140 g m^{-2} of dew was measured through approximately 0030 on 6 November. At approximately 0015 the thin haze layer aloft (base estimated at 100-300 m) thickened and obscured the moon. After this time, the previously deposited dew began to evaporate. Total evaporation was not complete until 0715. On 7 November, the dense haze aloft (possibly cloud) formed much earlier (at approximately 1800, 6 November) and prevented dew formation.

3. Microphysical Characteristics of Dense Haze

Attempts were made with the gelatin sampler to obtain size distributions of those particulates which were responsible for the visibility restrictions observed during the three occurrences of dense haze. Exposure times of 5 to 15 sec* were required to obtain statistically adequate collections of those particles (droplets).

The droplet replicas (gelatin) obtained in the dense haze situations at both Los Angeles and Vandenberg exhibited a characteristic feature not found in typical fog droplet replicas. Instead of the smooth moon-crater

---

*Typical exposure times for fog drop samples are approximately 0.1-0.5 sec.

appearance characteristic of normal droplet replicas, the replica craters formed by the dense haze droplets were filled with foreign matter and displayed an orange peel texture. The craters were similar in appearance to those which are produced by salt solution droplets. Apparently, the material left by the haze droplets was crystalline residue of the original nucleus.

Surprisingly, relatively high concentrations of large droplets were observed. Typically, calculated drop concentration ranged from 1-4 cm^{-3} and maximum observed drop size was 16-24 μm radius. Drop-size distributions obtained in the dense haze situations at Vandenberg and Los Angeles are presented in Figures 30 and 31, respectively.

As shown by the figures, the observed drop-size distributions are strikingly similar. Note that the largest percentage of droplets was found in the 4-8 μm radius range and that maximum observed drop size was 20 ±4 μm radius.

Several minor differences are also apparent from the data. Note that the drop spectra observed in the Los Angeles haze were narrower and more sharply peaked at somewhat smaller sizes than that of the Vandenberg haze. Note also that maximum observed drop sizes were consistently greater in the Vandenberg haze.

Measurements of nucleus concentrations at varying degrees of saturation were also obtained during the episodes of dense haze. The few observations obtained are shown in Table IV. Note that, as always, the highest nucleus concentrations were observed in Los Angeles. Nucleus concentrations observed on 6 and 7 November, however, were significantly lower than those observed during the Los Angeles radiation fogs of 5 and 9 November and were similar to the averages shown in Table I.

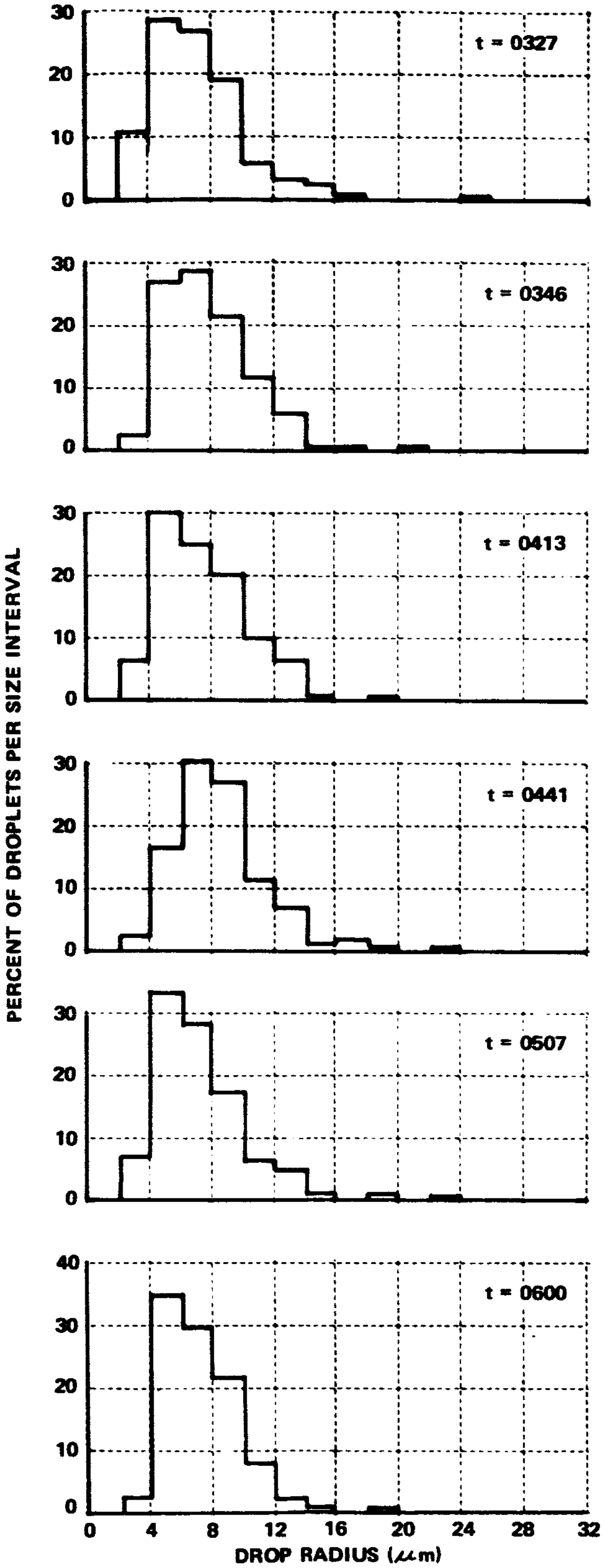

Figure 30 DROP SIZE DISTRIBUTIONS OBTAINED IN DENSE HAZE AT VANDENBERG, 1 OCTOBER 1971

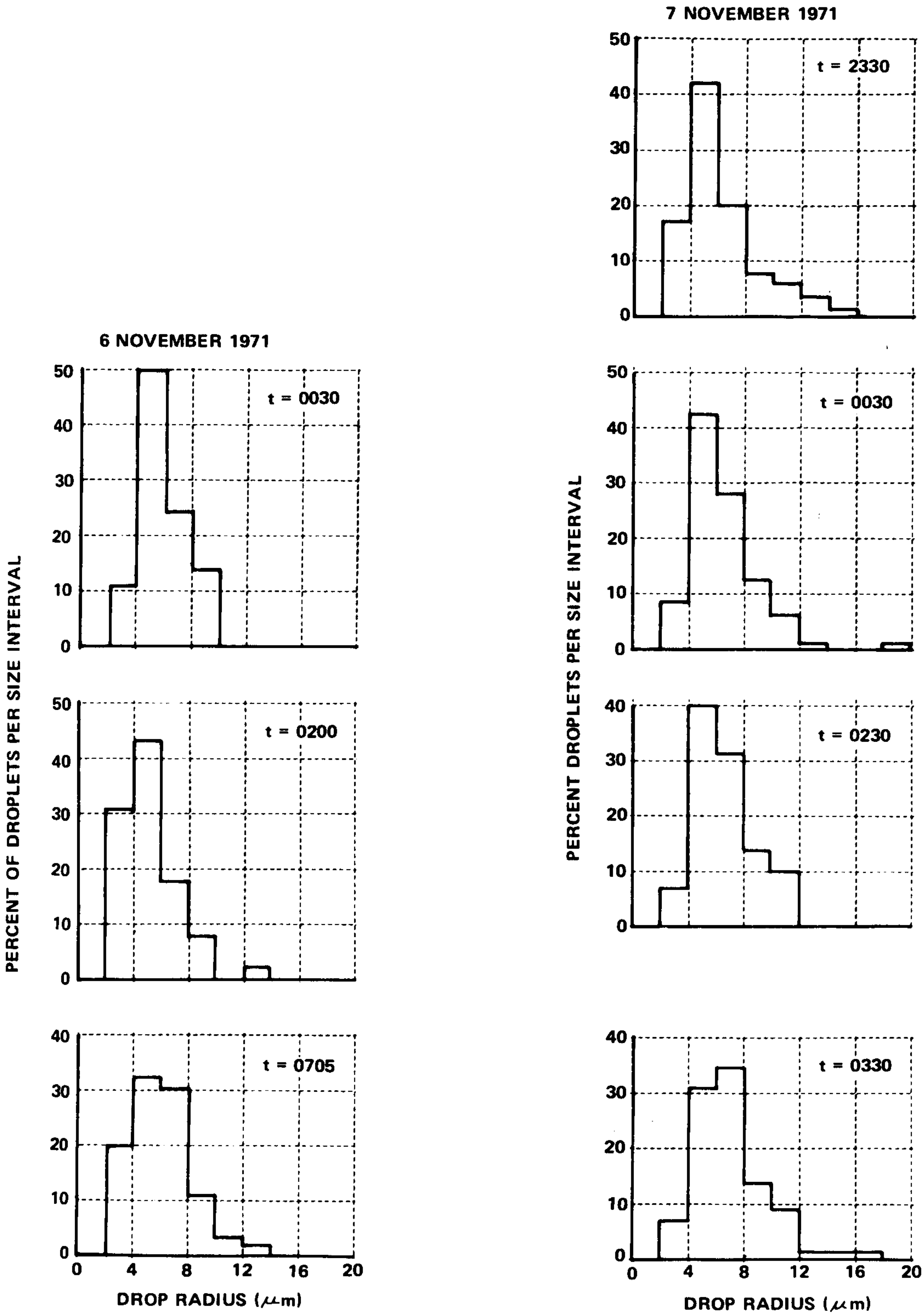

Figure 31 DROP SIZE DISTRIBUTIONS OBTAINED IN DENSE HAZE AT LOS ANGELES, 6 AND 7 NOVEMBER 1971

Table IV

Nucleus Concentrations Measured During
Three Occurrences of Dense Haze

	Nucleus Concentrations (cm^{-3})				
	Haze		Cloud		Aitken
Site/Date	95%RH	100%RH	0.3%S	1.0%S	
VAN (1 Oct)	40	70	--	--	3000
LAX (6 Nov)	200	250	800	3000	15,000
LAX (7 Nov)	325	---	900	1500	6000-10,000

4. Discussion and Summary

During the field trips to Vandenberg and Los Angeles, three occurrences of dense haze were observed: one at Vandenberg and two at Los Angeles. The episodes of dense haze were characterized by visibility restrictions of 4-10 km and occurred under differing meteorological conditions. Wind speed and direction, temperature, cloud cover, and nucleus concentration differed on each occasion. However, meteorological conditions were such that relative humidity increased to approximately 90% (±5%). Deliquescence and growth of hygroscopic particulates (both natural and man-made) to micron sizes at high relative humidities were responsible for the observed visibility restrictions.

F. NUCLEUS SURVEYS

In addition to in-fog measurements and routine observations of nucleus concentration, several nucleus surveys were conducted in the vicinity of Los Angeles and Vandenberg, California. The most informative of these surveys were the result of nucleus observations made at various distances inland from the Pacific shoreline. Data were obtained at locations ranging from 50 m to 20 km inland on days when winds were from the west at each of the coastal sites. Time and instrument problems permitted only one downwind-inland profile at each site. These data are shown in Figure 32 and compared with similar data obtained in February 1970 on the Pacific coast of Washington.

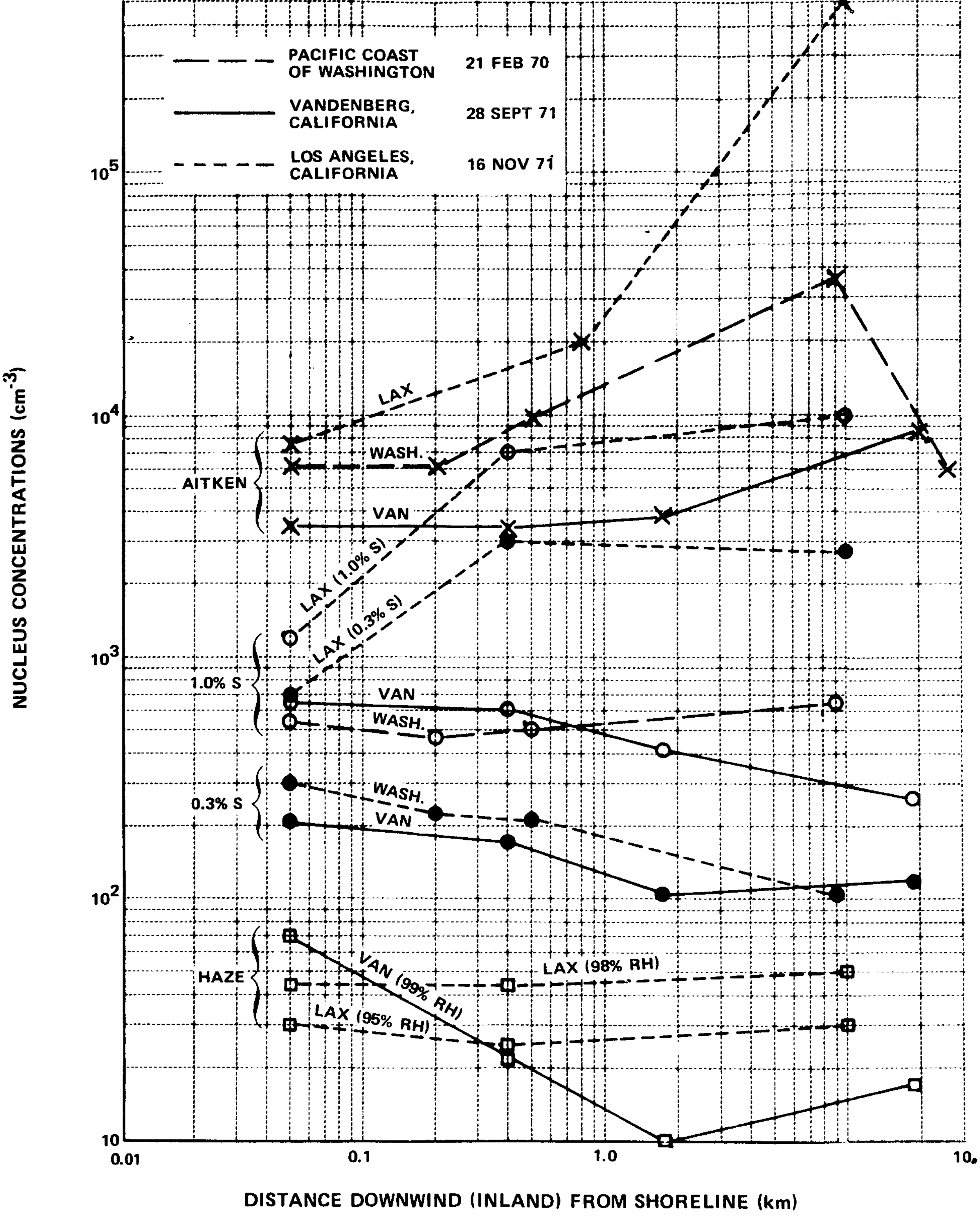

Figure 32 COMPARISON OF NUCLEI CONCENTRATIONS AS FUNCTIONS OF DISTANCE INLAND FROM THE PACIFIC OCEAN AT THREE DIFFERENT LOCATIONS

Recognizing that these data represent only one set of measurements at each site, we cannot make meaningful comparisons of absolute concentrations. However, the data indicate trends in the nucleus concentrations which are thought to be representative of these areas. Note, for example, that in the extremely clean, pollution-free areas of Vandenberg and the Washington shoreline, nucleus concentrations at supersaturations $<1.0\%$ decrease with distance inland while the total particulate (Aitken) concentration increases steadily downwind of the shoreline. It is likely that the decreasing inland concentration of large haze and cloud nuclei is a result of losses of some of the ocean-generated sea-salt nuclei. The increase in the total (Aitken) particulate concentration, however, is brought about by multiple land sources including those attributable to human activities.

In Los Angeles, nuclei of all types were found to increase with distance inland from the Pacific shoreline. Here the losses of sea-salt nuclei were more than compensated for by the addition of nuclei from a large number of inland sources that are common to the area. In addition, the daily production of photochemical aerosol in the Los Angeles Basin frequently results in an aged aerosol which is rich in effective haze and cloud nuclei, as was the case in this particular survey.

IV. A NUMERICAL MODEL OF ADVECTION FOG

A. INTRODUCTION

As part of this year's program effort, a two-dimensional numerical model was developed to investigate the formation of advection fogs and their dissipation by natural and artificial heating. The model predicts the evolution of potential temperature, water vapor content, and liquid water content in a vertical plane as determined by vertical turbulent transfer and horizontal advection. The model utilizes a grid system consisting of an upward expanding vertical grid with 55 grid levels through the first kilometer of the atmosphere, and, horizontally, up to 40 grid columns with variable spacing.

Starting from horizontally-uniform initial conditions, horizontal discontinuities in the surface temperature are introduced and the finite-difference equations of the model are integrated in time until the computed solutions evolve to a steady state. In this manner, the model is designed to simulate the formation or dissipation of advection fog as steady-state processes driven by horizontal discontinuities in the surface temperature.

The two-dimensional advection fog model incorporates several features of an earlier one-dimensional radiation fog model (Pilié et al., 1972) developed at CAL. The vertical exchange coefficients for turbulent transfer depend upon height and predicted local stability, as well as two parameters: friction velocity and roughness length. The influences of infrared absorption and radiation by fog, and fog drop sedimentation are also included in the model. It is also important to cite an analytical treatment of advection fog formation in a classical paper by Rodhe (1962), and the Fisher and Caplan (1963) demonstration of the feasibility of simulating advection fog formation and dissipation by means of a numerical model.

The physical and mathematical foundations of the numerical model are presented in Section B. Documentation of the computer program for the two-dimensional advection fog model is provided in Appendix A. In Section C, results of preliminary numerical experiments on the formation and dissipation of warm-air advection fog are discussed. While the usefulness and basic capabilities of the two-dimensional advection fog model are demonstrated, considerable potential for important research with the model remains. Recommendations are presented in Section D for future numerical modeling research which builds upon the initial advection fog model development and testing in the present study.

B. NUMERICAL MODEL

1. Major Assumptions

The following assumptions are adopted in the numerical modeling study of advection fog:

a) The model is two-dimensional in the X-Z plane. All of the quantities are uniform in the Y direction.

b) The turbulent exchange coefficients for the vertical diffusion of heat, water vapor, and liquid water are equal.

c) In the absence of fog, radiative flux divergence in the atmosphere is neglected.

d) Supersaturated water vapor condenses instantaneously until saturation is achieved. Liquid water in an unsaturated region evaporates instantaneously until saturation is achieved or the liquid water is exhausted.

2. Equations

- List of Symbols

In order to avoid lengthy explanations in the text, a list of the most important symbols employed will be given first:

T, θ	temperature and potential temperature of air
r	water vapor mixing ratio
r_s	saturation mixing ratio
w	liquid water mixing ratio
z	height coordinate
k	subscript denoting k th vertical grid level
x	horizontal coordinate

i	subscript denoting i th horizontal grid column
t	time
n	superscript denoting n th time step
U	horizontal wind speed
K	turbulent exchange coefficient for vertical transfer
ρ	density of air
C_p	specific heat of air at constant pressure
R	net upward flux of infrared radiation
σ	Stefan-Boltzmann constant
P	air pressure
L	latent heat of condensation
V_t	mean terminal velocity of fog drops
k_w	mean mass absorption coefficient of fog for infrared radiation (cm^2g^{-1})
g	gravitational constant
u^*	friction velocity
k	von Karman constant = 0.4

- Major Equations

The equations employed in the model for the time rate change of potential temperature θ, water vapor mixing ratio r, and liquid water mixing ratio W are:

$$\frac{\partial \theta}{\partial t} = - U \frac{\partial \theta}{\partial X} + \frac{\partial}{\partial z}\left(K \frac{\partial \theta}{\partial z}\right) + \frac{1}{\rho C_p}\left(\frac{1000}{P}\right)^{2/7}\left(L \cdot C - \frac{\partial R}{\partial z}\right) \tag{4}$$

$$\frac{\partial r}{\partial t} = - U \frac{\partial r}{\partial X} + \frac{\partial}{\partial z}\left(K \frac{\partial r}{\partial z}\right) - C \tag{5}$$

$$\frac{\partial W}{\partial t} = - U \frac{\partial W}{\partial X} + \frac{\partial}{\partial z}\left(K \frac{\partial W}{\partial z}\right) + C + \frac{\partial}{\partial z}\left(V_t W\right) \tag{6}$$

- Saturation Adjustment

The symbol C denotes a source function for condensation or evaporation. In the actual model, the finite-difference approximations to Eqs. (4) through (6) are integrated for a time step, neglecting condensation or evaporation. Then, the saturation adjustment procedure developed by McDonald (1963) is applied to the new values of θ , r , and W . Taking into account the heating of the air by the release of latent heat of condensation, supersaturated water vapor at a grid point is converted into liquid water until saturation is achieved. Similarly, taking into account the cooling of the air, liquid water at a grid point is evaporated into an unsaturated vapor until saturation is achieved or the liquid water is exhausted.

• Exchange Coefficients

As in an earlier radiation fog model (Pilié et al., 1972), the most difficult area in the development of the advection fog model was in providing realistic turbulent exchange coefficients for the vertical transfer of heat and moisture over wide ranges of height and stability. The treatment of the exchange coefficients adopted in the present model is based to a large extent on that employed in the earlier model. In that formalism, the exchange coefficients were assumed to be a function of the local stability, not just the surface heat flux as in a constant flux layer. On the other hand, since the horizontal wind is not a prognostic variable, the friction velocity $u^*=\sqrt{\tau/\rho}$, where τ is the shear stress, is treated as an input parameter in the model.

It is assumed in the model that the exchange coefficients for heat, water vapor, and liquid water are equal. The functional dependence of the exchange coefficients upon local stability and height in the model is based upon the so-called KEYPS formula (Lumley and Panofsky, 1964)

$$S^4 - \gamma \frac{z}{L} S^3 = 1 \tag{7}$$

for the dependence of non-dimensional wind shear

$$S = \frac{kz}{u^*} \frac{\partial v}{\partial z} \tag{8}$$

upon height z and the scaling length

$$L = \frac{-u^{*3} \rho C_p T}{k g H} \tag{9}$$

Here, H is the vertical heat flux and γ is an empirical constant which is assumed to be 14 after Lumley and Panofsky.

The KEYPS formula is an interpolation between free and forced convection and has been shown to be in reasonable agreement with observations in the constant flux layer extending 10-100 meters above the surface, where τ and H are approximately constant. Assuming that the exchange coefficients for momentum and heat are equal and that H is the local heat flux, the KEYPS formula yields an explicit relationship for the exchange coefficients as a function of height and stability. In the present fog model, this relationship is applied throughout the entire depth of the model atmosphere.

By definition of the exchange coefficient for momentum K_m, the non-dimensional wind shear can be written in the form

$$S = \frac{k u^* z}{K_m} \tag{10}$$

By definition of the exchange coefficient for heat K_h, the vertical heat flux is

$$H = -\rho C_p K_h \frac{\partial \theta}{\partial z} \tag{11}$$

Substituting this expression for H into Eq. (9), the scaling length can be written

$$L = \frac{u^{*3} T}{k g K_h \frac{\partial \theta}{\partial z}} \tag{12}$$

Now substituting Eq. (10) and Eq. (12) into KEYPS formula, Eq. (7), and asserting $K_h = K_m = K$, we obtain

$$(kz)^4 \left[\left(\frac{u^*}{K} \right)^4 - \gamma \frac{g}{T} \frac{\partial \theta}{\partial z} \left(\frac{1}{K} \right)^2 \right] = 1 \tag{13}$$

Solving Eq. (13) for K, we obtain the expression

$$K = \frac{kz}{\sqrt{2}} \left\{ -\gamma \frac{g}{T} \frac{\partial \theta}{\partial z} (kz)^2 + \left[\left(\gamma \frac{g}{T} \frac{\partial \theta}{\partial z} (kz)^2 \right)^2 + 4 u^{*4} \right]^{1/2} \right\}^{1/2} \tag{14}$$

used in the model for K as a function of z, $\partial\theta/\partial z$, and the parameter u^*.

It can be verified that when $\left|\gamma \frac{g}{T} \frac{\partial\theta}{\partial z}(kz)^2\right| << 2u^*$, Eq. (14) reduces to the expression for a neutral atmosphere

$$K = ku^* z \tag{15}$$

In the limit $\gamma \frac{g}{T} \frac{\partial\theta}{\partial z}(kz)^2 >> 2u^{*2}$ occurring under stable conditions, it can be shown that

$$K = \frac{u^{*2}}{\left[\gamma \frac{g}{T} \frac{\partial\theta}{\partial z}\right]^{1/2}} \tag{16}$$

independent of z.

In the limit $-\gamma \frac{g}{T} \frac{\partial\theta}{\partial z}(kz)^2 >> 2u^*$ occurring under unstable conditions, it can be shown that

$$K = \left[-\gamma \frac{g}{T} \frac{\partial\theta}{\partial z}\right]^{1/2} (kz)^{3/2} \tag{17}$$

independent of u^*.

To permit the incorporation of a dependence upon roughness length z_0 into the values of K near the surface, the height z was replaced by the quantity $(z + z_0)$ in Eq. (14). Since the K dependence for neutral conditions (Eq. (15)) prevails near the surface, regardless of stability, K now becomes $K = ku^*(z + z_0)$, in agreement with velocity profiles under neutral conditions (Lumley and Panofsky, 1964).

In a cloud or fog, a moist adiabatic lapse rate is neutrally stable rather than a dry adiabatic lapse rate. Therefore, when K is evaluated in fog, $\partial\theta/\partial z$ in Eq. (14) is replaced in the model by the expression

$$\frac{\theta}{T}\left(\frac{\partial T}{\partial z} + \Gamma_m\right) \tag{18}$$

where Γ_m is the local moist adiabatic lapse rate. In practice, the model fogs are sufficiently close to the surface so that the ratio θ/T can be replaced by unity.

In certain of the numerical experiments with the advection fog model, the exchange coefficients were modified aloft according to the relationship

$$K(z) = K(z_h) \cdot \left(\frac{z_T - z}{z_T - z_h} \right)^2 \quad z \geq z_h \tag{19}$$

where z_h is an estimated height of the constant flux layer, $K(z_h)$ is a value obtained from Eq. (14) at height z_h, and z_T is the top of the model grid system near 1 km.

The criterion $z_h^2 / 4K(z_h) \approx$ ten minutes, employed by Sasamori (1970) in a boundary layer study, was applied in each vertical column of the model at each time step to dynamically determine z_h. The objective of this modification was to eliminate an extreme discontinuity in exchange coefficients which was produced in the original formalism at a boundary between an unstable lower layer and a stable upper layer. This type of discontinuity led to an overproduction of liquid water near the top of a deep fog and accompanying problems in both the radiation and advection fog models.

- Horizontal Advection

In the present model, the prognostic variables are advected by a horizontal wind which may be uniform or vary in the vertical only according to the logarithmic profile for neutral conditions

$$U(z) = \frac{u}{k} \ln \left(\frac{z + z_0}{z} \right) \tag{20}$$

The numerical experiments to be discussed are based on the logarithmic wind profile shown in Table V, corresponding to $u^* = 15\ cm\ sec^{-1}$ and $z_0 = 1\,cm$. It should be noted, however, that provision has been made in the model to allow the incorporation of an additional equation to predict the horizontal wind $U(x, z, t)$ without major programming changes.

Table V

Horizontal Wind Profile

Z (m)	U(m sec^{-1})
0	0
10^{-2}	0.37
10^{-1}	0.86
1	1.72
10	2.59
10^{2}	3.45
10^{3}	4.31

The horizontal advection terms in the differential Eqs. (4) through (6) are approximated in the model by upstream differences which have the form

$$U \frac{\partial Q}{\partial X} = U_{i,k} \frac{(Q_{i,k} - Q_{i-1,k}}{X_i - X_{i-1}} \tag{21}$$

for $U_{i,k} \geq 0$.

When combined with forward time differencing, this finite-difference scheme is computationally stable when

$$U \frac{\Delta t}{\Delta X} \leq 1 \tag{22}$$

Thus, the maximum value of U and the minimum value of the horizontal grid length ΔX determine the maximum value of the time step Δt for which the integration will be stable. If $U_{max} = 4.3\ m\ sec$ and $\Delta X = 100\ m$ then $\Delta t_{max} \approx 23\ sec$.

The upstream differencing scheme has well-known pseudo-diffusive properties (Molenkamp, 1968), which can be expressed in terms of a horizontal pseudo-diffusion coefficient

$$\nu_H = \frac{1}{2} \left| U \right| \Delta X \left(1 - U \frac{\Delta t}{\Delta X} \right) \tag{23}$$

No unique value can be assigned ν_H in the model because U varies in the vertical and ΔX varies in the horizontal in the expanding portions of the horizontal grid. Above a few meters height, however, ν_H generally exceeds $10^2 m^2 sec^{-1}$ in the numerical experiments to be discussed. This results in the rapid damping of short wave length disturbances in the horizontal. While this property of the finite difference scheme would be particularly unattractive in studies of transient solutions, it is not without advantage in the study of forced, steady-state solutions, particularly if the present model is generalized in the future by the incorporation of prognostic fluid dynamic equations.

- Radiation

The treatment of radiation in the present model is designed to capture the essence of physical processes while avoiding detailed radiative transfer calculations. In the absence of fog, the radiative flux divergence $\partial R/\partial z$ in Eq. (4) is assumed to be everywhere zero. The net upward flux of infrared radiation at the surface $R(0)$ is assumed to be a constant fraction β of the blackbody radiation at the surface temperature $T(0)$, i.e.,

$$R(0) = \beta \sigma T^4(0) \tag{24}$$

The constant β is typically taken to be 0.25 (Sutton, 1953), signifying that the back radiation from the atmosphere is assumed to be 0.75 of the full blackbody radiation from the surface.

In the presence of fog, a radiative flux divergence $\partial R/\partial z$ resulting from absorption and reradiation by the fog drops is introduced in Eq. (4). Representing the influence of fog drops by a single spectrally-averaged mass absorption coefficient k_w and neglecting temperature gradients in the fog, the radiative flux at a height z in the fog is given by

$$R(z) = \beta \sigma T^4(0)\, e^{-1.6 k_w \rho \int_z^{z_t} w(z')\,dz'} \tag{25}$$

where z_t is the top of the fog and the effect of the angular dependence of the radiation field has been approximated by using the diffusivity factor 1.6 (Goody, 1964). Differentiating with respect to z, the radiative flux divergence at height z is given by

$$\frac{\partial R}{\partial z} = \beta \sigma T^4(0) \; 1.6 \, k_w \rho w(z) \, e^{-1.6 k_w \rho \int_z^{z_t} w(z') dz'} \tag{26}$$

In the model, the integrals over w are evaluated numerically.

In the Rayleigh limit $r/\lambda << 1$, the absorption cross section of water drops is proportional to r^3 (Batten, 1959). The results of Stephens (1961) show that spectrally-averaged absorption cross sections for blackbody radiation are virtually independent of temperature in the temperature range of interest to this study, and approximately proportional to r^3 for drop sizes up to $r = 5 \mu m$. Based upon these results of Stephens, a mean mass absorption coefficient $k_w = 1.5 \times 10^3 cm^2 g^{-1}$ was deduced and was applied in the model.

This treatment of radiative transfer in a fog would not be a satisfactory approximation for a fog which has a significant number of drops with $r > 10$ μm, since the spectrally-averaged absorption cross sections for large drops are approximately proportional to r^2 (Zdunkowski and Nielsen, 1969), and scattering becomes increasingly important in the radiative transfer as the drop sizes increase. It also should be noted that use of a spectrally-averaged absorption coefficient for blackbody radiation is less than accurate for the back radiation from the atmosphere, which is deficient in the water vapor window near $\lambda = 10$ μm. In spite of these shortcomings, this simple treatment provides a roughly quantitative simulation of the reduction of the net upward radiation at the surface by fog and of the accompanying radiative cooling of the fog.

- Terminal Velocity of Fog Drops

In the model, the sedimentation of the fog drops is simulated through the mean terminal velocity V_t in Eq. (6). Satisfactory results have been achieved by assuming that the total drop concentration remains constant, rendering V_t a function of the local liquid water mixing ratio W only. Under this assumption, V_t is negligible until the liquid water content approaches values observed in well-developed fogs.

The liquid water mixing ratio w can be written

$$w = N \frac{4\pi}{3} \frac{\rho_w}{\rho} r^3 \tag{27}$$

where N is the number of drops per unit volume, r is the mean volume radius of the drop-size distribution, ρ_w is the density of liquid water, and ρ is the air density. Eq. (27) can be solved for r and the result substituted in the Stokes relationship (Fletcher, 1966)

$$V_t = 1.2 \times 10^6 r^2 (cgs\ units) \tag{28}$$

for terminal velocity of water droplets under 20 μm in radius. The resulting expression is

$$V_t = 5.3 \times 10^3 \left(\frac{w}{N}\right)^{2/3} \tag{29}$$

where N is number drops cm^{-3}.

Assuming a constant drop concentration $N = 50 cm^{-3}$, reasonably representative of coastal advection fogs (Jiusto, 1964), Eq. (29) reduces to the expression

$$V_t = 4 \times 10^2 w^{2/3}\ cm/sec \tag{30}$$

employed in the model. For a liquid water mixing ratio $W = 2.44 \times 10^{-4}$ corresponding to liquid water content of approximately $0.30 g m^{-3}$ Eq. (30) yields $V_t = 1.5\ cm\ sec^{-1}$.

3. Initial Conditions

At each vertical grid level in the model, the initial values of the prognostic variables θ , r , and W are uniform in the horizontal. The model permits initialization with observed or theoretical vertical distributions of θ , r , and W . In the fog dissipation cases to be discussed, for instance, the model was initialized with vertical distributions predicted by the model in an earlier fog formation experiment.

For testing purposes and fog formation studies, the model can be initialized with certain idealized vertical distributions of the prognostic variables. The initial distribution of potential temperature can be either adiabatic ($\theta = const$) or isothermal ($T = const$). The water vapor mixing ratio r can be initiated with a uniform distribution with height. In fog formation studies, the liquid water mixing ratio W is initialized to be zero everywhere.

4. Boundary Conditions

At the surface, a no flux boundary condition $\left.\frac{\partial r}{\partial z}\right)_{z=0} = 0$ on water vapor mixing ratio was maintained in the numerical experiments to be discussed. The influences of alternative surface boundary conditions on r, such as saturation at the temperature of the surface, remain to be investigated. The liquid water mixing ratio W was maintained equal zero at the surface.

The basic objective in both the fog formation and fog dissipation experiments with the present model was to study the response of the model atmosphere to discontinuities in the surface temperature. Since the initial condition is a uniform surface temperature, the surface temperature discontinuities are introduced gradually over a ten-minute time period in the cases to be discussed to avoid sudden pulsing of the model at the start of the integration. The model has satisfactory handled temperature discontinuities as large as 20°C when introduced over the first ten minutes of an experiment. In principle, the model allows any structure of the surface temperature to be introduced.

The upper boundary of the grid system at $z \approx 1$ kilometer is assumed to be an undisturbed level. There, the prognostic variables are maintained equal to their uniform ($in\ x$) initial values throughout a numerical experiment.

At the upwind boundary of the grid system, the prognostic variables remain unchanged from their initial values during an integration. At the downwind boundary, however, the values of the prognostic variables are continually adjusted to be equal to their computed values in the adjacent upwind column of the grid system. The only mechanism for the upwind propagation of information in the present model is the pseudo-horizontal diffusion introduced by the finite-difference approximation to the horizontal advection terms. Nevertheless, it has been considered prudent to expand the grid system sufficiently far downwind to prevent significant contamination of the region of interest by any deleterious influences emanating from the downwind boundary condition.

5. Computational Procedure

- Grid System

In the vertical grid employed in the model, the spacing between adjacent grid levels expands upward from the surface. The expanding grid system provides high resolution near the surface where the variables of the model change rapidly with height and removes the upper boundary from the region of primary change, without requiring a prohibitively large number of grid levels. In the numerical experiments to be discussed, 55 grid levels have been employed with the grid spacing expanding upward by a factor of 1.2 per level from an initial spacing of 1 cm between the first grid level in the atmosphere and the surface. The upper boundary was 157 m above the next highest grid level and 943 m above the surface.

In the horizontal grid system, the grid expands both upwind and downwind about an interior region with uniform grid spacing. Within the limitation of a maximum of 40 horizontal grid columns, the model permits great flexibility in specifying the horizontal grid parameters for different applications. Numerical experiments on the artificial dissipation of advection fog by surface heating, for example, were based on an interior region of 10 grid columns spaced 100 m apart, with ten column grids expanding both upwind and downwind for approximately 10 km. Here, as in other numerical experiments to be discussed, the horizontal grid spacing expands by a factor of 1.4 per grid column in the expanding regions.

- Implicit Integration

Since the vertical grid has very fine grid spacing near the surface, it was necessary to adopt an implicit treatment of the vertical diffusion terms in the partial differential equations of the model (Eqs. (4) - (6)) in order to obtain computationally stable solutions using reasonably large time steps.

Omitting the symbolic source term C for condensation, the finite-difference equations employed in the model can be written in the form

$$\frac{\theta^{n+1}-\theta^{n}}{\Delta t} = -U\frac{\delta\theta^{n}}{\delta x} + \frac{\delta}{\delta z}\left(K^{n}\frac{\delta\theta}{\delta z}^{n+1}\right) - \frac{1}{\rho C_p}\left(\frac{1000}{p}\right)^{2/7}\frac{\partial R^{n}}{\partial z} \tag{31}$$

$$\frac{r^{n+1}-r^{n}}{\Delta t} = -U\frac{\delta r^{n}}{\delta x} + \frac{\delta}{\delta z}\left(K^{n}\frac{\delta r}{\delta z}^{n+1}\right) \tag{32}$$

$$\frac{W^{n+1}-W^{n}}{\Delta t} = -U\frac{\delta W^{n}}{\delta x} + \frac{\delta}{\delta z}\left(K^{n}\frac{\delta W}{\delta z}^{n+1}\right) + \frac{\delta\left(V_t^{n}W^{n+1}\right)}{\delta z} \tag{33}$$

where n and $n+1$ denote values known at the end of successive time steps. Thus, the horizontal advection terms, the radiative flux divergence $\frac{\partial R}{\partial z}$, the exchange coefficient K, and the mean terminal velocity of the fog drops V_t are computed from the known values of the prognostic variables at the end of the previous time step n. The prognostic variables in the vertical diffusion terms and W^{n+1} in the drop sedimentation term are the new values to be determined at the end of time step .

Denoting three adjacent vertical grid levels by $k+1$, k, and $k-1$, the finite-difference expressions in the model for vertical diffusion and drop sedimentation terms in Eq. (33) are

$$\frac{\delta}{\delta z}\left(K^{n}\frac{\delta W}{\delta z}^{n+1}\right) + \frac{\delta\left(V_t^{n}W^{n+1}\right)}{\delta z} = \left(\frac{1}{z_{k+\frac{1}{2}}-z_{k-\frac{1}{2}}}\right) \left[K^{n}_{k+\frac{1}{2}}\left(\frac{W^{n+1}_{k+1}-W^{n+1}_{k}}{z_{k+1}-z_{k}}\right) - K^{n}_{k-\frac{1}{2}}\left(\frac{W^{n+1}_{k}-W^{n+1}_{k-1}}{z_{k}-z_{k-1}}\right)\right] + \left(\frac{V^{n}_{k+1}W^{n+1}_{k+1}-V^{n}_{k-1}W^{n+1}_{k-1}}{z_{k+1}-z_{k-1}}\right) \tag{34}$$

The vertical diffusion terms in Eq. (31) and Eq. (32) are similar.

Denoting a prognostic variable by Q, we see Eqs. (31) - (33) can be placed in the general form

$$D_k^n = -A_k^n Q_{k+1}^{n+1} + B_k^n Q_k^{n+1} - C_k^n Q_{k-1}^{n+1} \tag{35}$$

where A_k^n, B_k^n, C_k^n, and D_k^n are known quantities from the previous time step. There is an equation of this type at each grid level k for each of the prognostic variables. In order to determine the Q^{n+1}'s, this system of simultaneous linear equations must be solved. This is the essence of implicit integration methods.

The general method of solution utilized in the model is based upon the technique of Richtmyer (1957) and will not be discussed in detail here. It is an efficient method which takes advantage of the specialized nature of the equations. Basically, it involves scanning a grid column downward, making use of the upper boundary value at the start to develop linear relations between the Q^{n+1}'s at adjacent grid levels, i.e.,

$$Q_k^{n+1} = E_k^n Q_{k-1}^{n+1} + F_k^n \tag{36}$$

It can be shown that

$$E_k^n = \frac{C_k^n}{B_k^n - A_k^n E_{k+1}^n} \tag{37}$$

and

$$F_k^n = \frac{D_k^n + A_k^n F_{k+1}^n}{B_k^n - A_k^n E_{k+1}^n} \tag{38}$$

with the starting values $E_{kE}^n = 0$ and $F_{kE}^n = Q_{kE}$ at the upper boundary ($k = kE$). Then, starting with the boundary value at the surface, the grid column is scanned upward using the previously determined linear relations (Eq. (36)) to successively determine all the Q^{n+1}'s.

This implicit integration scheme has proven computationally stable for time steps up to 60 sec under stable and unstable thermal stratification, both in the presence and absence of fog. In this regard, the finite-difference approximation to the vertical diffusion terms in the present model is superior to that used in an earlier radiation fog model (Pilié et al., 1972) which had poor stability characteristics under unstable thermal stratification.

- Summary of Computational Sequence

Suppose that all the prognostic and diagnostic variables are known at the end of the nth time step. The $(n+1)$th time step of the integration is accomplished in the following manner:

(1) Since the upstream differencing in the horizontal advection terms (see Eq. (21)) does not depend upon values of the variables downwind of a grid column, the integration is started in the grid column just upwind of the downwind boundary.

(2) Starting from the invariant boundary values at the upper boundary, the implicit integration is initiated by proceeding down the grid column to the first grid level above the surface ($k = 1$), computing the E_k^n's and F_k^n's for θ , r , and W .

(3) If a distribution of surface temperatures is being gradually introduced, the surface temperature is updated. Using the relationship

$$r_1^{n+1} = ER_1^n \cdot r_0^{n+1} + FR_1^n \tag{39}$$

and the no-flux boundary condition $r_0^{n+1} = r_1^{n+1}$, a new surface boundary value

$$r_0^{n+1} = \frac{FR_1^n}{1 - ER_1^n} \tag{40}$$

is computed.

(4) Starting with the surface boundary values $\theta_0^{n+1} = T_0^{n+1}$, r_0^{n+1} , and $W_0^{n+1} = 0$, the new values of θ_k^{n+1} , r_k^{n+1} , and W_k^{n+1} are computed by proceeding up the grid column using the previously determined linear relations (Eq. (36)). At each grid level k , the temperature

T_k^{n+1} is computed from θ_k^{n+1}. If necessary, a saturation adjustment is performed on the values of T_k^{n+1}, r_k^{n+1}, and W_k^{n+1} to account for condensation or evaporation, and an adjusted value of θ_k^{n+1} is computed. Then, new values of the diagnostic variables are computed including the exchange coefficients K_k^{n+1} and the integrals over W_k^{n+1} for the radiative flux divergence. When the vertical scan is completed, an adjusted value $r_0^{n+1} = r_1^{n+1}$ is computed.

(5) Steps (2) through (4) are repeated for each grid column, working upwind toward the upwind boundary.

(6) The values of the prognostic variables on the downwind boundary are updated to equal their computed values in the adjacent upwind grid column. This completes the time step.

C. RESULTS

1. Introduction

As previously stated, the aim of the modeling effort was to initiate development of a two-dimensional numerical model capable investigating advection fog formation and dissipation. This goal was achieved and the capabilities and potentialities of the resulting model are presented in this section. Detailed comparisons between model results and observations cannot be made until more extensive field data are acquired, both for verifying initial model conditions and for comparison with model results. Preliminary comparisons are therefore confined to general fog characteristics such as depth and liquid water content. In the discussion which follows, the capabilities of the model are delineated in terms of formation, natural dissipation, and artificial dissipation of advection fog.

2. Formation of Advection Fog

The model can produce fog of reasonable depth and liquid water content from the advection of moist air over a cold surface. Figure 33 shows an example of the predicted distribution of liquid water content in a fog formed by advecting air with a 1°C surface dew point depression over a

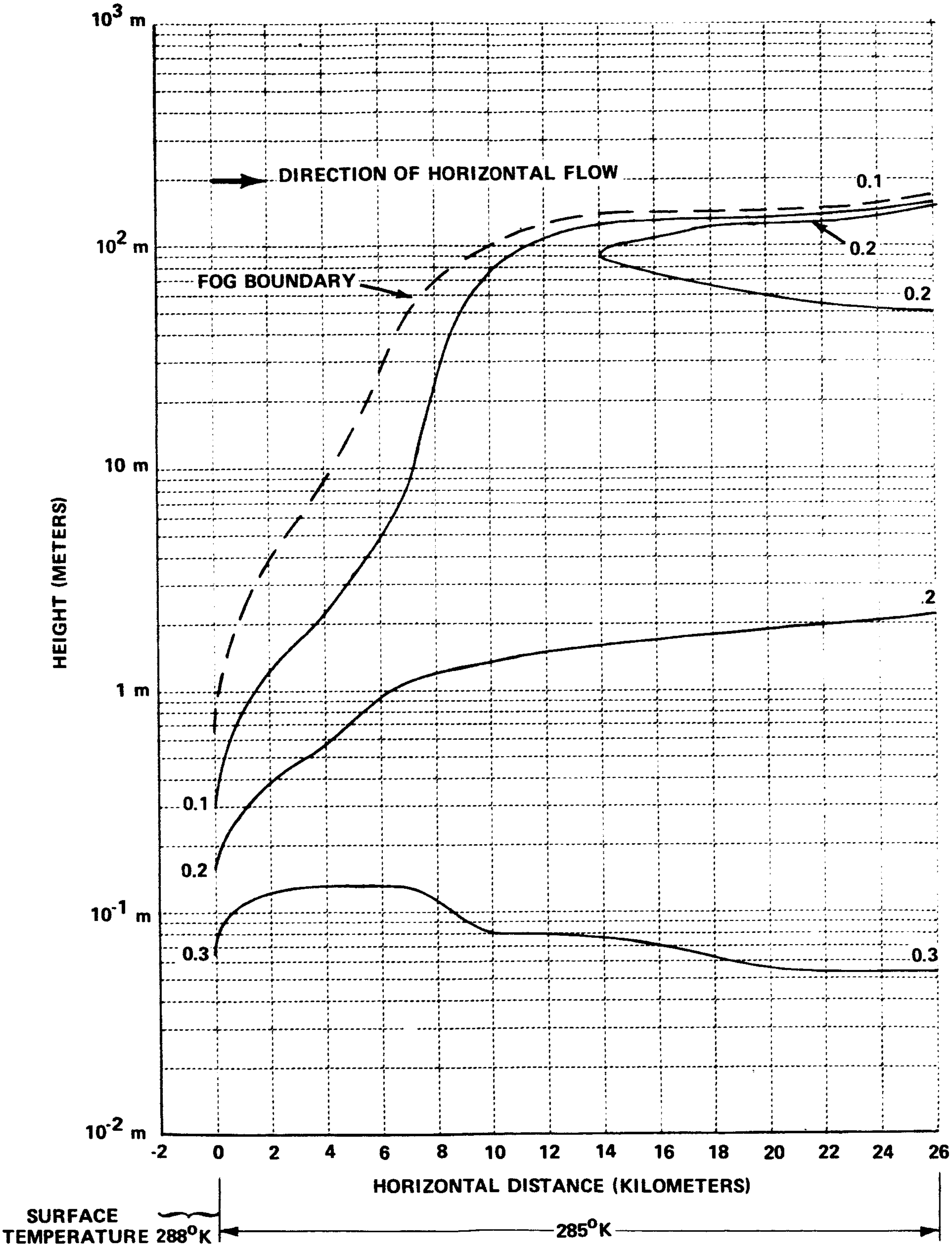

Figure 33 FOG BOUNDARY AND LIQUID WATER CONTENT (IN G M^{-3}) FOR NUMERICALLY SIMULATED ADVECTION FOG

3°C temperature drop at the surface. All simulations used the wind profile shown in Table V (p. 87). The fog top height of 150 m is not unrealistic at this distance downwind from the surface temperature discontinuity. Taylor (1917) shows advection fog with tops of 100 and 200 m, but both values are fog fogs which had a lifetime of the order of a couple of days.

In general, the liquid water values predicted by the model are also realistic. Okita (1962) shows a maximum value of 0.7 g m^{-3} and an average value of 0.5 g m^{-3} for a dense advection-radiation fog. By comparison, considering the small temperature difference and the relatively short time elapsed, the predicted values of 0.2 to 0.3 g m^{-3} are reasonable. The maximum liquid water contents at the surface appear to be a consequence of the no-flux surface boundary condition on water vapor maintained during the numerical simulation. The secondary maximum in liquid water near 100 m is associated with the development of a maximum in radiational cooling near the fog top after the fog depth exceeds a few tens of meters. In addition to the surface cooling, the radiational cooling maximum provides a driving force for fog formation.

Figure 34 shows the vertical profile of radiational cooling as a function of horizontal distance for the fog distribution in Figure 33. The profiles from 0.0 to 6.9 km show a maximum value of cooling at 10 cm, with the cooling extending to progressively higher levels as the fog depth increases. At 9.8 km and beyond, the profiles show a shift of the maximum cooling to the top of the fog as the fog depth reaches 100 m. Beyond 9.8 km, the cooling at the surface progressively decreases, essentially vanishing as the fog develops liquid water content near 0.2 g m^{-3} over its entire 100 m depth. This ability of the model to simulate radiational cooling behavior as a function of a developing fog makes it a powerful tool for studying problems of advective fog formation.

Of the other parameters which this model handles, temperature, eddy heat flux, and turbulent exchange coefficients show interesting features which deserve brief discussion. Profiles of these quantities at 19.8 km, selected from the simulation shown in Figures 33 and 34, are presented in Figure 35 and represent conditions in a fully developed fog.

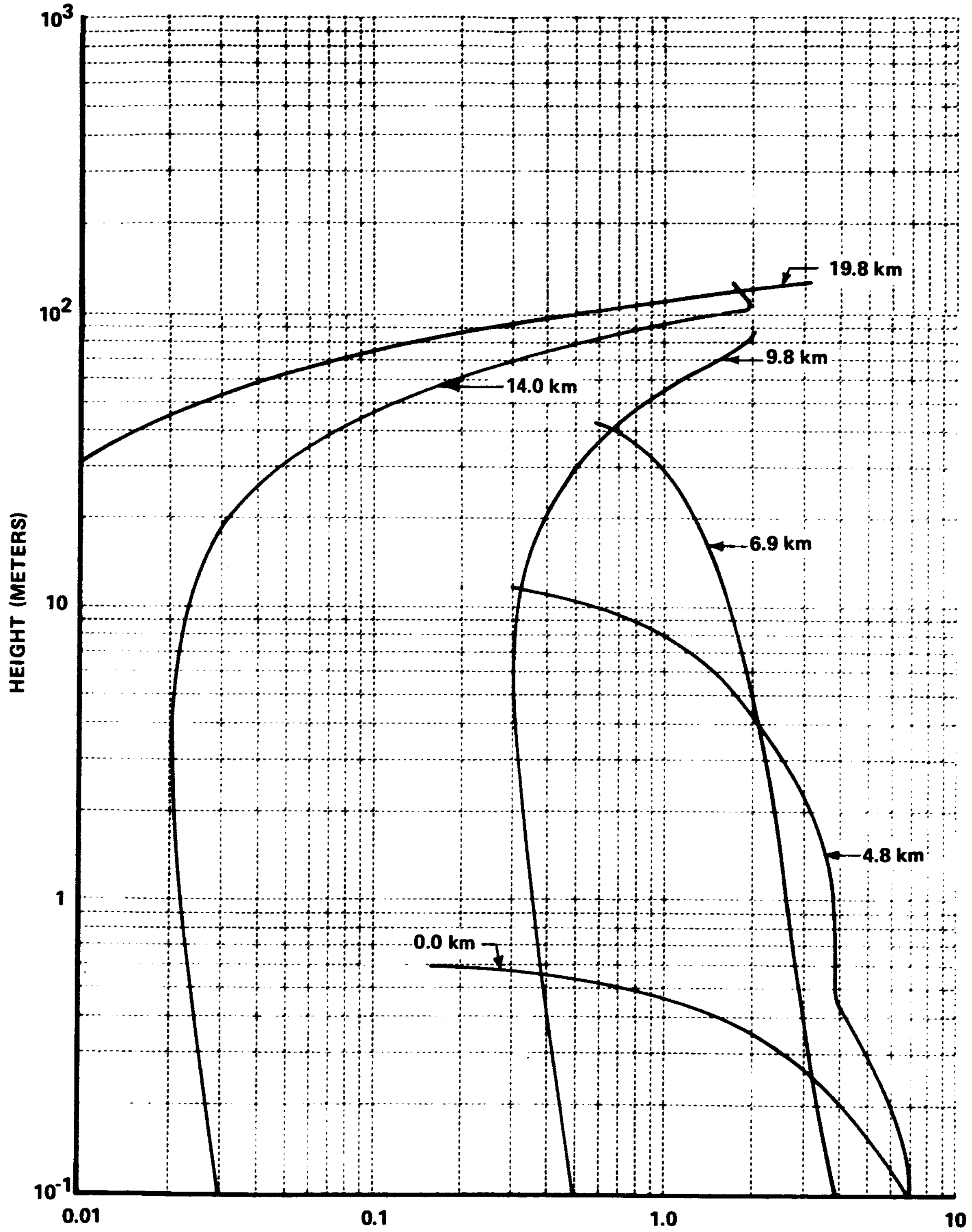

Figure 34 RADIATIVE COOLING PROFILES FOR VARIOUS STAGES OF A DEVELOPING ADVECTION FOG

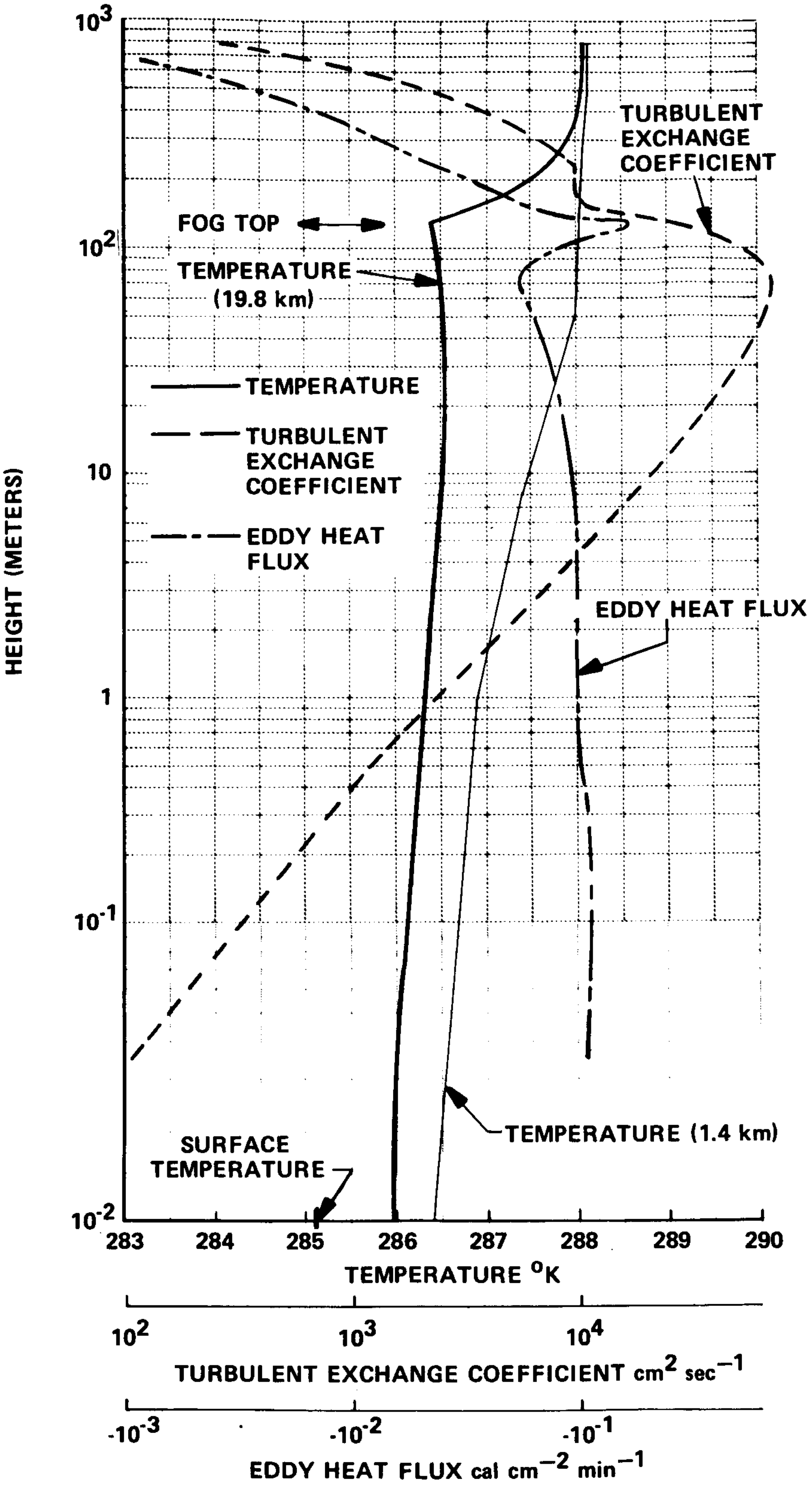

Figure 35 PROFILES OF TEMPERATURE, TURBULENT EXCHANGE COEFFICIENT AND EDDY HEAT FLUX FOR AN ADVECTION FOG

The exchange coefficients were determined by the formalism of Eq. (14) except that they were multiplied by the factor $exp[-z/150m]$ to provide a decrease in the coefficients aloft. However, in this case, with such a large U^* (60 cm sec^{-1}), the exchange coefficients behave as if the stability were neutral (see Eq. (15)). One exception is near the fog top where, because of the steep inversion, K is essentially constant with height through some 70 m.

The temperature profile shows the expected inverted profile through the fog and then a stronger inversion above the fog top. The inversion through the fog is weak for a number of reasons. First, the model has a large temperature jump from the surface value to the value at the first atmospheric level (1 cm), about 0.75°C in this simulation; secondly, the large K smooths out the temperature profile; and finally, the radiational cooling at the fog top drives the upper temperatures down toward the surface temperature. For comparison, the profile at 1.4 km, where the fog is only 3 m deep and the primary influence is cooling from the surface, shows a steeper temperature inversion.

The eddy heat flux profile shows a constant flux region up to 10 m and then a disturbed profile associated with the temperature and K structure at the fog top. In the model, eddy flux in fog depends on the sum of the temperature gradient and the moist adiabatic lapse rate (Eq. 18) so that the region of slight decrease in temperature near the fog top produces a decrease in eddy flux up to 75 m rather than a change in sign. The large peak in eddy heat flux at 127 m is associated with the sharp inversion near the fog top. Though the sharpness and intensity of these distributions may be unrealistic, they show the model's ability to respond to internally developing structure.

As mentioned previously, this simulation used a fairly large U^*, a value chosen in order to quickly obtain a deep fog. The accompanying K values undoubtedly affect the realism of the predicted profiles, especially the temperature profile. More realistic profiles are possible with smaller U^*, but the simulations would require longer computer time to obtain the deep fog.

3. Natural Dissipation of Advection Fog

An example of the predicted distribution of liquid water content in the natural dissipation of an advection fog is shown in Figure 36. In this case, a 200 m deep fog with liquid water contents in the range 0.25-0.3 g m^{-3} advects over a $5^{\circ}C$ temperature rise at the surface. It is seen that the fog is completely dissipated in slightly over 8 km. These data represent fog conditions after three hours of real time and comparison with earlier output shows that this is a quasi-steady state. Considering the warm surface as land, the inland extent of the fog seems reasonable, as does the variation of the lower fog boundary with distance from the coast.

The upward movement of the fog top during dissipation is apparently produced by the increase in exchange coefficients which accompanies the development of an unstable temperature stratification over the warm surface. The formalism for K used in this simulation was that discussed in connection with Eq. (19), with $U^* = 15 \, cm \, sec^{-1}$. The feature introduced by Eq. (19) was designed to eliminate an extreme discontinuity in exchange coefficients, which was produced by Eq. (14) at a boundary between an unstable lower layer and a stable upper layer. This type of discontinuity led to an overproduction of liquid water near the top of a deep fog.

The predicted evolution of the exchange coefficients for the fog dissipation in Figure 36 is shown in Figure 37 along with the corresponding temperature profiles. As the temperature inversion in the unmodified fog gives way to an increasingly unstable temperature stratification over the warm surface, K increases at all levels above 10 m and the height of the maximum value increases. While there is evidence of some artificiality in the vertical distributions of K, the general behavior of the model was significantly improved by the modification to exchange coefficients discussed above, as is seen by the absence of very large liquid water values.

It is important to note that the values of the exchange coefficients near the surface are nearly the same in the three distributions because these values are largely determined by U^* and z_0, which are fixed parameters in the present model. In reality, the value of U^* at the

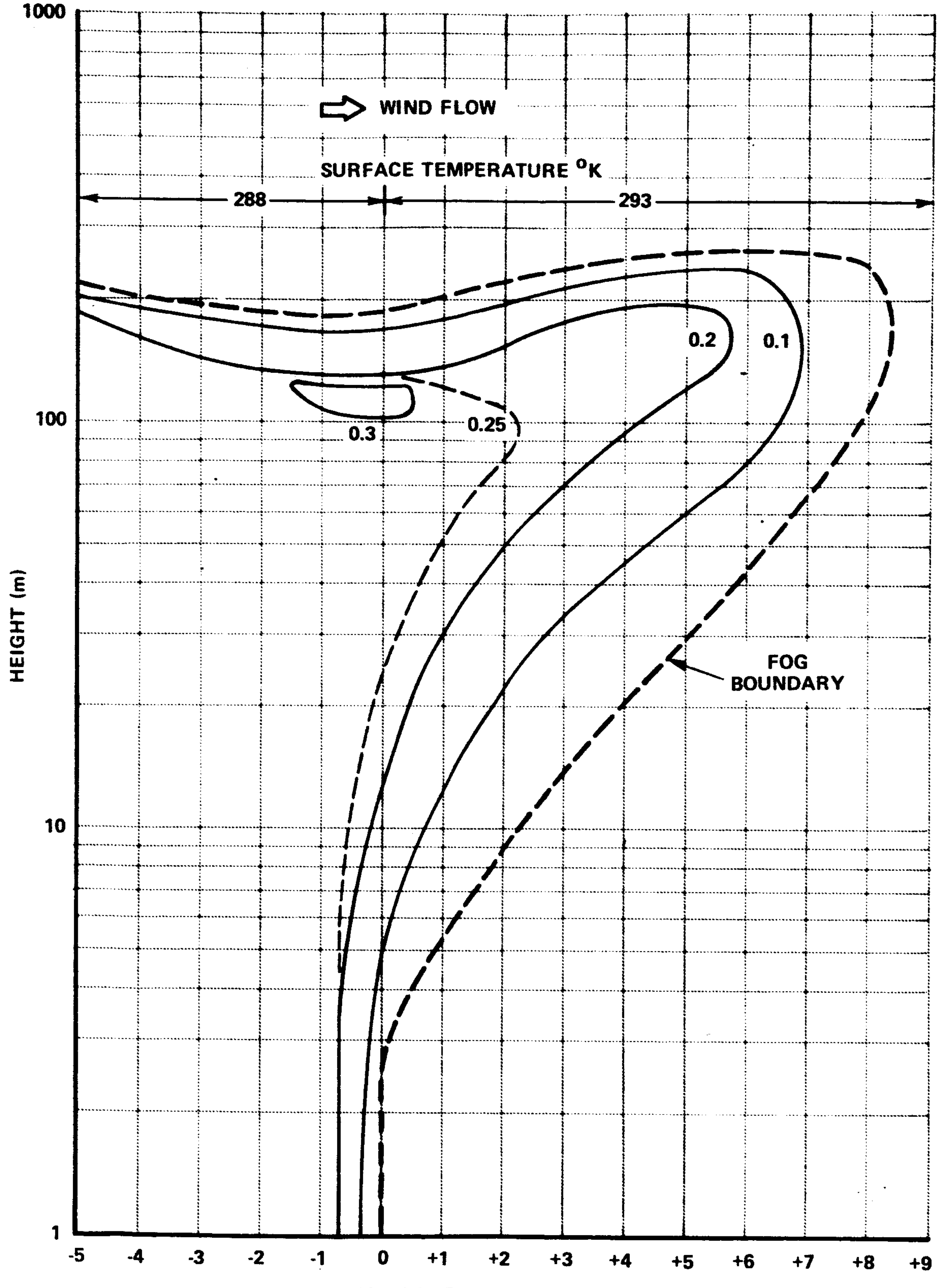

Figure 36 NUMERICAL SIMULATION OF NATURAL DISSIPATION OF AN ADVECTION FOG, ISOPLETHS OF LIQUID WATER CONTENT (G M^{-3})

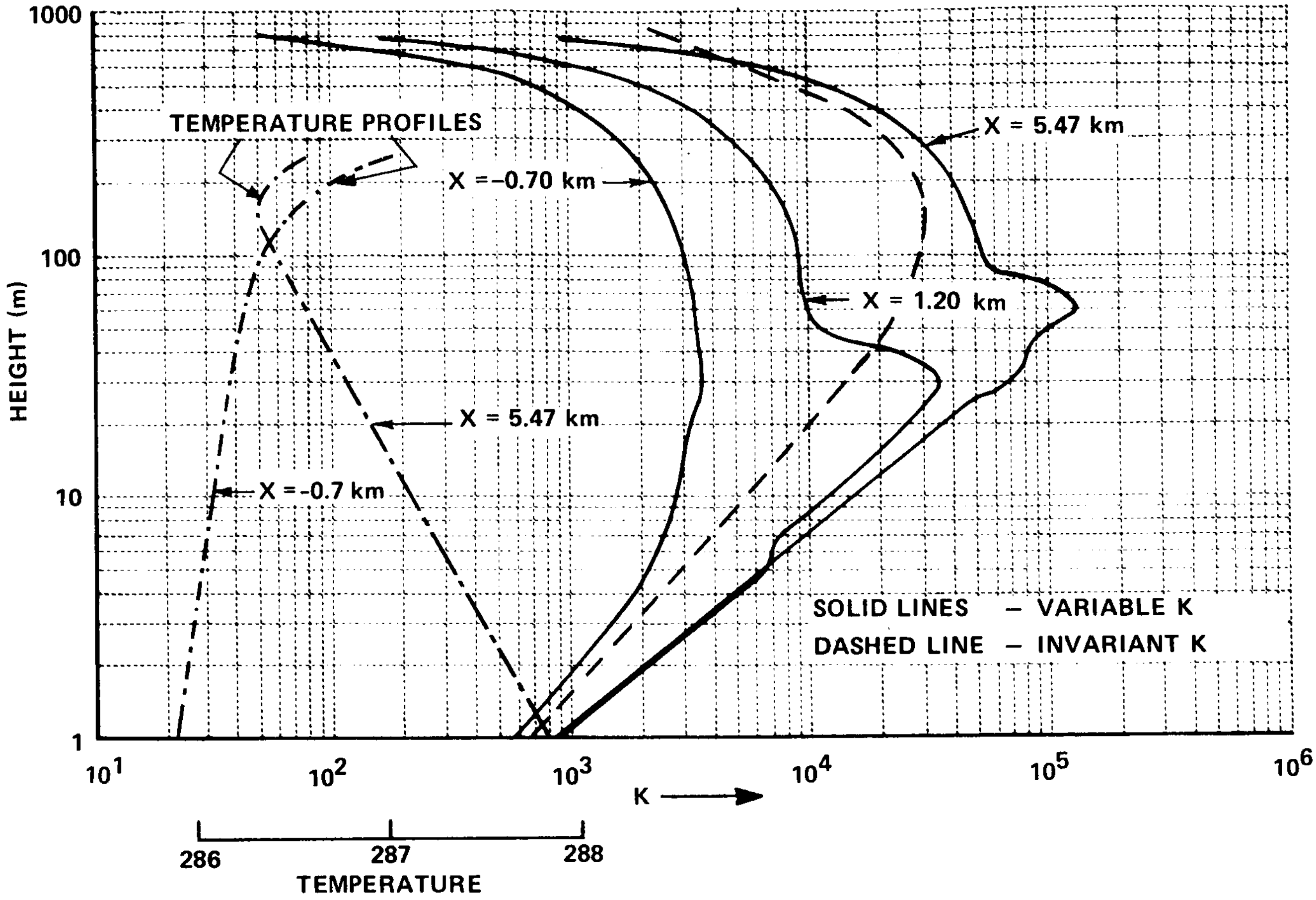

Figure 37 TURBULENT EXCHANGE COEFFICIENT (CM^2 SEC^{-1}) AND TEMPERATURE FROM NUMERICAL SIMULATIONS OF NATURALLY DISSIPATING ADVECTION FOG

surface should increase as the temperature stratification becomes unstable because of a coupling between the momentum exchange coefficients and the horizontal wind profile.

The profiles in Figure 37 show the capability of the model to provide a response of K to the changing temperature profile. This capability is particularly useful for studying fog dissipation whose behavior is sensitive to the structure and evolution of K .

As an example of the dependence of fog dissipation behavior on the K structure, we present Figure 38, which shows the liquid water content field for the same simulation as shown in Figure 36, except that the profile was invariant and given by

$$K(z) = k\, U^{*}\, z \exp\left[-z/150\,m\right] \tag{41}$$

as shown in Figure 37. The difference between these two fog dissipations is obvious: one completely dissipates and the other lifts and forms a fog deck with a base at 50 m and a thickness of 200 m. This result is even more striking since the liquid water content values upwind of the heated region are higher in the completely dissipated case.

Reference to Figure 37 shows that the value of the invariant K is everywhere less than the variable K- value for $X = 3.5\,km$, and less below 40 m for $X = 1.2\,km$. Obviously, in the invariant K case, the turbulent transfer is less and thus the heat transfer from the surface into the fog is less. This condition is verified by Figure 39, which shows the profile of eddy heat flux for the two cases. The profile for the invariant K case shows an essentially steady decrease of the heat flux up into the fog, whereas in the complete dissipation case the magnitude of the heat flux reaches its maximum value within the fog. Consequently, in the former case the horizontal advection and other processes are able to supply liquid water to the upper levels faster than the heating from below can destroy it. This situation is present in the dissipation of coastal advection fogs during morning hours; fog movement over a warmer surface is not necessarily sufficient for complete dissipation; the heat from the surface must be distributed throughout the fog.

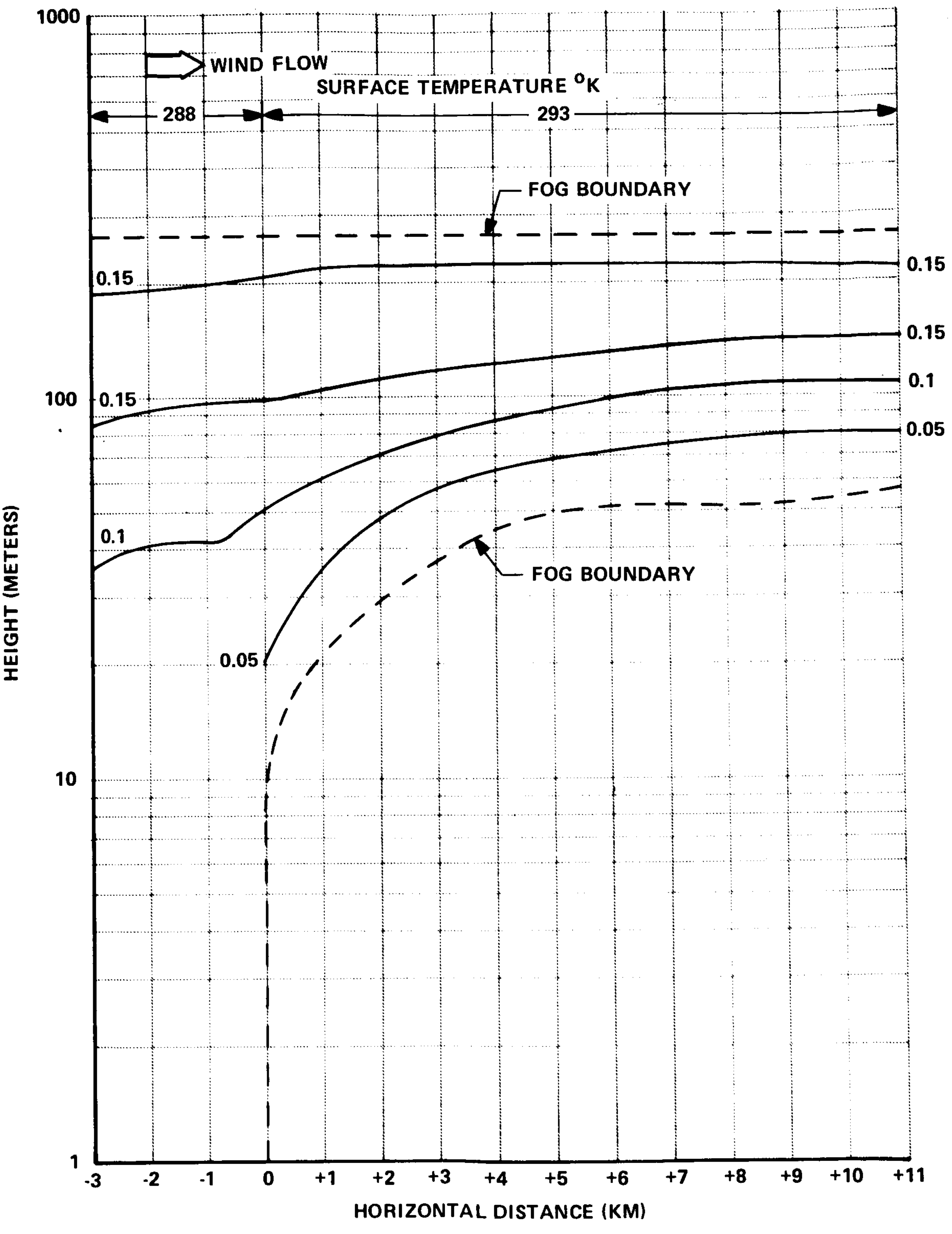

Figure 38 LIQUID WATER DISTRIBUTION (G M^{-3}) IN NATURAL DISSIPATION OF ADVECTION FOG WITH INVARIANT K

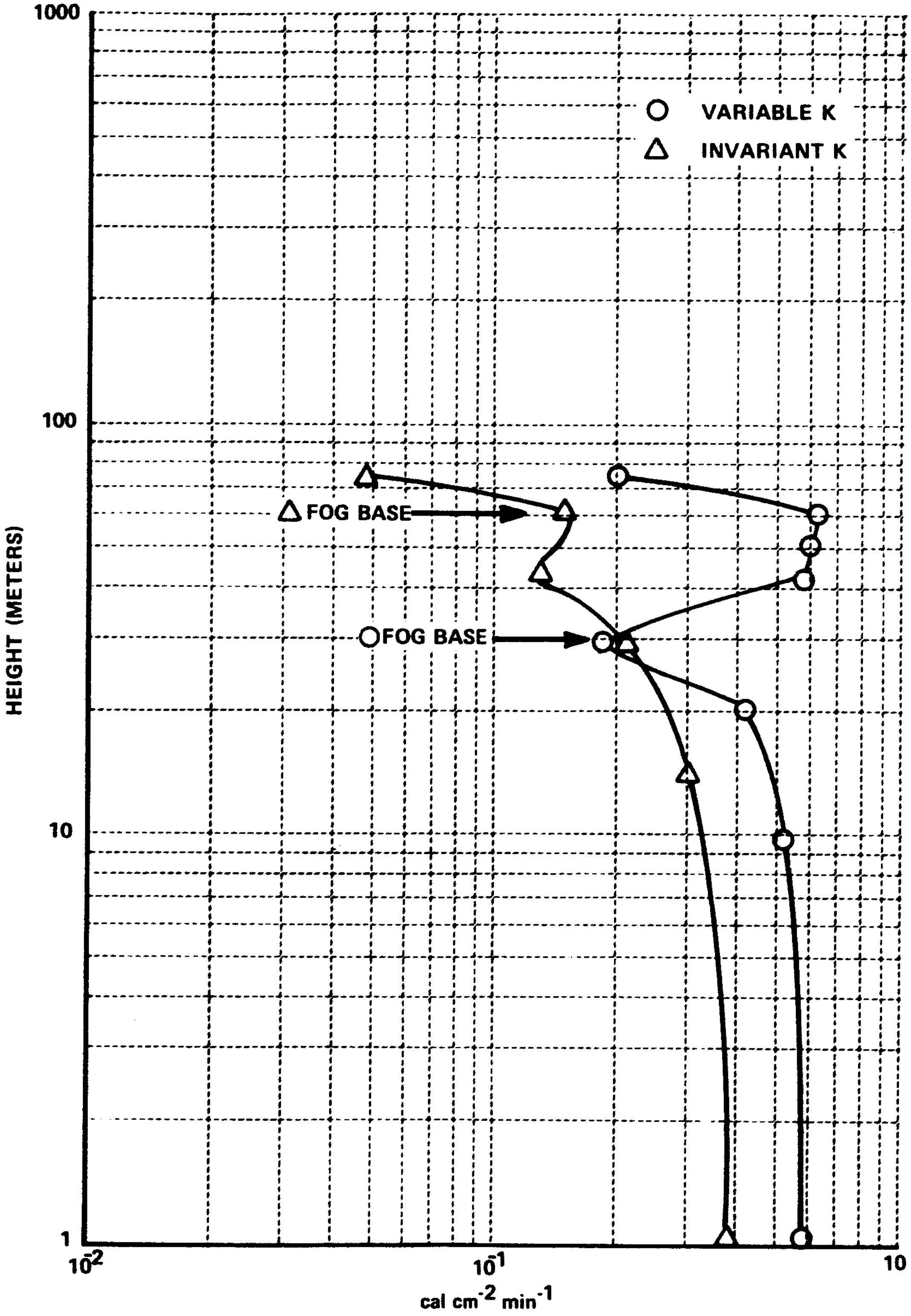

Figure 39 EDDY HEAT FLUX PROFILES FOR VARIABLE AND INVARIANT K-CONDITIONS

4. Artificial Dissipation of Advection Fog

An example of the artificial dissipation of an advection fog by heating is shown in Figure 40. Here, a 300 m wide zone at the surface is maintained 20°C warmer than the surface upstream and downstream of the heated zone. Although the region where complete evaporation of the fog is predicted is only about 17 m high and extends about 800 m downwind, the region of significant fog modification is considerably larger. The total heat input to the atmosphere from the heated zone is approximately 2.5×10^4 cal $\sec^{-1}$ per meter of length normal to the wind. This is roughly a factor of eight less than the maximum design heating capacity to achieve clearing to a height of 60 m in upcoming AFCRL fog dissipation experiments scheduled for July 1972 at Vandenberg, California.

It should be noted, however, that the effects of the artificial dissipation might be significantly greater if superimposed upon a naturally dissipating advection fog. In the present case, active fog forming processes cause the fog to completely re-form downwind of the heated zone. Furthermore, fluid dynamic motions produced by buoyancy forces, which are completely neglected in the present model, would undoubtedly produce a considerably greater vertical extent of the region of significant fog dissipation.

D. CONCLUSIONS AND RECOMMENDATIONS

The basic capabilities of an initial two-dimensional model to simulate both the formation and dissipation of advection fog have been demonstrated. As with all numerical modeling studies, the question arises as to whether future numerical modeling research should be devoted to the further development of the model by the incorporation of additional physical processes or to a full exploitation of the capabilities of the present model with only modest improvements to the modeling framework. It is our belief that important information about the formation and natural dissipation of advection fog can be gained by pursuing the latter alternative.

To fully exploit the capabilities of the present model, a systematic study of influences of the initial conditions, the boundary conditions, and the important physical parameters upon the predicted results should be carried

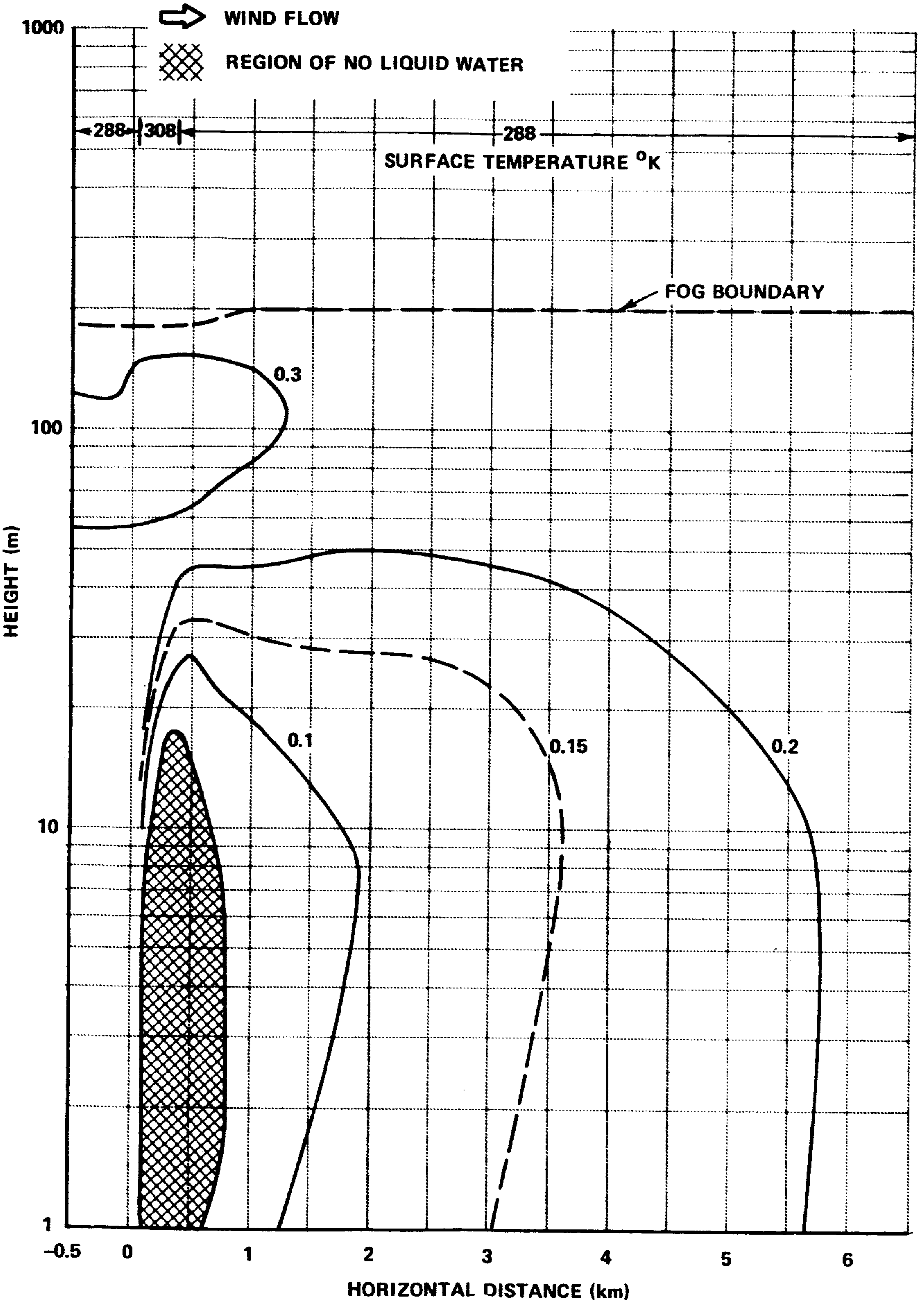

Figure 40 NUMERICAL SIMULATION OF FORCED DISSIPATION OF AN ADVECTION FOG, ISOPLETHS OF LIQUID WATER CONTENT (G M^{-3})

out. Within the framework of such a study, the model could easily be improved by incorporating a prognostic equation for the horizontal wind taking into account the vertical flux of horizontal momentum. The exchange coefficients would respond in a realistic manner to the predicted wind shears and temperature gradients through the Richardson number, eliminating U^* as a parameter in the model. The feasibility of such a modification has already been demonstrated in preliminary experiments with a one-dimensional radiation fog model. In addition, formation of warm air advection fogs over the ocean and steam fogs, where the surface is at or near saturation, could be studied with saturation at the surface temperature as the model's surface boundary condition on water vapor content.

While the sensitivity analysis approach is presently preferred for studying fog formation and natural dissipation, the eventual acquisition of more complete and up-to-date data on artificial dissipation of advection fogs by heating techniques will subsequently require a more sophisticated model. Building upon the present advection fog model, a major model development would incorporate complete fluid dynamics into a two-dimensional advection fog model, including vertical advection and the effects of buoyancy forces on the vertical wind velocities. The result would be a powerful model capable of treating advection fogs in a sea breeze-land breeze system, as well as providing much more realistic simulations of the artificial dissipation of advection fogs by heating techniques.

REFERENCES

Battan, L. J., 1959: Radar Meteorology. University of Chicago Press, 161 pp.

Fisher, E. L., and P. Caplan, 1963: An Experiment in Numerical Prediction of Fog and Stratus. J. Atmos. Sci., 20, 425-437.

Fletcher, N. H., 1966: Physics of Rainclouds. Cambridge University Press, 389 pp.

Goody, R. M., 1964: Atmospheric Radiation. Oxford University Press, 436 pp.

Jiusto, J. E., 1964: Investigation of Warm Fog Properties and Fog Modification Concepts. NASA CR-72.

Kocmond, W. C., W. D. Garrett, and E. J. Mack, 1972: Modification of Laboratory Fog with Organic Surface Films, J. Geophys. Res., 77, 18.

Kocmond, W. C., E. J. Mack, U. Katz, and R. J. Pilié, 1972: Project Fog Drops, Part II - Laboratory Investigations. CAL No. RM-3005-M-6, Cornell Aeronautical Laboratory, Buffalo, NY.

Lumley, J. L., and H. A. Panofsky, 1964: The Structure of Atmospheric Turbulence. New York, Interscience Publishers, 239 pp.

Mack, E. J., and U. Katz, 1971: An Investigation of the Effects of Fog on the Behavior of Tracer Aerosols. CAL No. CJ-5001-M-2, Cornell Aeronautical Laboratory, Buffalo, NY.

McDonald, J. E., 1963: The Saturation Adjustment in Numerical Modeling of Fog, J. Meteor., 20, 476-489.

Molenkamp, C. R., 1968: Accuracy of Finite-Difference Methods Applied to the Advection Equation. J. Appl. Meteor., 7, 160-167.

Neiburger, M. and M. G. Wurtele, 1949: On the Nature and Size of Particles in Haze, Fog, and Stratus of the Los Angeles Region, Chemical Reviews, 44, 2.

Okita, T., 1962: Observations of the Vertical Structure of a Stratus Cloud and Radiation Fogs in Relation to the Mechanisms of Drizzle Formation, Tellus, 14, 310.

Pilié, R. J., W. J. Eadie, E. J. Mack, C. W. Rogers, and W. C. Kocmond, 1972: Project Fog Drops, Part I - Investigation of Warm Fog Properties, CAL No. RM-3005-M-5, Cornell Aeronautical Laboratory, Buffalo, NY.

Richtmeyer, R. D., 1957: Difference Methods for Initial-Value Problems New York, Interscience Publishers, 238 pp.

Rodhe, B., 1962: The Effect of Turbulence on Fog Formation, Tellus, 14, 49-86.

Sassamori, T., 1970: A Numerical Study of Atmospheric and Soil Boundary Layers. J. Atmos. Sci., 27, 1122-1137.

Stephens, J. J., 1961: Spectrally Averaged Total Attenuation, Scattering, and Absorption Cross-sections for Infrared Radiation, J. Meteor., 18, 822-828.

Sutton, O. G., 1953: Micrometeorology, New York, McGraw Hill, 333 pp.

Taylor, G. I., 1917: The Formation of Fog and Mist, Quart. J. Royal Meteor. Soc., 43, 241.

Twomey, S., 1963: Measurements of Natural Cloud Nuclei, J. Res. Atmos., I, 1, p. 101.

Wieland, W., 1956: Condensation of Water Vapor on Natural Aerosol at Slight Supersaturation, Z. Agnew. Math. U. Phys., 7, pp. 428-460.

Zdunkowski, W. G., and B. C. Nielsen, 1969: A Preliminary Prediction Analysis of Radiation Fog, Pure and Appl. Geophys., 75, 278-299.

APPENDIX A

PROGRAM DOCUMENTATION

I. INTRODUCTION

The program documentation provided in this Appendix is separated into several related parts. Within the introduction the essential features of the program are described together with a discussion of some model capabilities. The remainder of the documentation includes a brief discussion of the control which can be exercised over the program in order to study particular features of advection fog (Part II), a listing and definition of variable- and constant-names used in the program (Part III), a description of input cards (Part IV), a page of sample output (Part V), and finally, a listing of the computer program with appropriate comment cards (Part VI). This presentation is designed to allow others to make the program accomplish their desired aims with a minimum expenditure of learning time.

The program described here provides a tool for studying both the formation and dissipation of advection fogs in the vertical (X-Z) plane. In the discussion which follows, quantities which occur in the computer program are capitalized; those that are input quantities are underlined. The model contains advection by the horizontal wind (U) and vertical turbulent diffusion, which produce changes in the dependent variables, potential temperature (PT), water vapor mixing ratio (R), and liquid water mixing ratio (W). Other physical processes which affect these variables are radiational cooling (COOL), provided by vertical divergence of long wave radiative flux (HR), and gravitational sedimentation of the fog drops.

The model can describe the evolution of the fields of PT, R, and W from a variety of initial conditions, subject to the imposed upper and lower boundary conditions. The latter represents the earth's surface, either land or ocean, at which PT is constrained to be equal to the surface temperature. The surface temperature can take on many desired configurations along the X-axis. In addition, at the lower boundary W is set equal to zero, and R undergoes no vertical flux. Values of PT, R, and W at the upper boundary are maintained equal to their initial values. At the upwind boundary, the dependent variables are maintained equal to their initial values. At the downwind boundary, however, the dependent variables are continually adjusted to equal their computed value in the adjacent upwind grid column.

Within each time step (DT), the PT, W, and R fields are changed by the simulated processes, in accordance with the boundary conditions, by an implicit integration scheme. The temperature (T) field is then diagnosed from the PT field. The occurrence of any condensation or evaporation is thus accounted for by a local saturation adjustment of T, R, and W. The PT field is then recovered from the adjusted T field. From these final fields, the diagnostic variables, turbulent exchange coefficient (KA), total water below a height (Z) in a column (INT), and specific heat of saturated air (CPT) are computed and stored for use in taking the next time step.

Output occurs when the total time elapsed (TIME) at the end of a set of time steps equals the print time (PRT). Printout of the fields of vertical eddy heat flux (HC), T, R, liquid water content, dew point depression, HR, and COOL, in that order, is provided. Integration then continues, with output occurring at PRT equal to integer multiples of output time (OT), until program termination at the ending time (ET).

II. CONTROL OF PROGRAM

Flexibility of the program to investigate various aspects of advection fog formation and dissipation rests with the way the configuration of the program can be changed through specification of input data and control indices. These quantities fall into the following categories:

a) time parameters

b) grid spacing and configuration in the vertical and horizontal

c) input parameters controlling which physical processes operate and their magnitude, and the initial values of the dependent variables

d) boundary conditions on temperature and water vapor at the earth's surface boundary

e) options for printout

A. Time

The basic time variable is the length of the time step DT, which can be changed to insure computational stability, and control running time on the computer. Additional time variables are OT, for multiples of which the program prints out, and ET, which is the total meteorological time the program is to run.

B. Grid Spacing

The vertical grid is composed of (KE) levels (up to a maximum of 60) with the space between adjacent levels expanding based on the height of the first level (ZAL) above the earth's surface and an expansion factor (ZAK).

The horizontal grid is composed of (IE) columns (up to a maximum of 40). IE can be specified as any number greater than two and $\leq$ 40, except that printout is conveniently grouped in units of ten columns per page. The horizontal grid is basically specified by (DELX) which is the uniform spacing between columns in that portion of the grid located between (IL) and (IR), the (I)-values of the left and right boundaries of the region of uniform grid spacing. Outside these limits, the grid spacing expands to the upwind and downwind grid limits with the size of spacing controlled by the expansion factor (XAI) and DELX. In the output, negative X's indicate columns located upwind of the uniformly spaced grid and positive values label the uniform portion and columns in the downwind expanding portion.

C. Initial Values

If ISED = 1 and IRAD = 1, sedimentation and radiational cooling, respectively, are included in the model; if ISED and IRAD $\neq$ 1, then the processes are excluded.

PT, W, R, and U can be initialized to be uniform everywhere having values (PTI), (ZERO), (RI), and (UI) when the corresponding control indices (IPT, IW, IRR, and IU) = 0. If IPT = -1, then the temperature profile is isothermal with a value of (TP) and the corresponding initial PT is computed from the hydrostatic relationship. If IPT, IRR, and IW all = 1, the corresponding variables are uniform in X, and T, R, and liquid water content are read from a card listing for K = 1, . . . , KE; the prognostic variables PT and W must then be computed. Temperature and liquid water content are used as input parameters for fog dissipation studies since they are the output quantities from fog formation simulations with the model. If IU $\neq$ 0, then U is an adiabatic profile at all columns, using friction velocity (UV) and roughness length (ZO). For this condition, UI is set equal to zero because of its role in labeling the output.

D. Boundary Values

The boundary condition on the surface potential temperature is controlled by the index (IDTEM). If IDTEM = 0, then (DTEM(I)), the surface temperature change being investigated (negative for advection fog formation, positive for dissipation) equals 0.0. If IDTEM = 1, then DTEM(I) is uniformly equal to (DTEMI) between (ITEML) and (ITEMR), the left and right I-boundaries of this warmer or colder region. If IDTEM = -1, then DTEM(I) is read from a card list for all I's except I = 1 and IE. In all these cases, DTEM(I) is introduced gradually to avoid pulsing the integration. The length of time over which DTEM(I) is introduced is equal to (TIM).

If (IRSFC) = 0, then a boundary condition of no vertical flux is imposed on R at the surface. At present, IRSFC takes on no other values than zero, but it is included so that the model can operate with other boundary conditions after further model development.

Conditions at the upstream boundary remain unchanged throughout the integration, while conditions at the downstream boundary are set equal to those at the adjacent column at the end of each time step.

E. Output

Output from the program is controlled by the main program and performed by a print subroutine (PRNT). For variables in storage, a call of PRNT, with the proper arguments, accomplishes the output. For variables not in storage, the values are computed in the main program and stored in a dummy storage location called HC, and output occurs by calling PRNT with HC as an argument. If (IP) = 0, then the output of HR and COOL can be eliminated.

The print subroutine prints ten data columns per page for each output quantity, along with documentary vertical and horizontal distance information. Each column covers the entire vertical extent of the grid. Logic in the program provides for printing only IE columns of data when IE is less than 40 and an integer multiple of 10. In addition, the first page identifies the output variable, output time, and other selected information which identifies the simulation.

F. Units

Internally, the program operates in cgs units, except that when heat is an explicit unit it is expressed in calories. Two input parameters are not in cgs units: UI is specified in m $\sec^{-1}$ and DELX in meters.

G. Computational Requirements

The program has been written in Fortran and run on an IBM 370/165 digital computer under OS MVT Release 20.1. Approximately 138 K bytes of core storage were required for execution of the program. CPU time requirements for execution of the program depend upon the ratio ET/DT, the total number of grid points (IE) x (KE), and the amount of output specified. In addition, more computations per time step are required in fog than in non-fog regions.

The primary limitation on the maximum time step (DT) that should be employed is the computational stability criterion,

$$\frac{U \cdot DT}{DELX} < 1, \tag{1}$$

for the integration of the horizontal advection terms. It is advisable, however, to restrict DT $\leq$ 60 seconds, even when condition (1) can be satisfied by a larger DT, in order to avoid serious truncation errors and/or computational instabilities in the vertical integrations.

An example of the CPU time requirements for execution of the program is a natural fog dissipation experiment in which KE = 55, IE = 20, and DT = 60 seconds. Approximately 59 seconds of CPU time were required to simulate three hours of meteorological time, with output at the end of each hour.

III. LIST OF COMPUTER VARIABLES

The following list of variables is not arranged in alphabetical order, but rather variables of a common type or variables which are concerned with a given program operation are listed together.

A. Grid Specification

1. Vertical Grid

K = index for vertical grid
KE = number of vertical levels
KN = KE - 1
ZA(K) = vertical coordinate at level K
DZA(K) = grid spacing between level K and K - 1
ZAL = height of lowest vertical grid point in the atmosphere
ZAK = expansion factor in the vertical

2. Horizontal Grid

I = index for horizontal grid
IE = number of horizontal columns
IN = IE - 1
X(I) = horizontal coordinate at column I
DX(I) = grid spacing between columns I and I - 1
DELX = uniform X-spacing
IL = leftmost grid point of unexpanded grid
IR = rightmost grid point of unexpanded grid
XAI = expansion factor in the horizontal

B. Variables

1. Prognostic

PT(I, K) = potential temperature
R(I, K) = water vapor mixing ratio
W(I, K) = liquid water mixing ratio

2. Diagnostic

T(I, K) = temperature
KA(I, K) = turbulent exchange coefficient
INT(I, K) = total liquid water below level K
CPT(I, K) = specific heat of moist air

3. Non-time Dependent

P(K) = pressure
U(I, K) = horizontal wind speed

4. Working Variables

PR(K)
Z(K)
DZ(K)

C. Variable Initialization

RI = initial water vapor mixing ratio
PTI = initial potential temperature
TP = input temperature for pressure computation and isothermal initial condition
UI = uniform wind speed input
DTEM(I) = surface temperature difference, final minus initial
TIM = time interval over which DTEM(I) is introduced
DTEMI = input value of DTEM(I)
ITEML, ITEMR = left and right I-limits on non-zero, uniform DTEM(I)

IDTEM	= 0	DTEM(I) = 0.0
	= 1	DTEM(I) = DTEMI between ITEML and ITEMR, and equals zero elsewhere
	= -1	DTEM(I) = LIST
IPT	= -1	PT(I, K) = TP$\left(\frac{1000}{P}\right)^K$, isothermal
	= 0	PT(I, K) PTI, adiabatic
	= 1	T(I, K) = LIST

IRR	= 0	R(I, K) = RI
	= 1	R(I, K) = LIST
IW	= 0	W(I, K) = 0
	= 1	W(I, K) = LIST
IU	= 0	U(I, K) = UI
	= 1	$U(I, K) = 2.5\ UV\ \ln\left(\frac{Z + Z_o}{Z_o}\right)$

D. Integration

1. Implicit Integration Scheme

Implicit integration factors for PT, R, W, and U*, e.g., EPT and FPT.

2. Physical Process Control

ISED = 1 sedimentation

≠ 1 no sedimentation

IRAD = 1 radiational cooling

≠ 1 no radiational cooling

3. Surface Boundary Conditions

(i) Potential temperature

IF (TIME LE TIM) PT (I, 1) = PT (1, 1) + DTEM(I) TIME/TIM

IF (TIME GT TIM) PT (I, 1) = PT (1, 1) + DTEM(I)

(ii) Water vapor mixing ratio

IF IRSFC = 0 R(I, 1) = R(I, 2)

(iii) Liquid water mixing ratio

W(I, 1) = 0.0

(iv) Horizontal velocity

U(I, 1) = 0.0

---

*Although the present model has no capability for predicting the U-field, provision has been made for this further development by presently including EU and FU in the variables.

4. Time

DT = time step

TIME = time into integration

PRT = time of output

OT = output time interval

ET = ending time of integration

E. Output

HC = vertical, eddy heat flux, cal cm^{-2} min^{-1} (negative downward)

Liquid water content, g m^{-3}

Dew point depression, ^{o}C

EX = turbulent exchange coefficient, cm^{2} sec^{-1}

HR = net radiative flux, cal cm^{-2} min^{-1} (positive upward)

COOL = rate of radiative cooling, ^{o}C hr^{-1}

IP = 0 No HR and COOL output provided.

IP $\neq$ 0 HR and COOL output provided.

FMTH = format for height and variable information on a page for HC, R, dew point depression, liquid water content, EX, HR, COOL

FMTT = format for height and temperature information on a page

F. Constants

1. Physical

L = latent heat of condensation for water vapor

DEN = density of air

CP = specific heat of dry air at constant pressure

G = gravitational constant

RA = gas constant for dry air

RW = gas constant for water vapor

SIGMA = Stefan-Boltzman constant

2. Variable

KW = mean mass absorption coefficient of fog for infrared radiation ($cm^2\ g^{-1}$)

RF = fraction of surface black body radiation used as net upward infrared flux through upper boundary

UF = friction velocity used for computing KA

ZO = roughness length

UV = friction velocity used for computing U (I, K)

CV = sedimentation constant

P(1) = surface pressure

3. Working Constants

CR

CC

CI

CH

CK

CS

CL

IV. SAMPLE SET OF INPUT CARDS

A. TIME VARIABLE CONSTANTS, TEMPERATURE AND WIND INPUT (2 cards)

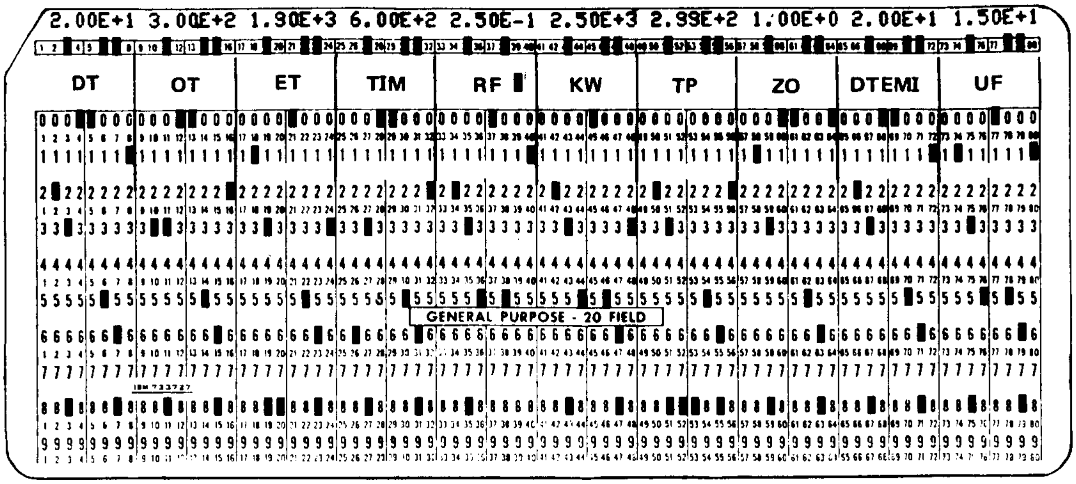

2.00E+1 3.00E+2 1.90E+3 6.00E+2 2.50E-1 2.50E+3 2.99E+2 1.00E+0 2.00E+1 1.50E+1

DT	OT	ET	TIM	RF	KW	TP	ZO	DTEMI	UF

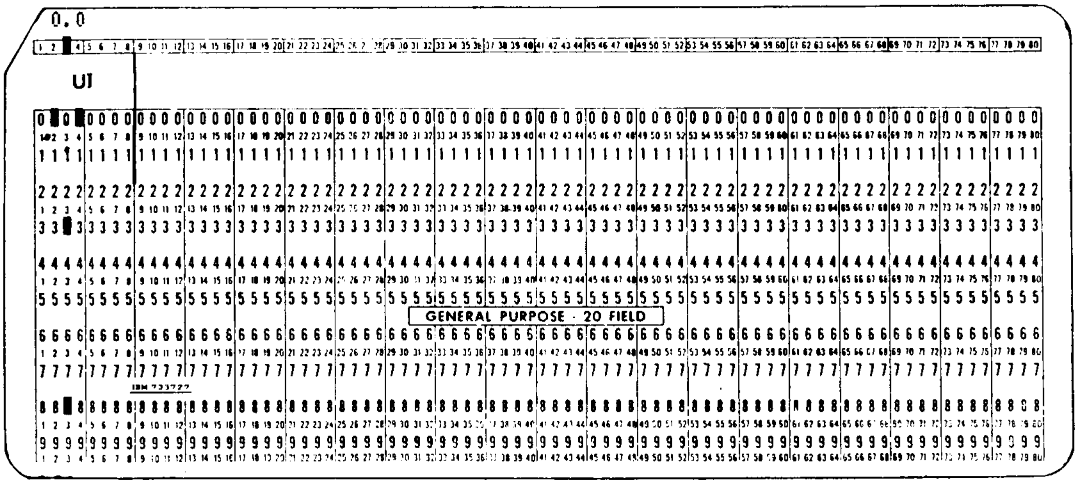

0.0

UI

B. CONTROL INDEX CARD (1 card)

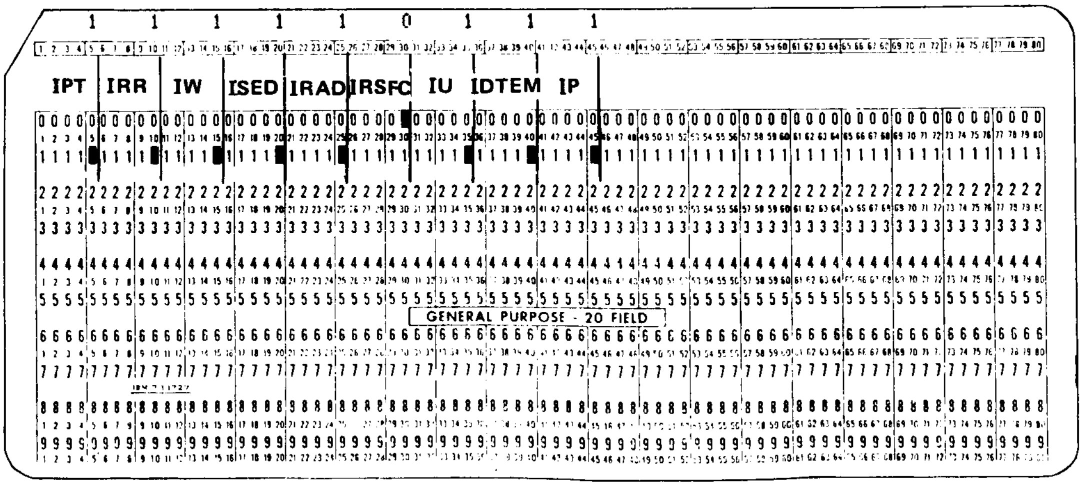

IPT	IRR	IW	ISED	IRAD	IRSFC	IU	IDTEM	IP
1	1	1	1	1	0	1	1	1

C. GRID SPECIFICATION CARD (1 card)

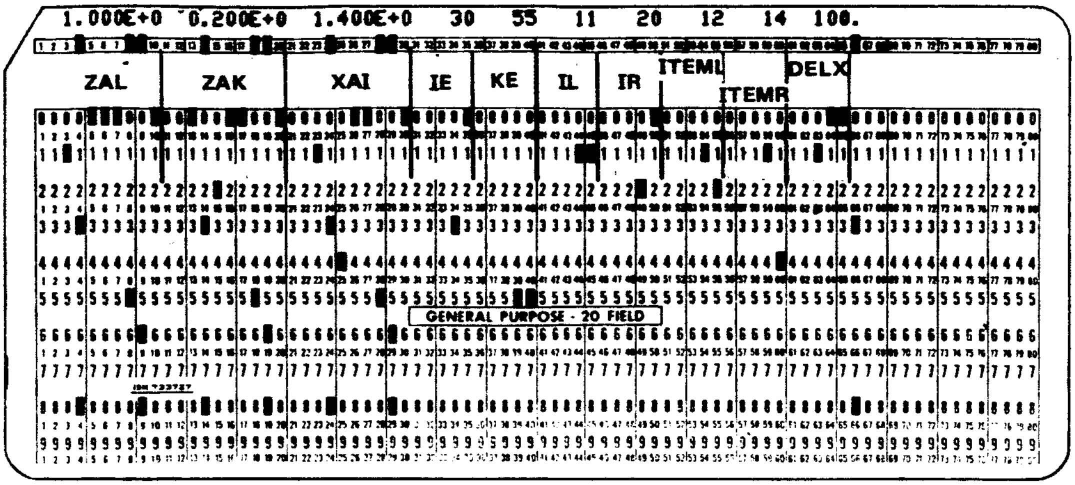

```
 1.000E+0 -0.200E+0  1.400E+0    30   55   11   20   12   14  100.
```

D. OUTPUT FORMATS (2 cards)

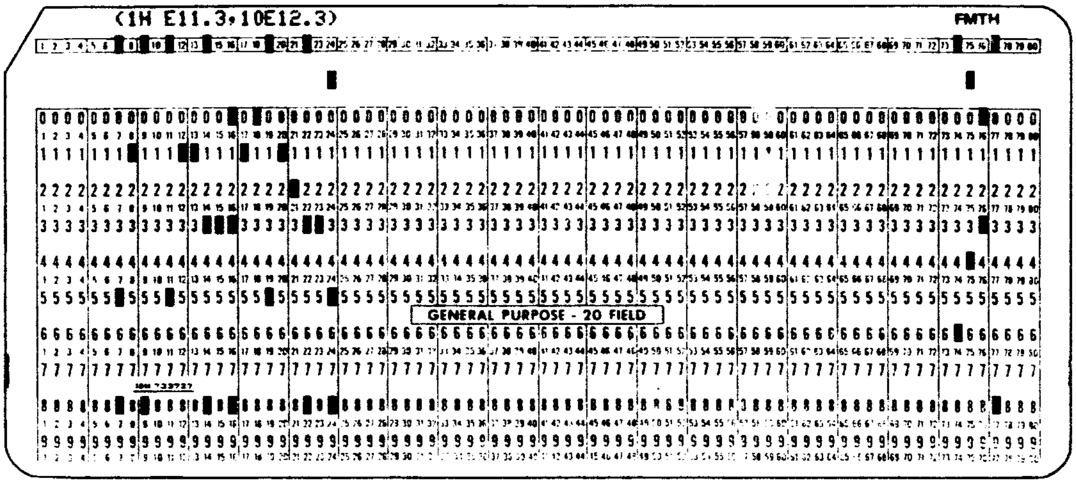

```
        (1H E11.3,10E12.3)                                              FMTH
```

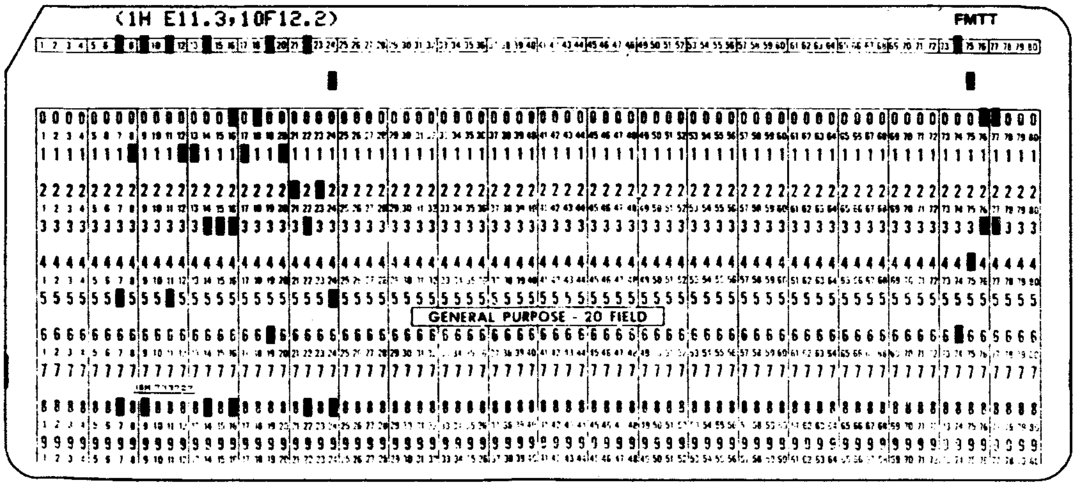

```
        (1H E11.3,10F12.2)                                              FMTT
```

E. PROGNOSTIC VARIABLE INPUT, UNIFORM WITH HEIGHT (1 card)

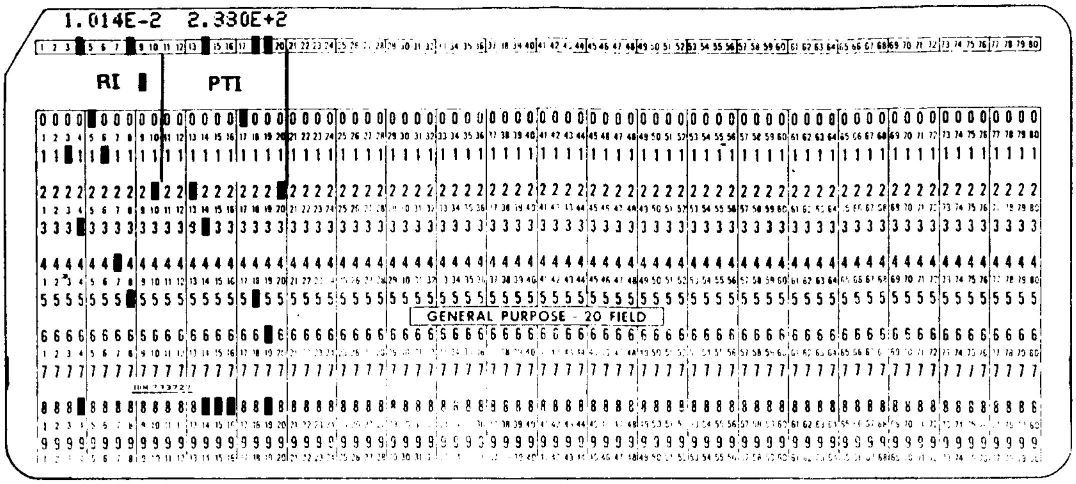

F. VARIABLE INPUT, NON-UNIFORM WITH HEIGHT

1. TEMPERATURE (8 VERTICAL GRID POINTS PER CARD)

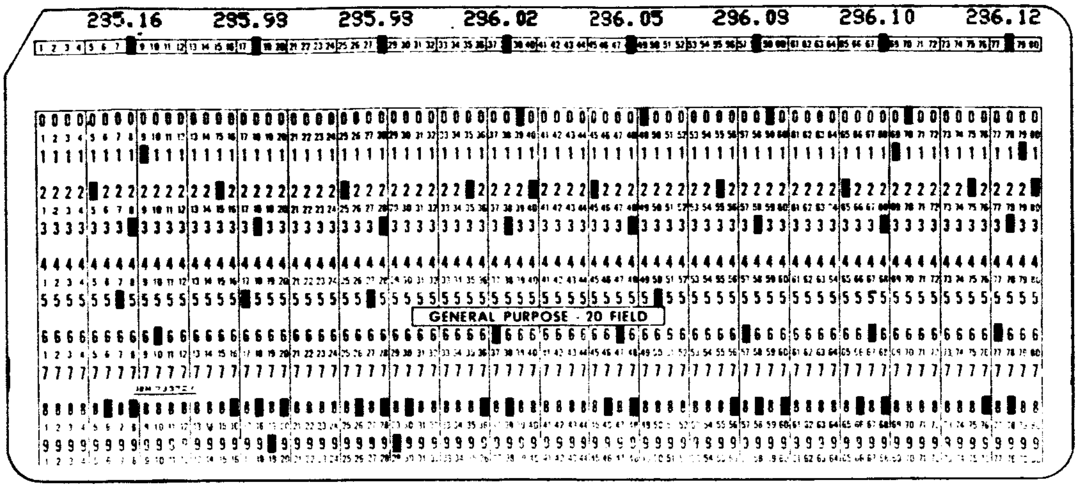

235.16 295.98 295.98 296.02 296.05 296.09 296.10 296.12

2. WATER VAPOR MIXING RATIO (8 VERTICAL GRID POINTS PER CARD)

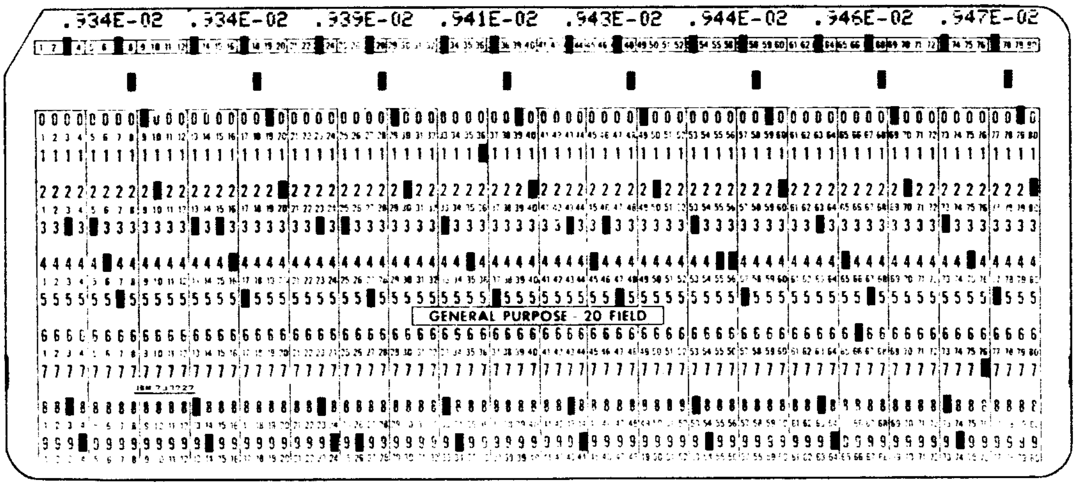

.934E-02 .934E-02 .939E-02 .941E-02 .943E-02 .944E-02 .946E-02 .947E-02

3. LIQUID WATER CONTENT (8 VERTICAL GRID POINTS PER CARD)

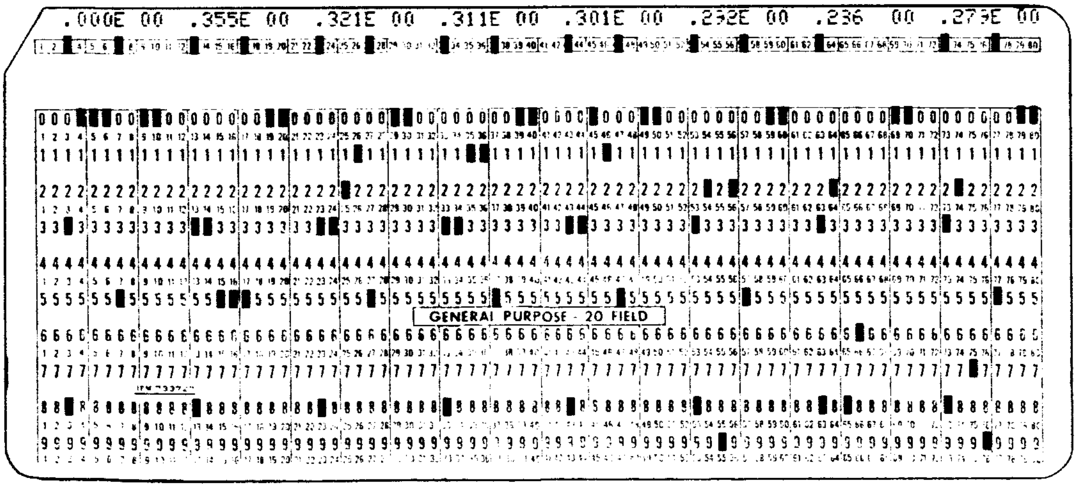

.000E 00 .355E 00 .321E 00 .311E 00 .301E 00 .292E 00 .236 00 .279E 00

V. SAMPLE OF MODEL OUTPUT, FIRST PAGE OF THREE-PAGE OUTPUT

```
LIQUID WATER CONTENT IN G/M**3


TIME=  1800. SEC      DTEMI= 20.0 K       UI= 0.0 M/SEC      UF= 15. CM/SEC  ITEML=12  ITEMR=14

X(KM)=            -9.77        -6.88        -4.82        -3.34        -2.29        -1.53        -0.99        -0.61        -0.34        -0.14
  Z(CM)
 0.943E 05   0.0          0.0          0.0          0.0          0.0          0.0          0.0          0.0          0.0          0.0
 0.786E 05   0.0          0.0          0.0          0.0          0.0          0.0          0.0          0.0          0.0          0.0
 0.655E 05   0.0          0.0          0.0          0.0          0.0          0.0          0.0          0.0          0.0          0.0
 0.546E 05   0.0          0.0          0.0          0.0          0.0          0.0          0.0          0.0          0.0          0.0
 0.455E 05   0.0          0.0          0.0          0.0          0.0          0.0          0.0          0.0          0.0          0.0
 0.379E 05   0.0          0.0          0.0          0.0          0.0          0.0          0.0          0.0          0.0          0.0
 0.316E 05   0.0          0.0          0.0          0.0          0.0          0.0          0.0          0.0          0.0          0.0
 0.263E 05   0.0          0.0          0.0          0.0          0.0          0.0          0.0          0.0          0.0          0.0
 0.219E 05   0.0          0.0          0.0          0.0          0.0          0.0          0.0          0.0          0.0          0.0
 0.183E 05   0.0          0.0          0.0          0.0          0.0          0.0          0.0          0.0          0.0          0.0
 0.152E 05   0.187E-02    0.264E 00    0.365E 00    0.351E 00    0.323E 00    0.292E 00    0.291E 00    0.290E 00    0.284E 00    0.290E 00
 0.127E 05   0.299E 00    0.324E 00    0.354E 00    0.343E 00    0.322E 00    0.293E 00    0.291E 00    0.288E 00    0.280E 00    0.283E 00
 0.106E 05   0.278E 00    0.312E 00    0.335E 00    0.344E 00    0.347E 00    0.345E 00    0.344E 00    0.343E 00    0.342E 00    0.342E 00
 0.881E 04   0.252E 00    0.290E 00    0.314E 00    0.328E 00    0.335E 00    0.339E 00    0.340E 00    0.341E 00    0.341E 00    0.341E 00
 0.734E 04   0.231E 00    0.270E 00    0.294E 00    0.309E 00    0.317E 00    0.322E 00    0.324E 00    0.325E 00    0.326E 00    0.327E 00
 0.612E 04   0.213E 00    0.252E 00    0.276E 00    0.291E 00    0.299E 00    0.303E 00    0.306E 00    0.308E 00    0.309E 00    0.309E 00
 0.510E 04   0.199E 00    0.237E 00    0.260E 00    0.274E 00    0.282E 00    0.285E 00    0.289E 00    0.290E 00    0.291E 00    0.292E 00
 0.425E 04   0.188E 00    0.224E 00    0.247E 00    0.260E 00    0.267E 00    0.271E 00    0.273E 00    0.274E 00    0.275E 00    0.276E 00
 0.354E 04   0.180E 00    0.214E 00    0.235E 00    0.247E 00    0.254E 00    0.257E 00    0.260E 00    0.261E 00    0.262E 00    0.262E 00
 0.295E 04   0.174E 00    0.205E 00    0.225E 00    0.237E 00    0.243E 00    0.246E 00    0.248E 00    0.250E 00    0.250E 00    0.251E 00
 0.246E 04   0.170E 00    0.199E 00    0.218E 00    0.229E 00    0.235E 00    0.238E 00    0.240E 00    0.241E 00    0.241E 00    0.242E 00
 0.205E 04   0.168E 00    0.195E 00    0.212E 00    0.222E 00    0.228E 00    0.231E 00    0.233E 00    0.234E 00    0.235E 00    0.235E 00
 0.170E 04   0.167E 00    0.192E 00    0.209E 00    0.218E 00    0.223E 00    0.226E 00    0.228E 00    0.229E 00    0.229E 00    0.230E 00
 0.142E 04   0.167E 00    0.190E 00    0.206E 00    0.215E 00    0.220E 00    0.222E 00    0.224E 00    0.225E 00    0.225E 00    0.225E 00
 0.118E 04   0.168E 00    0.190E 00    0.204E 00    0.212E 00    0.217E 00    0.220E 00    0.221E 00    0.222E 00    0.222E 00    0.222E 00
 0.984E 03   0.169E 00    0.189E 00    0.203E 00    0.211E 00    0.215E 00    0.218E 00    0.219E 00    0.220E 00    0.220E 00    0.220E 00
 0.819E 03   0.172E 00    0.189E 00    0.202E 00    0.210E 00    0.214E 00    0.216E 00    0.217E 00    0.218E 00    0.218E 00    0.218E 00
 0.682E 03   0.175E 00    0.189E 00    0.201E 00    0.209E 00    0.213E 00    0.215E 00    0.216E 00    0.217E 00    0.217E 00    0.217E 00
 0.567E 03   0.178E 00    0.190E 00    0.201E 00    0.208E 00    0.212E 00    0.214E 00    0.215E 00    0.216E 00    0.216E 00    0.216E 00
 0.472E 03   0.182E 00    0.190E 00    0.201E 00    0.208E 00    0.212E 00    0.213E 00    0.214E 00    0.215E 00    0.215E 00    0.215E 00
 0.392E 03   0.186E 00    0.190E 00    0.200E 00    0.207E 00    0.211E 00    0.213E 00    0.214E 00    0.214E 00    0.215E 00    0.215E 00
 0.326E 03   0.190E 00    0.191E 00    0.200E 00    0.207E 00    0.211E 00    0.212E 00    0.213E 00    0.214E 00    0.214E 00    0.214E 00
 0.271E 03   0.195E 00    0.192E 00    0.201E 00    0.207E 00    0.211E 00    0.212E 00    0.213E 00    0.214E 00    0.214E 00    0.214E 00
 0.225E 03   0.199E 00    0.193E 00    0.201E 00    0.208E 00    0.211E 00    0.212E 00    0.213E 00    0.214E 00    0.214E 00    0.214E 00
 0.187E 03   0.204E 00    0.194E 00    0.202E 00    0.208E 00    0.211E 00    0.213E 00    0.213E 00    0.214E 00    0.214E 00    0.214E 00
 0.155E 03   0.209E 00    0.196E 00    0.203E 00    0.209E 00    0.212E 00    0.213E 00    0.214E 00    0.215E 00    0.215E 00    0.215E 00
 0.128E 03   0.214E 00    0.197E 00    0.204E 00    0.210E 00    0.213E 00    0.214E 00    0.215E 00    0.215E 00    0.215E 00    0.216E 00
 0.106E 03   0.219E 00    0.199E 00    0.205E 00    0.211E 00    0.214E 00    0.215E 00    0.215E 00    0.216E 00    0.216E 00    0.216E 00
 0.874E 02   0.224E 00    0.200E 00    0.206E 00    0.212E 00    0.215E 00    0.216E 00    0.216E 00    0.217E 00    0.217E 00    0.217E 00
 0.720E 02   0.229E 00    0.202E 00    0.208E 00    0.213E 00    0.216E 00    0.217E 00    0.217E 00    0.218E 00    0.218E 00    0.218E 00
 0.592E 02   0.235E 00    0.204E 00    0.209E 00    0.214E 00    0.217E 00    0.218E 00    0.218E 00    0.219E 00    0.219E 00    0.219E 00
 0.485E 02   0.242E 00    0.206E 00    0.211E 00    0.215E 00    0.218E 00    0.219E 00    0.219E 00    0.220E 00    0.220E 00    0.220E 00
 0.396E 02   0.247E 00    0.209E 00    0.212E 00    0.217E 00    0.219E 00    0.220E 00    0.220E 00    0.221E 00    0.221E 00    0.221E 00
 0.322E 02   0.254E 00    0.211E 00    0.214E 00    0.218E 00    0.220E 00    0.221E 00    0.222E 00    0.222E 00    0.222E 00    0.222E 00
 0.260E 02   0.259E 00    0.214E 00    0.216E 00    0.220E 00    0.222E 00    0.223E 00    0.223E 00    0.224E 00    0.224E 00    0.224E 00
 0.208E 02   0.265E 00    0.217E 00    0.218E 00    0.222E 00    0.223E 00    0.224E 00    0.224E 00    0.225E 00    0.225E 00    0.225E 00
 0.165E 02   0.272E 00    0.220E 00    0.221E 00    0.224E 00    0.225E 00    0.226E 00    0.226E 00    0.227E 00    0.227E 00    0.227E 00
 0.129E 02   0.279E 00    0.224E 00    0.224E 00    0.227E 00    0.227E 00    0.228E 00    0.228E 00    0.229E 00    0.229E 00    0.229E 00
 0.993E 01   0.286E 00    0.228E 00    0.227E 00    0.229E 00    0.230E 00    0.231E 00    0.230E 00    0.231E 00    0.231E 00    0.231E 00
 0.744E 01   0.292E 00    0.233E 00    0.231E 00    0.232E 00    0.233E 00    0.233E 00    0.233E 00    0.233E 00    0.234E 00    0.234E 00
 0.537E 01   0.301E 00    0.239E 00    0.235E 00    0.236E 00    0.236E 00    0.237E 00    0.237E 00    0.237E 00    0.237E 00    0.237E 00
 0.364E 01   0.311E 00    0.246E 00    0.241E 00    0.241E 00    0.241E 00    0.241E 00    0.241E 00    0.241E 00    0.241E 00    0.241E 00
 0.220E 01   0.321E 00    0.257E 00    0.249E 00    0.247E 00    0.247E 00    0.246E 00    0.246E 00    0.246E 00    0.246E 00    0.246E 00
 0.100E 01   0.355E 00    0.275E 00    0.264E 00    0.260E 00    0.258E 00    0.258E 00    0.258E 00    0.258E 00    0.258E 00    0.258E 00
 0.0         0.0          0.0          0.0          0.0          0.0          0.0          0.0          0.0          0.0          0.0
```

VI. FORTRAN LISTING OF COMPUTER PROGRAM WITH COMMENT CARDS

```
C
C
C     TWO-DIMENSIONAL ADVECTION FOG MODEL
C     STEADY STATE MODEL
C
C     CORNELL AERO. LAB. INC.  MAY 1972 W.J.EADIE AND C.W.ROGERS
C
C
      REAL*4 KA,INT,KW,L
      COMMON PT(40,60),R(40,60),W(40,60),U(40,60),T(40,60),KA(40,60),
     1       INT(40,60),CPT(40,60),HC(40,60),X(40),DX(40),DTEM(40),
     2       P(60),ZA(60),DZA(60),EPT(60),FPT(60),ER(60),FR(60),EW(60),
     3       FW(60),EU(60),FU(60),Z(60),DZ(60),PR(60),L,DEN,CP,G,RA,RW,
     4       SIGMA,TIME,DT,TIM,UF,RF,KW,ZO,CV,UI,DTEMI,ZAK,XAI,DELX,CC,
     5       CH,CI,CK,CL,CR,CS,UU,
     6       KE,KN,IE,IN,IL,IR,ISED,IRAD,IRSFC,IDTEM,ITEML,ITEMR,IP
      DIMENSION FMTH(11),FMTT(11)
C
C     PHYSICAL CONSTANTS
C
      L=592.
      DEN=1.23E-3
      CP=.240
      G=980.6
      RA=.0686
      RW=.1102
      SIGMA=1.355E-12
      CV=400.
      UV=15.
      P(1)=1000.
C
C     DATA INPUT
C
   10 READ(5,1000,END=400) DT,OT,ET,TIM,RF,KW,TP,ZO,DTEMI,UF,UI
      READ(5,1100) IPT,IRR,IW,ISED,IRAD,IRSFC,IU,IDTEM,IP
      READ(5,1200) ZAL,ZAK,XAI,IE,KE,IL,IR,ITEML,ITEMR,DELX
      READ(5,1205) FMTH,FMTT
C
C     DATA LISTING
C
      WRITE(6,2000) DT,OT,ET,TIM,RF,KW,TP,ZO,DTEMI,UF,UI
      WRITE(6,2100) IPT,IRR,IW,ISED,IRAD,IRSFC,IU,IDTEM,IP
      WRITE(6,2200) ZAL,ZAK,XAI,IE,KE,IL,IR,ITEML,ITEMR,DELX
C
C     WORKING CONSTANT DEFINITION
C
      CR=KW*RF*SIGMA/CP
      CC=.622*(L**2)/(CP*RA)
      CI=KW*DEN/2.
      CH=(L**2)/RW
      CK=.4*UF
      CS=G/4.186E+7
      UU=2.*UF**2
      IN=IE-1
      KN=KE-1
C
C     VERTICAL GRID SPECIFICATION
C
      ZA(1)=0.0
      ZA(2)=ZAL
      DZA(2)=ZAL
```

```
      DO 20 K=3,KE
      DZA(K)=(1.+ZAK)*DZA(K-1)
   20 ZA(K)=ZA(K-1)+DZA(K)
C
C     HORIZONTAL GRID SPECIFICATION
C
      DO 30 I=IL,IR
   30 X(I)=(I-IL)*DELX
      I1=IR+1
      DO 31 I=I1,IE
   31 X(I)=X(I-1)+XAI*(X(I-1)-X(I-2))
      IF(IL .EQ. 1) GO TO 33
      I1=IL-1
      DO 32 I2=1,I1
      I=I1-I2+1
   32 X(I)=X(I+1)-XAI*(X(I+2)-X(I+1))
   33 DO 35 I=2,IE
   35 DX(I)=X(I)-X(I-1)
C
C
C     VARIABLE INITIALIZATION
C
C
      READ(5,1300) RI,PTI
      WRITE(6,2300) RI,PTI
      TP=TP+.16
      PTI=PTI+.16
      W(1,1)=0.0
C
C     A-UNIFROM WITH HEIGHT
C
      DO 40 I=1,IE
      DO 40 K=1,KE
      IF(IU .EQ. 0) U(I,K)=UI
      IF(IW .EQ. 0) W(I,K)=0.0
      IF(IRR .EQ. 0) R(I,K)=RI
      IF(IPT .EQ. 0) PT(I,K)=PTI
      IF(I .EQ. 1) P(K)=1000.*EXP(-G*ZA(K)/(4.186E+7*RA*TP))
C
C     B-ISOTHERMAL
C
      IF(IPT .EQ. -1) PT(I,K)=TP*((1000./P(K))**.286)
C
   40 CONTINUE
C
C     C-VARIABLE LIST
C
      IF(IPT .EQ. 1) READ(5,1400) ( T(1,K),K=1,KE)
      IF(IRR .EQ. 1) READ(5,1500) (R(1,K),K=1,KE)
      IF(IW .EQ. 1) READ(5,1500) (W(1,K),K=1,KE)
      IF(IPT .EQ. 1) WRITE(6,2400) ( T(1,K),K=1,KE)
      IF(IRR .EQ. 1) WRITE(6,2500) (R(1,K),K=1,KE)
      IF(IW .EQ. 1) WRITE(6,2500) (W(1,K),K=1,KE)
      IF(IU .EQ. 0) GO TO 60
C
C     D-ADIABATIC U-PROFILE
C
      DO 41 K=1,KE
   41 U(1,K)=2.5*UV*ALOG((ZA(K)+ZO)/ZO)
      DO 42 I=2,IE
      DO 42 K=1,KE
```

```
   42 U(I,K)=U(1,K)
C
      IF(IPT .EQ. 1) GO TO 45
      GO TO 60
C
C     PT AND W FROM VARIABLE LIST
C
   45 DO 47 K=1,KE
      PT(1,K)=T(1,K)*((1000./P(K))**.286)
   47 W(1,K)=W(1,K)/(1.0E+6*DEN)
C
C     INITIALIZATION ALL COLUMNS
C
      DO 50 I=2,IE
      DO 50 K=1,KE
      PT(I,K)=PT(1,K)
      R(I,K)=R(1,K)
   50 W(I,K)=W(1,K)
   60 CONTINUE
C
C     INITIALIZATION,EXCHANGE COEFFICIENT, INTEGRATED LIQUID WATER,AND
C     SPECIFIC HEAT OF MOIST AIR
      Z(KE)= ZΦ+ (ZA(KE)+ ZA(KE-1))/2.
      CL=14.*G*.16/PT(1,1)
      INT(1,1)=0.0
      T(1,1)=PT(1,1)
      DO 80 K=2,KE
      Z(K)=ZO+(ZA(K)+ZA(K-1))/2.
      PR(K)=(1000./P(K))**.286
      DZ(K)=(1.+ZAK/2.)*(DZA(K)**2)
      T(1,K)=PT(1,K)/PR(K)
      IF(W(1,K) .GT. 0.0) GO TO 65
      CPT(1,K)=CP
      S=(PT(1,K)-PT(1,K-1))/DZA(K)
      GO TO 70
   65 CPT(1,K)=CP+CH*RSF(T(1,K),P(K))/(T(1,K)**2)
      S=(T(1,K)-T(1,K-1))/DZA(K)+CS/CPT(1,K)
   70 SS=CL*S*Z(K)**2
      IF(SS .GE. 100.*UU) KA(1,K)=UU/(2.*SQRT(14.*G*S/PT(1,1)))
      IF(SS .LT. 100.*UU) KA(1,K)=.4*Z(K)*SQRT((-SS+SQRT(SS**2+UU**2))/2
     1.)
      IF((Z(K)**2)/(4.*KA(1,K)) .LT. 600.) GO TO 79
      KA(1,K)=KA(1,KK)*((Z(KE)-Z(K))/(Z(KE)-Z(KK)))**2
      GO TO 80
   79 KK=K
   80 INT(1,K)=INT(1,K-1)+KW*DEN*(W(1,K)+W(1,K-1))*DZA(K)/2.
      CPT(1,1)=CPT(1,2)
      KA(1,1)=KA(1,2)
C
C     INITIALIZATION ALL COLUMNS
C
      DO 81 I=2,IE
      DO 81 K=1,KE
      IF(K .EQ. 1) W(I,K)=0.0
      T(I,K)=T(1,K)
      CPT(I,K)=CPT(1,K)
      KA(I,K)=KA(1,K)
   81 INT(I,K)=INT(1,K)
C
C     INITIALIZATION OF SURFACE TEMPERATURE DIFFERENCE
C
```

```
      DO 85 I=1,IN
      IF(IDTEM .EQ. 0) DTEM(I)=0.0
      IF(IDTEM .EQ. 1) DTEM(I)=DTEMI
      IF((IDTEM .EQ. 1) .AND. (I .LT. ITEML)) DTEM(I)=0.0
      IF((IDTEM .EQ. 1) .AND. (I .GT. ITEMR)) DTEM(I)=0.0
      IF(IDTEM .EQ. -1) READ(5,1400) (DTEM(I),I=2,IN)
      IF(IDTEM .EQ. -1) WRITE(6,2400) (DTEM(I),I=2,IN)
   85 CONTINUE
C
C     UPPER BOUNDARY CONDITION FOR IMPLICIT INTEGRATION
C
      EPT(KE)=0.0
      FPT(KE)=PT(1,KE)
      ER(KE)=0.0
      FR(KE)=R(1,KE)
      EW(KE)=0.0
      FW(KE)=W(1,KE)
C
C     OUTPUT TIME ,END TIME, AND TIME STEP CONTROL
C
      TIME=0.0
      PRT=OT
   90 IF(TIME .LT. PRT) GO TO 95
      PRT=TIME+OT
      GO TO 200
   95 IF(TIME .GE. ET) GO TO 10
      TIME=TIME+DT
      CALL STEP
      GO TO 90
  200 CONTINUE
C
C
C     OUTPUT
C
C
C
C     EDDY HEAT FLUX OUTPUT
C
  300 WRITE(6,3000)
      DO 311 I=1,IE
      DO 310 K=2,KN
      IF(CPT(I,K) .LE. CP) HC(I,K)=-DEN*CP*((KA(I,K)+KA(I,K+1))/2.)*(PT(
     1I,K+1)-PT(I,K-1))/(ZA(K+1)-ZA(K-1))*60.
  310 IF(CPT(I,K) .GT. CP) HC(I,K)=-DEN*CPT(I,K)*(((KA(I,K)+KA(I,K+1))/2
     1.)*((T(I,K+1)-T(I,K-1))/(ZA(K+1)-ZA(K-1))+CS/CPT(I,K)))*60.
      HC(I,1)=-DEN*CK*(.5+ZO/DZA(2))*(CP*(PT(I,2)-PT(I,1)))*60.
      HC(I,KE)=HC(I,KN)
  311 CONTINUE
      CALL PRNT(HC,FMTH)
C
C     TEMPERATURE OUTPUT
C
      WRITE(6,3100)
      CALL PRNT(T,FMTT)
C
C     MIXING RATIO OUTPUT
C
      WRITE(6,3200)
      CALL PRNT(R,FMTH)
C
C     LIQUID WATER CONTENT OUTPUT
```

```
C
      WRITE(6,3300)
      DO 315 I=1,IE
      DO 315 K=1,KE
  315 HC(I,K)=DEN*W(I,K)*1.0E+6
      CALL PRNT(HC,FMTH)
C
C     DEW POINT DEPRESSION OUTPUT
C
      WRITE(6,3400)
      DO 320 I=1,IE
      DO 320 K=1,KE
C
C     DEW POINT DEPRESSION COMPUTATION
C
      E=P(K)*R(I,K)/(.62465+R(I,K))
      T1=T(I,K)
      DO 318 M=1,3
      RS=RSF(T1,P(K))
      ES=P(K)*RS/(.62465+RS)
      EE=E/ES
  318 T1=T1+(T1-35.86)*ALOG(EE)/17.26939
  320 HC(I,K)=T(I,K)-T1
      CALL PRNT(HC,FMTH)
C
C     TURBULENT EXCHANGE COEFFICIENT OUTPUT
C
      WRITE(6,3500)
      DO 331 I=1,IE
      DO 330 K=2,KN
      EX=(KA(I,K)+KA(I,K+1))/2.
  330 HC(I,K)=EX
      HC(I,1)=HC(I,2)
  331 HC(I,KE)=HC(I,KN)
      CALL PRNT(HC,FMTH)
C
      IF(IP .EQ. 0) GO TO 95
C
C     RADIATIVE FLUX OUTPUT
C
      WRITE(6,3600)
      DO 340 I=1,IE
      DO 340 K=1,KE
      HR=RF*SIGMA*(T(I,1)**4)*EXP(-INT(I,KE)+INT(I,K))*60.
  340 HC(I,K)=HR
      CALL PRNT(HC,FMTH)
C
C     RADIATIVE COOLING RATE OUTPUT
C
      WRITE(6,3700)
      DO 350 I=1,IE
      DO 350 K=1,KE
      COOL=-3600.*W(I,K)*KW*RF*SIGMA*(T(I,1)**4)*EXP(-INT(I,KE)+INT(I,K)
     1)/CPT(I,K)
  350 HC(I,K)=COOL
      CALL PRNT(HC,FMTH)
C
      GO TO 95
  400 STOP
 1000 FORMAT(10E8.2 / -2PF4.1)
 1100 FORMAT(9I5)
```

```
 1200 FORMAT(3E10.3,6I5,-2PF6.0)
 1205 FORMAT(11A4/11A4)
 1300 FORMAT(4E10.3)
 1400 FORMAT(8F10.2)
 1500 FORMAT(8E10.3)
 2000 FORMAT(1H1,////,60X,10HINPUT DATA,//,1H0,10F10.3,-2PF4.1)
 2100 FORMAT(1H0,9I5)
 2200 FORMAT(1H0,3E10.3,6I5,-2PF6.0)
 2300 FORMAT(1H0,4E10.3)
 2400 FORMAT(1H0,8F10.2)
 2500 FORMAT(1H0,8E10.3)
 3000 FORMAT(27H1EDDY FLUX IN CAL/CM**2 MIN///)
 3100 FORMAT(21H1TEMPERATURE IN DEG K///)
 3200 FORMAT(20H1MIXING RATIO IN G/G///)
 3300 FORMAT(31H1LIQUID WATER CONTENT IN G/M**3///)
 3400 FORMAT(30H1DEW POINT DEPRESSION IN DEG C///)
 3500 FORMAT(44H1TURBULENT EXCHANGE COEFFICIENT IN CM**2/SEC///)
 3600 FORMAT(31H1RADIATIVE FLUX IN CAL/CM**2MIN///)
 3700 FORMAT(30H1RADIATIVE COOLING IN DEG C/HR///)
      END
C
C
C      INTEGRATION SUBROUTINE
C
C      INTEGRATE ONE TIME STEP AND COMPUTE NEW PROGNOSTIC & DIAGNOSTIC
C      VARIABLES
C
      SUBROUTINE STEP
      REAL*4 KA,INT,KW,L
      COMMON PT(40,60),R(40,60),W(40,60),U(40,60),T(40,60),KA(40,60),
     1       INT(40,60),CPT(40,60),HC(40,60),X(40),DX(40),DTEM(40),
     2       P(60),ZA(60),DZA(60),EPT(60),FPT(60),ER(60),FR(60),EW(60),
     3       FW(60),EU(60),FU(60),Z(60),DZ(60),PR(60),L,DEN,CP,G,RA,RW,
     4       SIGMA,TIME,DT,TIM,UF,RF,KW,ZO,CV,UI,DTEMI,ZAK,XAI,DELX,[illegible],
     5       CH,CI,CK,CL,CR,CS,UU,
     6       KE,KN,IE,IN,IL,IR,ISED,IRAD,IRSFC,IDTEM,ITEMI,ITEMR,IP
C
C      UPWIND DO LOOP OVER HORIZONTAL GRID SYSTEM
C
      DO 80 M=2,IN
      I=IN+2-M
C
C      DOWNWARD DO LOOP OVER VERTICAL GRID SYSTEM TO SET UP IMPLICIT
C      INTEGRATION
C
      DO 20 N=2,KN
      K=KN+2-N
      DD=DT/DZ(K)
      A=DD*KA(I,K+1)/(1.+ZAK)
      AW=A
      C=DD*KA(I,K)
      CW=C
      IF(ISED .NE.1) GO TO 10
C
C      DROP SEDIMENTATION
C
      DS=CV*DD*DZA(K)/2.
      AW=AW+DS*(W(I,K+1)**.667)
      CW=CW-DS*(W(I,K-1)**.667)
C
   10 B=1.+A+C
```

```
      BB=2.-B
      DPT=PT(I,K)-U(I,K)*(PT(I,K)-PT(I-1,K))*DT/DX(I)
C
C     RADIATIONAL COOLING
C
      IF((IRAD .EQ. 1) .AND. (W(I,K) .GT. 0.0)) DPT=DPT-CR*W(I,K)*(PT(I,
     11)**4)*EXP(-INT(I,KE)+INT(I,K))*PR(K)*DT
C
      DW = W(I,K)-U(I,K)*( W(I,K)- W(I-1,K))*DT/DX(I)
      DR = R(I,K)-U(I,K)*( R(I,K)- R(I-1,K))*DT/DX(I)
      EPT(K)=C/(B-A*EPT(K+1))
      ER(K)=C/(B-A*ER(K+1))
      EW(K)=CW/(B-AW*EW(K+1))
      FPT(K)=(DPT+A*FPT(K+1))*EPT(K)/C
      FR(K)=(DR+A*FR(K+1))*ER(K)/C
      FW(K)=(DW+AW*FW(K+1))*EW(K)/CW
   20 CONTINUE
C
C     UPDATE SURFACE BOUNDARY CONDITION
C
      IF(TIME .LE. TIM) PT(I,1)=PT(1,1)+DTEM(I)*TIME/TIM
      IF(TIME .LE. TIM) T(I,1)=PT(I,1)
      IF(IRSFC .EQ. 0) R(I,1)=FR(2)/(1.-ER(2))
C
C     UPWARD DO LOOP OVER VERTICAL GRID SYSTEM TO COMPUTE NEW PROGNOSTIC
C     AND DIAGNOSTIC VARIABLES
C
      INT(I,1)=0.0
      DO 70 K=2,KE
      IF(K .EQ. KE) GO TO 40
      PT(I,K)=EPT(K)*PT(I,K-1)+FPT(K)
      R(I,K)=ER(K)*R(I,K-1)+FR(K)
      W(I,K)=EW(K)*W(I,K-1)+FW(K)
C
C     COMPUTE TEMPERATURE
C
      T(I,K)=PT(I,K)/PR(K)
C
C     SATURATION ADJUSTMENT
C
      RS=RSF(T(I,K),P(K))
      IF((R(I,K) .LE. RS) .AND. (W(I,K) .LE. 0.0)) GO TO 40
      DR=(R(I,K)-RS)/(1.+CC*RS/(T(I,K)**2))
      IF(R(I,K) .GT. RS) GO TO 30
      IF(-DR .LE. W(I,K)) GO TO 30
      DR=-W(I,K)
   30 T(I,K)=T(I,K)+DR*L/CP
      PT(I,K)=T(I,K)*PR(K)
      R(I,K)=R(I,K)-DR
      W(I,K)=W(I,K)+DR
C
C     COMPUTE NEW VALUES OF INT, CPT, AND KA
C
   40 IF(W(I,K) .LT. 0.0) W(I,K)=0.0
      INT(I,K)=INT(I,K-1)+CI*(W(I,K)+W(I,K-1))*DZA(K)
      IF(W(I,K) .GT. 0.0) GO TO 50
      CPT(I,K)=CP
      S=(PT(I,K)-PT(I,K-1))/DZA(K)
      GO TO 60
   50 CPT(I,K)=CP+CH*RSF(T(I,K),P(K))/(T(I,K)**2)
      S=(T(I,K)-T(I,K-1))/DZA(K)+CS/CPT(I,K)
```

```
   60 SS=CL*S*Z(K)**2
      IF(SS .GE. 100.*UU) KA(I,K)=UU/(2.*SQRT(14.*G*S/PT(1,1)))
      IF(SS .LT. 100.*UU) KA(I,K)=.4*Z(K)*SQRT((-SS+SQRT(SS**2+UU**2))/2
     1.)
      IF((Z(K)**2)/(4.*KA(I,K)) .LT. 600.) GO TO 69
      KA(I,K)=KA(I,KK)*((Z(KE)-Z(K))/(Z(KE)-Z(KK)))**2
      GO TO 70
   69 KK=K
C
   70 CONTINUE
C
C     UPDATE SURFACE BOUNDARY CONDITION ON R AFTER SATURATION ADJUSTMENT
C
      IF(IRSFC .EQ. 0) R(I,1)=R(I,2)
C
   80 CONTINUE
C
C     UPDATE DOWNWIND BOUNDARY CONDITION
C
      DO 90 K=1,KE
      PT(IE,K)=PT(IN,K)
      R(IE,K)=R(IN,K)
      W(IE,K)=W(IN,K)
      KA(IE,K)=KA(IN,K)
      T(IE,K)=T(IN,K)
      CPT(IE,K)=CPT(IN,K)
      INT(IE,K)=INT(IN,K)
   90 CONTINUE
      RETURN
      END
C
C
C     PRINT SUBROUTINE
C
      SUBROUTINE PRNT(O,FORM)
      REAL*4 KA,INT,KW,L
      COMMON PT(40,60),R(40,60),W(40,60),U(40,60),T(40,60),KA(40,60),
     1        INT(40,60),CPT(40,60),HC(40,60),X(40),DX(40),DTEM(40),
     2        P(60),ZA(60),DZA(60),EPT(60),FPT(60),ER(60),FR(60),EW(60),
     3        FW(60),EU(60),FU(60),Z(60),DZ(60),PR(60),L,DEN,CP,G,RA,RW,
     4        SIGMA,TIME,DT,TIM,UF,RF,KW,ZO,CV,UI,DTEMI,ZAK,XAI,DELX,CC,
     5        CH,CI,CK,CL,CR,CS,UU,
     6        KE,KN,IE,IN,IL,IR,ISED,IRAD,IRSFC,IDTEM,ITEML,ITEMR,IP
      DIMENSION O(40,60),FORM(11)
C
C     OUTPUT DOCUMENTATION
C
      WRITE(6,4000) TIME,DTEMI,UI,UF,ITEML,ITEMR
C
C     PAGE 1 COLUMNS 1-10
C
      WRITE(6,4100) (X(I),I=1,10)
      DO 450 J=1,KE
      K=KE-J+1
  450 WRITE(6,FORM) ZA(K),(O(I,K),I=1,10)
C
      IF(IE .LT. 11) GO TO 490
C
C     PAGE 2 COLUMNS 11-20
C
      WRITE(6,4105) (X(I),I=11,20)
```

```
      DO 460 J=1,KE
      K=KE-J+1
  460 WRITE(6,FORM) ZA(K),(O(I,K),I=11,20)
C
      IF(IE .LT. 21) GO TO 490
C
C     PAGE 3 COLUMNS 21-30
C
      WRITE(6,4105) (X(I),I=21,30)
      DO 470 J=1,KE
      K=KE-J+1
  470 WRITE(6,FORM) ZA(K),(O(I,K),I=21,30)
C
      IF(IE .LT. 31) GO TO 490
C
C     PAGE 4 COLUMNS 31-IE
C
      WRITE(6,4105) (X(I),I=31,IE)
      DO 480 J=1,KE
      K=KE-J+1
  480 WRITE(6,FORM) ZA(K),(O(I,K),I=31,IE)
C
  490 CONTINUE
 4000 FORMAT(6HOTIME=,F7.0,4H SEC,6X,6HOTEMI=,F5.1,2H K,6X,3HUI=,-2PF4.1
     1,6H M/SEC,6X,3HUF=,0PF4.0,7H CM/SEC,2X,6HITEML=,I2,2X,6HITEMR=,I2)
 4100 FORMAT(1H0,6HX(KM)=,6X,10(-5PF12.2) / 1H ,3X,5HZ(CM))
 4105 FORMAT(1H1,6HX(KM)=,6X,10(-5PF12.2) / 1H ,3X,5HZ(CM))
      RETURN
      END
C
C
C     SATURATION MIXING RATIO AS A FUNCTION OF TEMPERATURE A AND
C     PRESSURE B
C
      FUNCTION RSF(A,B)
      ES=6.1078*EXP(17.26939*(A-273.16)/(A-35.86))
      RSF=.62465*ES/(B-ES)
      RETURN
      END
```

DATA CARDS

```
2.00E+1 3.00E+2 1.80E+3 6.00E+2 2.50E-1 2.50E+3 2.88E+2 1.00E+0 2.00E+1 1.50E+1
0.0
   1     1     1     1     1     0     1     1     1
 1.000E+0  0.200E+0  1.400E+0    30    55    11    20    12    14  100.
      (1H E11.3,10E12.3)                                                  FMTH
      (1H E11.3,10F12.2)                                                  FMTT
 1.014E-2  2.880E+2
```

TEMPERATURE

```
   285.16     285.98     285.98     286.02     286.05     286.08     286.10     286.12
   286.14     286.17     286.18     286.20     286.22     286.24     286.26     286.28
   286.30     286.32     286.33     286.35     286.37     286.38     286.40     286.41
   286.43     286.44     286.46     286.47     286.48     286.49     286.50     286.51
   286.52     286.52     286.53     286.52     286.52     286.51     286.50     286.49
   286.45     286.42     286.38     286.35     286.76     287.43     287.68     287.81
   287.90     288.00     288.08     288.08     288.08     288.08     288.16
```

```
                                  WATER VAPOR MIXING RATIO

.934E-02   .934E-02   .939E-02   .941E-02   .943E-02   .944E-02   .946E-02   .947E-02
.949E-02   .950E-02   .951E-02   .953E-02   .954E-02   .955E-02   .956E-02   .957E-02
.959E-02   .960E-02   .961E-02   .962E-02   .963E-02   .964E-02   .965E-02   .966E-02
.967E-02   .968E-02   .969E-02   .970E-02   .971E-02   .972E-02   .973E-02   .974E-02
.975E-02   .975E-02   .976E-02   .976E-02   .977E-02   .977E-02   .977E-02   .977E-02
.977E-02   .976E-02   .976E-02   .976E-02   .101E-01   .101E-01   .101E-01   .101E-01
.101E-01   .101E-01   .101E-01   .101E-01   .101E-01   .101E-01   .101E-01

                                  LIQUID WATER CONTENT

.000E 00   .355E 00   .321E 00   .311E 00   .301E 00   .292E 00   .286  00   .279E 00
.272E 00   .265E 00   .259E 00   .254E 00   .247E 00   .242E 00   .235E 00   .229E 00
.224E 00   .219E 00   .214E 00   .209E 00   .204E 00   .199E 00   .195E 00   .190E 00
.186E 00   .182E 00   .178E 00   .175E 00   .172E 00   .169E 00   .168E 00   .167E 00
.167E 00   .168E 00   .170E 00   .174E 00   .180E 00   .188E 00   .199E 00   .213E 00
.231E 00   .252E 00   .278E 00   .299E 00   .187E-02   .000E 00   .000E 00   .000E 00
.000E 00   .000E 00   .000E 00   .000E 00   .000E 00   .000E 00   .000E 00
```